PONTIFÍCIA UNIVERSIDADE CATÓLICA
DO RIO DE JANEIRO

Rayanne Carla Alves do Nascimento

Numerical Analysis of the Influence of the Use of Hydrogen as a Secondary Fuel in Spark-Assisted Compression Ignition Engines

Dissertação de Mestrado

Dissertation presented to the Programa de Pós-Graduação em Engnharia Mecânica of PUC-Rio in partial fulfillment of requirements for the degree of Mestre em Engenharia Mecânica.

Advisor : Prof. Florian Alain Yannick Pradelle
Co-advisor : Prof. Sergio Braga Leal

Rio de Janeiro
June 2024

PONTIFÍCIA UNIVERSIDADE CATÓLICA
DO RIO DE JANEIRO

Rayanne Carla Alves do Nascimento

Numerical analysis of the influence of the use of hydrogen as a secondary fuel in Spark-Assisted Compression Ignition engines

Dissertation presented to the Programa de Pós-Graduação em Engenharia de Mecânica of PUC-Rio in partial fulfillment of requirements for the degree of Mestre em Engenharia Mecânica. Approved by the Examination Committee:

Prof. Florian Alain Yannick Pradelle
Advisor
Departamento de Engenharia Mecânica – PUC-Rio

Prof. Sergio Braga Leal
Co-advisor
Departamento de Engenharia Mecânica – PUC-Rio

Dr. Tadeu Cavalcante Cordeiro de Melo
CENPES/PETROBRAS

Prof. Albino José Kalab Leiroz
Departamento de Engenharia Mecânica – UFRJ

Prof. Marcos Sebastião de Paula Gomes
Departamento de Engenharia Mecânica – PUC-Rio

Rio de Janeiro, June 7th, 2024

Rayanne Carla Alves do Nascimento

Rayanne Carla graduated in mechanical engineering in 2017 from Universidade Federal do Rio Grande do Norte (UFRN). Currently, she is a student researcher at the Instituto Tecnológico PUC-Rio (PUC-Rio) in the field of energy and combustion.

Bibliographic data

Nascimento, R. C. A. do

Numerical Analysis of the Influence of the Use of Hydrogen as a Secondary Fuel in Spark-Assisted Compression Ignition Engines / Rayanne Carla Alves do Nascimento; advisor: Florian Alain Yannick Pradelle; co-advisor: Sergio Braga Leal. – 2024.

187 f: il. color. ; 30 cm

Dissertação (mestrado)–Pontifícia Universidade Católica do Rio de Janeiro, Departamento de Engenharia Mecânica, 2024.

Inclui bibliografia

1. Engenharia Mecânica – Teses. 2. Motor de Ignição por Compressão Assistida por Centelha (SACI). 3. Parâmetros de desempenho. 4. Hidrogênio. 5. Análise Numérica. 6. Planejamento de Box-Behnken. I. Pradelle, Florian Alain Yannick. II. Leal, Sergio Braga. III. Pontifícia Universidade Católica do Rio de Janeiro. Departamento de Engenharia Mecânica. IV. Título.

CDD: 621

To my husband and to my family, for
their support and encouragement.

Acknowledgments

To my husband, Adeilson, for his friendship, support, patience, and attention throughout the entire Master course.

To my parents, Raimundo and Aparecida, my sisters Ruth and Rafaella for their support, encouragement, and companionship.

To my advisor professor Florian Alain Yannick Pradelle for his attention, guidance, dedication at all times since the beginning of this research.

To my co-advisor Sergio Leal Braga for his ideas and excitement when teaching and talking about energy researches during Master's subjects.

To the Instituto Tecnológico (ITUC) and the team of Departamento de Engenharia Mecânica (DEM), PUC-Rio, for support, attention, and ideas for solving the problems faced.

To all my friends for being always there for me: to listen, to help, to think together, to laugh.

To CAPES for its essential support in the development of this research. This study was financed in part by the Coordenação de Aperfeiçoamento de Pessoal de Nível Superior - Brasil (CAPES) - Finance Code 001.

Abstract

Nascimento, R. C. A. do; Pradelle, Florian. A. Y. (Advisor); Leal, Sergio B. (Co-Advisor). **Numerical Analysis of the Influence of the Use of Hydrogen as a Secondary Fuel in Spark-Assisted Compression Ignition Engines.** Rio de Janeiro, 2024. 187p. Dissertação de Mestrado - Departamento de Departamento de Engenharia Mecânica, Pontifícia Universidade Católica do Rio de Janeiro.

With the current requirements on emissions and fuel consumption in a context of very strict environmental laws, it is necessary to improve combustion engines performance to reduce greenhouse gas emissions. New technologies, such as Homogeneous Charge Compression Ignition or Spark-Assisted Compression Ignition (SACI), are alternatives to increase engine's efficiency. In this work, a MATLAB routine was created to predict the performance of SACI multimode combustion of methane and methane-hydrogen blends, using a two-zone thermodynamic model. A sensitivity analysis was realized to four performance parameters: thermal efficiency, NOx emissions, CO_2 emissions and energy of the fuel, with several factors' variations such as percentage of H_2, engine speed, fuel-air equivalence ratio, intake pressure and valve overlap, using experimental design tools to evaluate the impact of those factors over the performance parameters. The Box-Behnken Design indicated that engine speed, percentage of H_2 and intake pressure are the most important SACI factors since they influence all engine performance parameters. On the other hand, fuel-air equivalence ratio was relevant in only one of them (NOx) and the valve overlap, as it was used in the experiments, showed no relevant impact on the results. Furthermore, a Univariate Analysis was done to compare Spark-Ignition and SACI engines efficiencies. The results showed that SACI engines performs better, with 7% - 17% higher efficiency and 90% - 96% IMEP's increase.

Keywords

Spark-Assisted Compression Ignition (SACI); Performance Parameters; Hydrogen; Numerical Analysis; Box-Behnken Design.

Resumo

Nascimento, R. C. A. do; Pradelle, Florian. A. Y. (Advisor); Leal, Sergio B. (Co-Advisor). **Análise Numérica da Influência do Uso de Hidrogênio como Combustível Secundário em Motores de Ignição por Compressão Assistida pela Centelha.** Rio de Janeiro, 2024. 187p. Dissertação de Mestrado - Departamento de Departamento de Engenharia Mecânica, Pontifícia Universidade Católica do Rio de Janeiro.

Com os atuais requisitos sobre emissões e consumo de combustível em um contexto de leis ambientais mais rigorosas, é necessário melhorar o desempenho dos motores de combustão para reduzir as emissões de gases do efeito estufa. Novas tecnologias, como Ignição por Compressão de Carga Homogênea (HCCI) ou Ignição por Compressão Assistida por Centelha (SACI), são alternativas para aumentar a eficiência dos motores. Neste trabalho, foi criada uma rotina MATLAB para prever o desempenho da combustão SACI multimodo de metano e misturas metano-hidrogênio, utilizando um modelo termodinâmico de duas zonas. Foi realizada uma análise de sensibilidade a quatro parâmetros de desempenho: eficiência térmica (η_{th}), emissões de NOx, emissões de CO_2 e energia do combustível (E_{fuel}), com diversas variações de fatores tais quais porcentagem de H_2, rotação do motor, relação de equivalência combustível - ar, pressão de admissão e superposição de válvulas, utilizando ferramentas de planejamento de experimentos para avaliar o impacto dos fatores sobre os parâmetros de desempenho. O Planejamento Box-Behnken indicou que rotação do motor, porcentagem de H_2 e pressão de admissão são os fatores SACI mais importantes, pois influenciam todos os parâmetros de desempenho do motor. Por outro lado, a relação de equivalência combustível - ar foi relevante para apenas um deles (NOx) e a superposição de válvula, como foi utilizada nos experimentos, mostrou nenhum impacto relevante sobre os resultados. Além disso, foi feita uma Análise Univariada para comparar motores de ignição por centelha e SACI. Os resultados mostraram que os motores SACI apresentam melhor desempenho, sendo cerca de 7% - 17% mais eficientes e um aumento de 90% - 96% no IMEP.

Palavras-chave

Motor de Ignição por Compressão Assistida por Centelha (SACI); Parâmetros de desempenho; Hidrogênio; Análise Numérica; Planejamento de Box-Behnken.

Table of Contents

List of figures

LIST OF TABLES

Nomenclature

Acronyms

AIT	Auto-Ignition Timing
aBDC	After Bottom Dead Center
aTDC	After Top Dead Center
BBD	Box-Behnken Design
bBDC	Before Bottom Dead Center
BDC	Bottom Dead Center
BEV	Battery Electric Vehicle
bTDC	Before Top Dead Center
CAD	Crank Angle in Degrees
CCUS	Carbon Capture, Utilization, and Storage
CI	Compression Ignition
CNG	Compressed Natural Gas
DoE	Design of Experiments
EAR	Excess Air Ratio
eEGR	external Exhaust Gas Recirculation
EGR	Exhaust Gas Recirculation
EIVO	Early Intake Valve Opening
EPE	Energy Research Office
EVC	Exhaust Valve Opens
EVO	Exhaust Valve Closes
ETF	Enhanced Transparency Framework
FCEV	Fuel Cell Electric Vehicles
GHG	Greenhouse Gases
HCCI	Homogeneous Charge Compression Ignition
HRR	Heat Release Rate
ICE	Internal Combustion Engine
iEGR	internal Exhaust Gas Recirculation
IMEP	Indicated Mean Effective Pressure
IVC	Intake Valve Opens
IVO	Intake Valve Closes
LEVC	Late Exhaust Valve Closing
LOHC	Liquid Organic Hydrogen Carrier
LPG	Liquid Petroleum Gas
LT-LEDS	Long-Term Low Greenhouse Gas Emission Development Strategies
NDC	Nationally Determined Contributions
NVO	Negative Valve Overlap
NZE	Net Zero Emission
PLIF	Chemiluminescence and Planar Laser Induced Fluorescence
PODE	PolyOxymethylene Dimethyl Ether
PVO	Positive Valve Overlap

SACI	Spark-Assisted Compression Ignition
SI	Spark Ignition
SI-HCCI	Spark Ignition - Homogeneous Charge Compression Ignition
SICI	Spark-Induced Compression Ignition
SPCCI	Spark Controlled Compression Ignition
TDC	Top Dead Center
WACC	Weighted Average Costs of Capital
WOT	Wide-Open Throttle

Symbols

A	$[m^2]$	Cylinder lateral area
a_W	$[-]$	Wiebe efficiency factor
a_{AI}	$[-]$	Auto-ignition a coefficient
B	$[m]$	Cylinder bore
b_{AI}	$[K]$	Auto-ignition b coefficient
c_p	$[kJ/(kg \cdot K)]$	Specific heat capacity at constant pressure
$C_1 and\ C_2$	$[-]$	Woschni constants
$E_{a_{AI}}$	$[J/mol]$	Auto-ignition activation energy coefficient
h	$[kJ/kg]$	Specific enthalpy
KI	$[-]$	Knock-integral
L	$[m]$	Connecting-rod length
MW	$[kg/kmol]$	Molecular weight
m	$[kg]$	In-cylinder mass
k_W	$[-]$	Wiebe form factor
N_{cyl}	$[-]$	Number of cylinders
Nu	$[-]$	Nusselt number
n	$[mol]$	Amount of substance
n_{AI}	$[-]$	Auto-ignition n coefficient
P	$[kPa]$	In-cylinder pressure
P_{int}	$[kPa]$	Pressure at the intake manifold
R	$[m]$	Crank radius
Re	$[-]$	Reynolds number
r	$[kJ/(kg \cdot K)]$	Specific gas constant
r_c	$[-]$	Compression ratio
S	$[m]$	Cylinder stroke
$\overline{S_p}$	$[m/s]$	Mean piston speed
s	$[kJ/(kg \cdot K)]$	Specific entropy
T	$[K]$	Temperature
t	$[s]$	Time
u	$[kJ/kg]$	Specific internal energy
v	$[m^3/kg]$	Specific volume
V	$[m^3]$	Cylinder volume
V_{BDC}	$[m^3]$	Bottom Dead Center volume
V_d	$[cm^3]$	Displacement volume
V_d^{tot}	$[cm^3]$	Total displacement volume

V_{TDC}	$[m^3]$	Top Dead Center volume
x	$[-]$	Mass fraction
w	$[m/s]$	Average cylinder gas velocity
y	$[-]$	Molar fraction

Greek letters

α	$[W/(m^2 \cdot K)]$	Heat transfer coefficient
γ	$[-]$	Heat capacity ratio
ϵ	$[-]$	Half-stroke to rod ratio
η	$[-]$	Efficiency
θ	[°]	Crank angle
ξ	$[-]$	Nitric oxide concentration to its equilibrium value ratio
τ	$[s]$	Auto-ignition delay time
ϕ	$[-]$	Fuel-air equivalence ratio
ω	$[rad/s]$	Angular velocity
ζ	$[-]$	Extent of precursor reaction

Subscripts and superscripts

amb	Ambient
avg	Average
b	Burned gas
c	Critical
d	Combustion duration
exh	Exhaust
int	Intake
IVC	Intake Valve Closing
m	Motored
p	Precursor
s	Start of combustion
tot	Total
th	Thermal
u	Unburned gas
v	Volumetric
W	Wiebe function

“It is not the strongest of the species that survives,
not the most intelligent that survives.
It is the one that is the most adaptable to change.”
Charles Darwin

1 Introduction

1.1. Motivation

The climate change over the last decades has become a main subject since many significant agencies and scientists have been studying and alerting about the effects of human action on the environment (NOAA CLIMATE.ORG, 2022). Earth's temperature has risen by 0.08°C per decade since 1880, but the rate of warming since 1981 is more than two times that: 0.18°C per decade (LINDSEY; DAHLMAN, 2022). As one of these natural resources, energy has turned into one of the most relevant fields of scientific research over the years. Due to that it is necessary that the management of this resource follow a path of more conscious and renewable consumption.

In the last decade the political pressure to regulate the emissions of Greenhouse Gas (GHG) has grown significantly after the Paris Agreement at COP 21, signed by 196 countries, in December 2015. "Its goal is to limit the global warming to well below 2, preferably 1.5 degrees Celsius, compared to pre-industrials levels" (IEA, 2021). Since the climate change started to severely affect lives and environment worldwide, it was inevitable that countries had to start to make commitments about economic and social transformations.

By 2020, plans for climate actions were stablished by the countries that signed the Paris Agreement known as Nationally Determined Contributions (NDCs). These NDCs intend to list the actions that will be taken to lower GHG emissions with the purpose to limit the global warming. Beyond it, countries have settled an Enhanced Transparency Framework (ETF). Under it, they will have "to report transparently on actions taken and progress in climate change mitigation, adaptation measures and support provided and received" starting in 2024. This amount of information will provide content to global stocktake which shall evaluate collective progress towards the long-term climate goals. Therefore, it will allow recommendations of more ambitious plans for countries to set in next cycles (UNFCCC, 2020).

Thus, global energy-related CO_2 emissions rose to an amount of 37 Gt in 2022 (IEA, 2023c). Regarding GHG emissions, the global transport sector accounts for around 25% of CO_2 emissions (8 Gt CO_2) in 2021 (IEA, 2022). The

transport sector in Brazil was responsible for 200.2Mt of CO_2 emissions in 2021 (IEA, 2021), contrasting with 1.26 Gt of CO_2 emissions from deforestation to commodities production (WRI, 2024).

It is noteworthy that people's quality of life directly depends on trustable supply of energy at an accessible price. Considering that it is necessary to control temperature of houses, to cook and save food, to build structures as hospitals, stadiums, schools, roads, etc. and to stay connected to the world, the future of energy consumption must be reshaped from now for the safety of next generations (BRUYNINCKX, 2017).

Global economy still strongly relies on burning fossil fuels. This scenario will not change from one day to another. It takes time to change the main rule that keeps economy normally functioning. And that is why it is so important that the pattern of consumption keeps evolving from the actual one, that mainly uses not green types of energies, to one that uses mixed types of energies, primarily based on green types.

Nowadays the most used means of transport are still those that depend on Internal Combustion Engines (ICE), mainly land-based ones. Internal combustion engines are commonly known in two types of combustion: Spark Ignition engines (SI) and Compression Ignition engines (CI). These engines operate according to the cycles designed by Nikolaus Otto and Rudolf Diesel, respectively, which are the combustion techniques typically used for ICEs. Due to this, they can also be cited as Otto and Diesel-cycle engines (LEITE, 2021).

Increasing concerns regarding the dependence of current energy systems on fossil fuels have raised the demand for more efficient engines and green alternative fuels in order to drive a sustainable energy future with a carbon-free economy (KURIEN; MITTAL, 2023). In general, ICE use liquid fuels (mostly fossil ones as gasoline and diesel oil, but also bioethanol and biodiesel), but some of them can also use natural gas or biomethane as fuel. Among the alternatives, studies about the use of low-carbon hydrogen as fuel for ICE are in expansion due to its decarbonization potential to the transport sector.

The lack of infrastructure needed to use hydrogen as an enabler of decarbonization of the energy sector limits the actual growth prospects for this fuel, whose implementation is affected by issues related to storage and distribution of hydrogen energy (KURIEN; MITTAL, 2023). In 2021, the use of hydrogen for mobility application represented 0.03% of the global market share of hydrogen (IEA, 2023a).

In addition, other models of combustion techniques beyond the traditional ones have been developed to improve the performance of the engines. They will be cited in the following sections of this document, named as Homogeneous Charge Compression Ignition Engine (HCCI) and Spark-Assisted Compression Ignition Engine (SACI).

1.2.Objectives

This thesis has as its main objective the development of a numerical study of the SACI technology, using natural gas and hydrogen as fuel to analyze the improvement of thermal performance and reduction of emissions, under different operating conditions using a Design of Experiments (DoE) approach. Engine speed, fuel-air equivalence ratio, spark timing, compression ratio, and intake pressure will be investigated, with the support of a two-zone thermodynamic 0D Matlab® routine. The simulation, improving the work developed by Leite (2021), will assist the comprehension of the engine's key performance parameters, i.e., thermal efficiency, indicated mean effective pressure, NOx emissions, mean in-cylinder temperature, and auto-ignition timing.

For this purpose, this work has three specific objectives:

I. Allow the simulator to model the simultaneous opening of intake and exhaust valves to have negative, none or positive valve overlap.
II. Investigate the impact of the heat transfer model.
III. Turn the simulator able to simulate the combustion of hydrogen.

Satisfactory results from the application of this simulator can contribute to technical depth and discussions on the subject.

1.3.Thesis Structure

A bibliographic review about SACI engines technology is presented in Chapter 2. The differences between its combustion and the ones from SI, CI, and HCCI engines are evidenced.

In Chapter 3, the modeling of SACI engines is discussed. The hypothesis assumed are justified and the thermodynamic and chemical approaches for each of the four strokes are presented. The criterion for the autoignition and the combustion curve for SI-HCCI combustion is also proposed.

The calculation procedure and the examples analyzed are described in Chapter 4. In Chapter 5, the operating point's mapping is studied for optimized ICE

systems with SACI vs. SI comparison. Thus, the SACI operation results are shown and discussed.

Finally, Chapter 6 provides the main conclusions of this work and suggests future research on the theme.

2 Literature Review

2.1. Transports and Hydrogen Scenario

People constantly go from one place to another, and commodities are traded across the world through distances farther than ever. Consequently, big part of the carbon consumption comes from transports. In 2021, transport emissions were responsible for about 23% of the CO_2 global emissions (IEA, 2022). These emissions primarily involve road, rail, air, and marine transportation. And besides other sectors of industries, the transportation sector emissions are expected to keep growing faster than the other ones (WANG; GE, 2019). It shows the major challenge that is necessary since the Paris Agreement in 2015. The decarbonization process of global industries expected from NDCs enables the changes in transport sector to provide a cleaner, healthier, and more affordable future.

CO_2 emissions from energy combustion and industrial processes were responsible for around 89% of energy-related greenhouse gas emissions in 2022 (IEA, 2022). However, while the world needs to reduce their own emissions, the transport emissions show a pattern of growth. Even though the efficiency of the vehicles is being improved, the number of travels keeps growing faster. As an example of this, after United States experimented a decline of the peak of emissions in 2005, it started to grow again and since 2012 keeps growing every year (WANG; GE, 2019; WRI, 2023). In 1990, the top three of transportation GHG emitters were United States, Russia, and Japan. After 1999, China increased its emissions in this field and nowadays emits more than India and Russia, becoming the second largest CO_2 emitter of transportation (WRI, 2023).

Analyzing the types of transports, road vehicles are responsible for about 79% of transportation global emissions and responsible for 70% of the increase in the transport sector emissions from 1990 to 2022. The emissions from other types of vehicles have also increased, like international and domestic aviation and costal and international marine transportation. Walking through a different path, railways emissions have decreased, mostly because of the use of electricity as source of energy (IEA, 2023c; STATISTA, 2024).

In regard to countries, those ones which have an income rate high or upper-middle are the most responsible for the GHG emissions of transport sector. In 2023, the ten countries that contributed more for the transport global emissions were United States, China, India, Russia, Brazil, Japan, Canada, Mexico, Germany, and Iran, in descending order. Their amount of transport global emissions corresponded to 51% in 2023 (IEA, 2023c; STATISTA, 2024).

Brazil, placing as the fifth largest country responsible for polluting emissions in the transport sector (Figure 2.1), has a key role in the direction that climate change will follow in the coming years, even though Brazil's emissions represents, respectively, just 12% and 24% of United States and China emissions and 20% of Europe emissions (Figure 2.2) (CRIPPA et al., 2023; EDGAR/JRC, 2023; STATISTA, 2024).

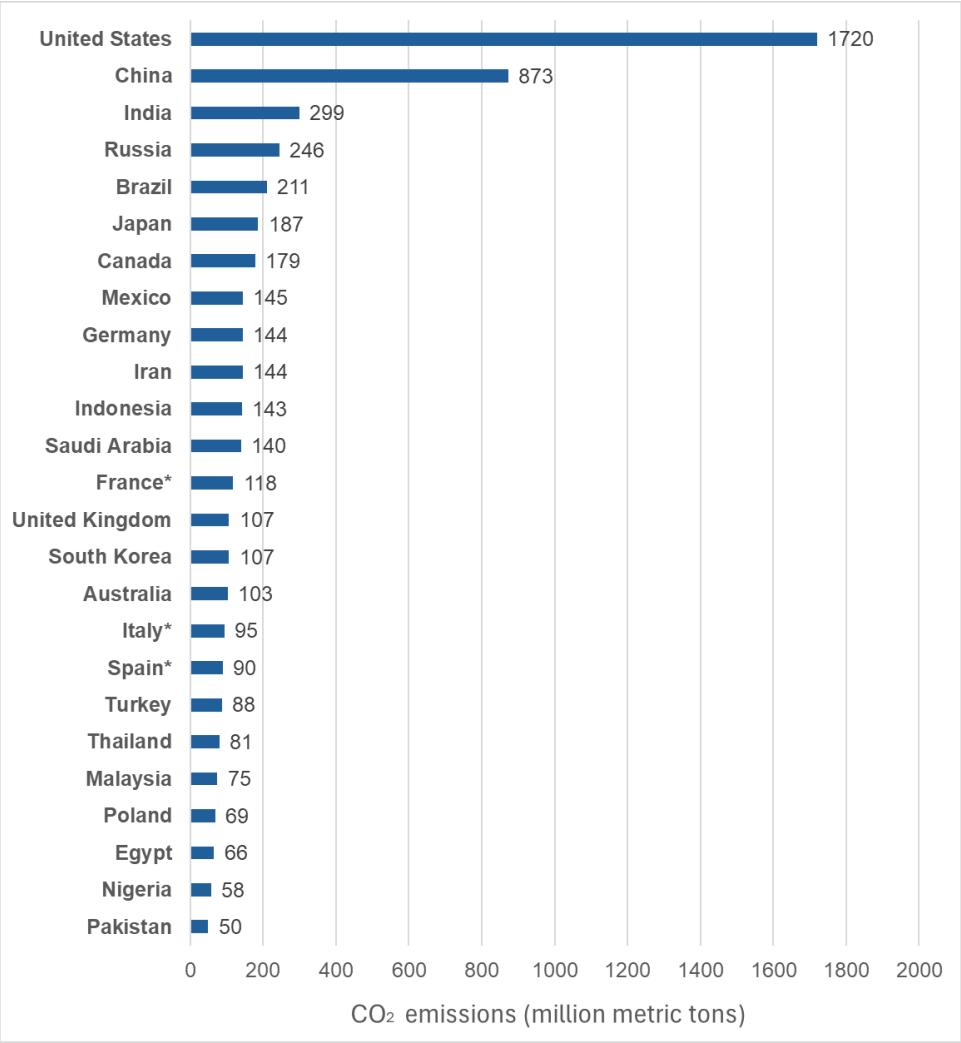

Figure 2.1. Carbon dioxide emissions of the transportation sector worldwide in 2022, by select country ($MtCO_2e$). Source: (EDGAR/JRC, 2023), author own elaboration.

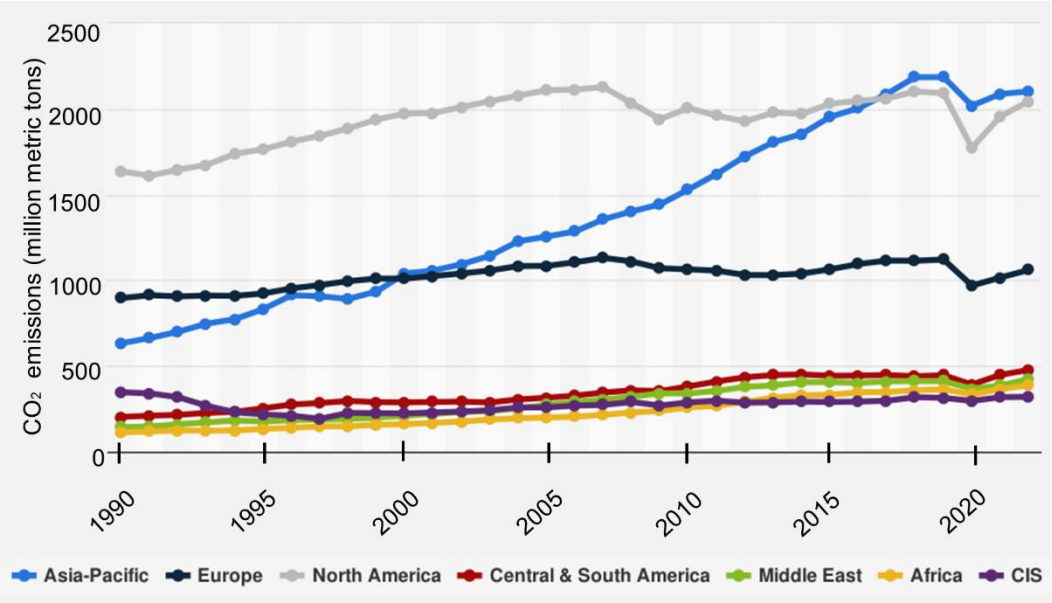

Figure 2.2. Carbon dioxide emissions of the transportation sector worldwide from 1990 to 2022, by region ($MtCO_2e$). Source: (EDGAR/JRC; STATISTA, 2023), adapted by the author.

The average volume of oil derivatives consumed by the world, and by Brazil, in the transport sector are in first place. Figure 2.3 and Figure 2.4, from the Brazilian Energy Balance 2022 (BEN 2022) produced by Energy Research Office (EPE, 2023), respectively show the levels of consumption in the world and in Brazil for periods between 1970 and 2021. From Figure 2.3, it can be seen the actual world consumption of oil derivatives in transportation is above of 65%. Analyzing Figure 2.4, it is notable that around 60% of the oil consumption in Brazil goes to transportation.

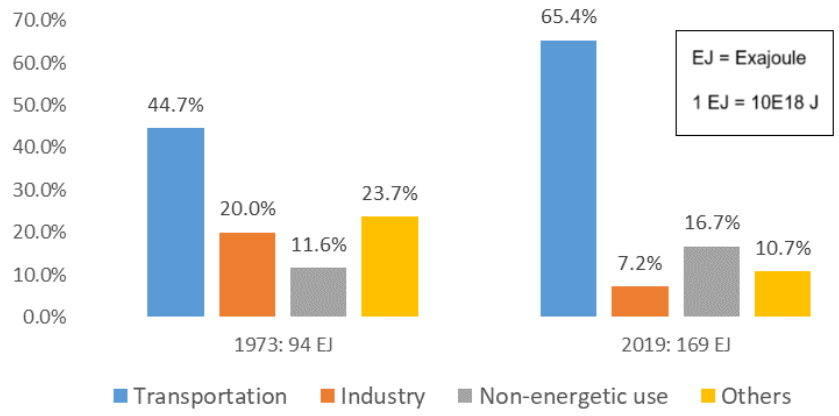

Figure 2.3: Sectorial consumption of oil products for world data in the period of 1973-2019, last year pre-COVID pandemic. Source: (EPE, 2023), author's own elaboration.

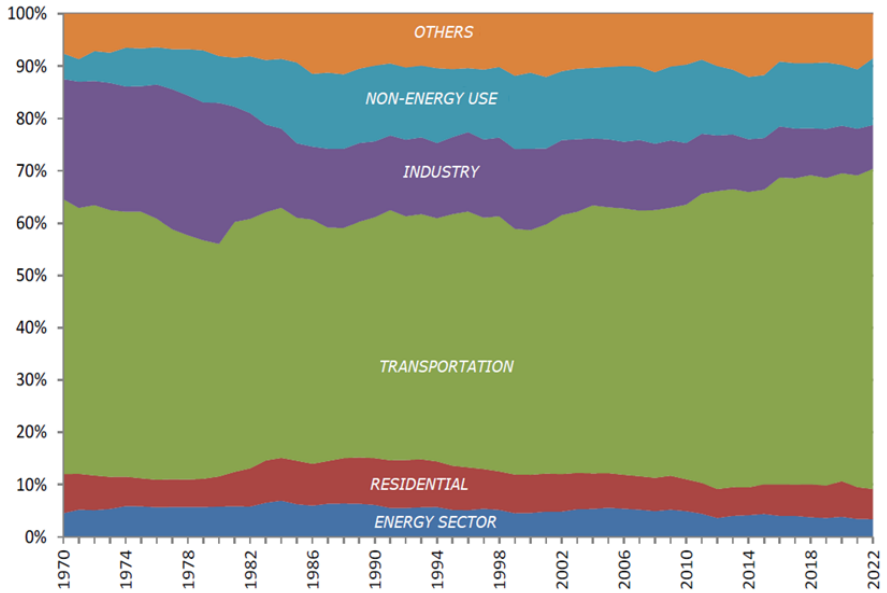

Figure 2.4: Oil products consumption by sector for Brazil in the period of 1970-2022. Source: EPE for Brazil, edited by the author.

Reducing CO_2 emissions to net zero by 2050 is adequate to the efforts settled in Paris Agreement as necessary to keep the global warming up to 1.5 °C. The path to this achievement is narrow and requires massive development of all available clean and efficient energy technologies. So, to make it real, the 2020s must become a decade of greater clean energy expansion. Achieving the net zero emission (NZE) requires a broad range of mitigation actions to severely reduce the GHG emission through the period of 2020-2050. The decarbonization pillars are energy efficiency, behavioral changes, electrification, renewables, hydrogen and hydrogen-based fuels, bioenergy, and carbon capture, utilization, and storage (CCUS) (IEA, 2021).

At a global level, renewable energies are the essential solution to the reduction of electricity supply. The share of renewable energies needed in total worldwide electricity generation to achieve NZE by 2050 must grow from 29% in 2020 to more than 60% in 2030 and to approximately 90% in 2050. Renewables play an important role in the reduction of pollutant emissions. They can be used directly or indirectly, by consumption or transformation of the energy generated. In transport sector, renewables can be used to reduce emissions by producing electricity to power electric vehicles or producing biofuels or biomethane (IEA, 2021).

Due to water scarcity and the activation of substitutive thermoelectric plants, the share of renewables in the Brazilian energy matrix was marked by a drop between 2020-2021 (EPE, 2023) caused by the decrease in the supply of hydraulic energy. But unlike the rest of the world, Brazil is one of the countries with the greatest presence of renewable energies in its energy matrix accounting for 47.4% in 2022, while OCDE and World accounted in 2020 for 11.5% and 14.1% respectively. According to EPE and IEA data, the presence of renewable energies in Brazil energy matrix have grown almost 7% from 2013 to 2022 (EPE, 2023; IEA, 2023c). In this way, Brazil's role in this scenario of changes in energy standards is of such relevance to reach the NZE by 2050 and influence nations to follow the same path based on its example.

The use of decarbonized fuel contributes to the energy transition. Low-emission hydrogen (water electrolysis with renewable electricity or production from biomass, or synthesis from fossil fuels with CCUS technology) has emerged as an important tool for decarbonizing sectors in which emissions are hard to abate. Governments have strengthened their commitments to achieve NZE, and low-emission hydrogen has become an integral part of their plans (IEA, 2023a).

The initial focus to achieve the NZE by hydrogen use is the conversion of existing uses of fossil fuels to low-carbon hydrogen in terms that do not request promptly big transformations in actual infrastructure of energy transmission and distribution. This includes hydrogen use in industry, refineries and power plants, and the blending of hydrogen into natural gas for distribution to end-users (IEA, 2023c).

Theoretically, hydrogen can also be used in a wide range of other applications, as a raw material or reducing agent, and also as a fuel. Hydrogen has not been used at scale in these applications for mobility, either because low-emission technological alternatives are uncompetitive when compared to existing fossil fuels or because its end-use technologies have not reached commercial maturity. Although, decarbonization efforts are expected to encourage the use of hydrogen in some of these new applications, particularly in sectors where emissions are difficult to reduce, and other low-emission technologies are not available or very difficult to implement.(IEA, 2023a)

Hydrogen use grew strongly in all major consuming regions except Europe. In Europe, hydrogen use took a big hit due to reduced activity in recent years. In contrast, North America and the Middle East saw strong growth (around 7% in both cases), which more than offset the decline in Europe. In China, use grew more modestly (around 0.5%), but the country remains the largest single consumer of

hydrogen by far, accounting for almost 30% of global hydrogen use (more than double the second largest consumer, the United States) (IEA, 2023a). In the IEA's updated 2023 Net Zero Emissions by 2050 Scenario (NZE Scenario), hydrogen use is projected to grow by 6% annually by the end of this decade. This implies achieving over 150 Mt of hydrogen use by 2030, with almost 40% coming from new applications (IEA, 2023b).

As in previous years, the growth in global hydrogen use is not the result of hydrogen policies, but rather global energy trends. Virtually all of the increase occurred in traditional applications, mainly refining and the chemical sector, and was met by increased production based on unreduced fossil fuels. This means that the growth has had no benefit for climate change mitigation purposes. The uptake of hydrogen in new applications in heavy industry, transport, production of hydrogen-based fuels or electricity generation and storage – which is key to the clean energy transition – remains minimal, accounting for less than 0.1% of global demand (IEA, 2023a).

Hydrogen use in road transport increased by around 45% in 2022 compared to 2021 primarily in fuel cell electric vehicles (FCEV), albeit from a relatively low starting point. To get on track with the NZE Scenario, it will be important to accelerate the adoption of hydrogen and hydrogen-based fuels and advance technologies that are still pre-commercial today. Under the NZE Scenario, almost 8 Mt of hydrogen is projected to be used directly in transportation by 2030, mainly in the road (50%) and maritime (45%) sectors. In addition, another approximately 8 Mt of hydrogen is projected to be used for the production of ammonia and synthetic fuels for use in shipping and aviation. (IEA, 2023a).

In cars and vans sector, Porsche and Toyota have developed prototype cars using hydrogen combustion engines. In trucks sector, Technocarb and CMB.TECH companies developing activities of hydrogen combustion by retrofitting diesel engines. New Zealand is also trialing hydrogen combustion, though in dual-fuel vehicles (IEA, 2023a).

Global hydrogen use reached 95 Mt in 2022, a nearly 3% increase from the 2021's IEA estimative, continuing the growing trend that was only interrupted in 2020 as a consequence of the COVID-19 pandemic and the economic slowdown (IEA, 2023a). As in 2021, 2022 production was dominated by continued use of fossil fuels. Natural gas without CCUS accounted for 62% of global production, while unabated coal, mainly located in China, accounted for 21% of global production. Byproduct hydrogen, which is produced in refineries and the petrochemical industry during naphtha reforming, often used for other refining and

conversion processes (e.g. hydrocracking, desulfurization), accounted for 16% of global production. (IEA, 2023a).

Low-emission hydrogen production in 2022 was less than 1 Mt (0.7% of global energy production), very similar to 2021 and almost entirely from fossil fuels with CCUS. Water electrolysis production continued to be relatively small, still below 100 kt H_2 in 2022, representing a 35% growth compared to the previous year. At a regional level, China was responsible for almost 30% of global production, reflected by large domestic demands for refineries and the chemical industry. More than 70% of global production was in China, United States, Middle East, India and Russia in 2022 (in descending order by production share) (IEA, 2023a).

The cost of hydrogen production depends on the technology and cost of the energy source used, which often has significant regional differences. Before the recent global energy crisis, the levelized cost of producing hydrogen from unattenuated fossil sources was in the range of $1.0-3.0/kg H2. As of 2021, these production routes offer the cheapest option to produce hydrogen, compared to using fossil fuels with CCUS ($1.5-3.6/kg H2) or using electrolysis with low-emission electricity ($3.4-12/kg H2) (IEA, 2023a).

The cost of hydrogen produced using electrolysis is driven by the capital cost of the electrolyzers and the cost of the electricity used to power the electrolyzer. If large-scale deployment occurs as envisioned in the NZE Scenario, the costs of producing electrolytic hydrogen using electricity from solar photovoltaic (PV)-based could fall to US$1.6/kg H_2 by 2030 in regions with excellent solar irradiation such as Africa, Australia, Chile, China and Middle East. While solar PV-based electrolysis could become the cheapest way to produce hydrogen by the end of the decade, locations with excellent wind resources (offshore or onshore) could also see a significant drop in the levelized cost of hydrogen, reaching values below US$2.1/kg H_2 in northwestern Europe and below US$2.3/kg H_2 in the United States (IEA, 2023a).

Hydrogen production from renewable electricity is a capital-intensive production route. Initial investments are not only required for the electrolyzer, but also for the generation of renewable electricity. In the current context of rising interest rates, rising weighted average costs of capital (WACC) can have a profound impact on the economic viability of projects and their hydrogen production costs. For example, an increase in WACC from 5% to 10% results in a nearly 40% increase in hydrogen production costs, depending on the renewable electricity source. For project developers in emerging and developing economies in

particular, access to finance can be a major barrier, reflected in a WACC that is generally higher compared to advanced economies. An increase in WACC from 6% to 15%, for example, would increase the cost of hydrogen production from solar PV by more than 70%.(IEA, 2023a).

The cost of producing hydrogen from natural gas with CCUS is strongly influenced by the price of natural gas and its fluctuations. The impact of WACC on the cost of producing hydrogen from natural gas with CCUS is much smaller than for renewable hydrogen produced with electrolysis, given that the cost of production from electrolysis using renewable electricity is almost entirely CAPEX-based, while for production from natural gas the share of CAPEX is 5-30%(IEA, 2023a).

Infrastructure for transporting and storing hydrogen is an important enabler for hydrogen trade. However, as hydrogen has a relatively low volumetric energy density and low liquefaction temperature, transporting and storing hydrogen is technically more challenging than handling fossil fuels today. These include the need to liquefy or compress hydrogen or convert hydrogen to carriers such as ammonia or liquid organic hydrogen carrier (LOHC). Developing commercial hydrogen trade would involve complexities that would require careful consideration of cost, benefits and potential trade-offs in exporting and importing countries. (IEA, 2023a).

Today, hydrogen trade flows are limited to some existing hydrogen pipelines connecting industrial areas and some pilot projects to demonstrate hydrogen trade by ship. The only exceptions are ammonia and methanol, which are already traded globally as raw materials for the chemical industry. Around 10% of global ammonia demand was met through international trade in 2021, and for methanol the commercial share was 20%. Nevertheless, existing trade is tied to use in the chemical industry, and international trade of ammonia and methanol for fuel purposes has only been tested in a few early pilot projects. (IEA, 2023a).

Three-quarters of the export-oriented projects planned for 2030 or earlier are still in the early stages of development, and just under a quarter are undergoing a feasibility study. Additionally, less than a third of the volume that could be traded by 2030 has already identified a potential buyer. The realization of the announced commercial projects will depend not only on the implementation of the production unit and the necessary infrastructure, but also on the guarantee of one or more long-term buyers: these two aspects must be pursued in parallel to ensure that the projects are carried out on time and are economically sustainable. Despite the strong momentum surrounding hydrogen export announcements in recent years,

the small proportion of commercial projects that have reached advanced planning stages demonstrates significant uncertainty around the ability to develop an export market at scale in the next decade. (IEA, 2023a).

Many projects are at an early stage of development and for several of them the carrier has not yet been chosen. By 2040, around 5% of the volume traded based on announced commercial projects could be in the form of synthetic liquid hydrocarbons, 4% as compressed gaseous hydrogen via pipeline and 2% in the form of liquefied hydrogen. The cost of transporting hydrogen from the exporting region to the importing region can be substantial and therefore assessing the total cost of supply – for both production and transport – is essential. Depending on the carrier and the distance of transport, transport costs can shift the competitiveness in favor of domestic production. A current obstacle to trade is the lack of a common internationally agreed methodology for determining the emissions intensity of hydrogen, which could potentially lead to a fragmented market for hydrogen. (IEA, 2023a).

Transport and storage are critical elements of the low-emission hydrogen supply chain. Infrastructure is needed not only to connect regions where low-emission hydrogen can be produced at low cost with demand centers and to manage fluctuations in production and demand, but also to ensure system resilience in the event of supply disruptions. Under the NZE Scenario, annual global investment in low-emission hydrogen and hydrogen-based fuel transportation, including pipelines, storage facilities, terminals and refueling stations, is projected to reach approximately USD 35 billion in the second half of this decade. This amount represents approximately 40% of current annual spending on natural gas pipelines and transportation infrastructure (IEA, 2023a).

To transport hydrogen over long distances where pipeline transmission is not feasible, or in regions without suitable geological conditions for underground storage, hydrogen needs to be converted to denser forms. Among these alternatives, liquefied hydrogen (LH_2) or carriers like ammonia and LOHCs are promising options. However, although the conversion of hydrogen to ammonia for use as ammonia is already well established, if conversion back to hydrogen is required, the necessary technologies are not yet available on a commercial scale. (IEA, 2023a).

As previously mentioned, United States, China, Russia, India, Brazil are the five largest emitters of GHG in the transport sector. Therefore, their fleet of vehicles, that rely on fossil fuels, are significantly large. Making a change in this sector should happen gradually, since severe changes include drastic effects on

the population's lifestyle, on the infrastructure of the land transport road network and on the country's economy (IEA, 2023c).

Due to all this need about decarbonizing the world, light duty vehicles usage has been projected to decrease in North America and Europe until 2050. On the other hand, Asia has shown a potential to have cars as a prevailing transportation mode up to the NZE. Asian car use is projected to grow more than 40% of trips taken in the next three decades. The share of these trips taken by Asian population by car would reach the Europe level (44%) and Latin America level (42%) by 2050 (WEF, 2021).

Although Asia Pacific has some of the most advanced public transport systems in the world, the social inequality between rural and urban areas and the development disparities of countries could increase expeditiously the motorization as the continent develops (WEF, 2021). With data of the report 21st Century Cities: Asia Pacific's Urban Transformation (GREEN; FANSHAWE; CREPALDI, 2021), these statistics can be seen in Figure 2.5.

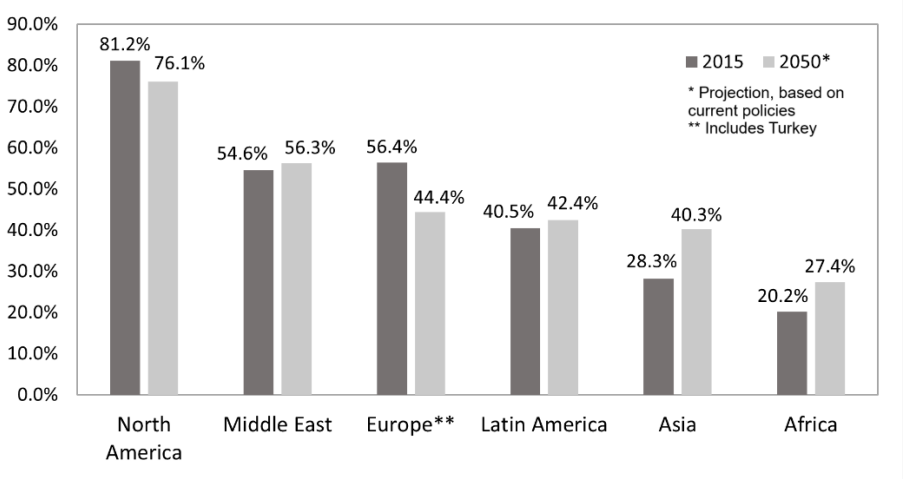

Figure 2.5: Share of all trips taken by car in 2015 and 2050, by world region (in percent). Source: (GREEN; FANSHAWE; CREPALDI, 2021), author's own elaboration.

Decarbonizing road transportation is important for meeting long-term low greenhouse gas emission development strategies (LT-LEDS), onto achieving the goal of the Paris Agreement. Since 2015, government policies regarding to decarbonize road transportation have shown a tendency to achieve those strategies by establishing a society more efficient in transportation field, with more energy efficient vehicles, larger shares of renewable fuels and faster introduction of battery electric vehicles (BEV) (MORFELDT; DAVIDSSON KURLAND;

JOHANSSON, 2021). However, GHG impact of BEV could be worse than the one caused by conventional vehicles if the electricity generation and the energy used for battery production are not properly decarbonized. Beyond that, if coal remain to be a significant part of the energy options, as it still is in China and India, and if this power generation keeps near urban centers, local urban air quality in terms of noxious emissions, such as nitrogen oxides and sulfur dioxide, would get worse (KALGHATGI, 2018).

Around 95% of the energy source for transportation comes from liquid fossil fuels and around 60% of all oil produced in the world is used to produce transport fuels. The major replacement options to liquid fossil fuels are biofuels, compressed natural gas (CNG) and liquid petroleum gas (LPG), which together correspond to a share around 5% of total global transport energy. The share that corresponds to actual use in transportation of electricity is small and of hydrogen or synthetic fuels, negligible. There are many researchers across the world studying and developing alternatives – especially electricity. The influences in evolution of the transport energy supply chain depend on the complex interplay between several factors as shown in Figure 2.6 and it will evolve distinctly in different parts of the world. Thus, projections suggest that by 2040 around 90% of transport energy will still come from liquid fossil fuels used in ICEs (KALGHATGI, 2018).

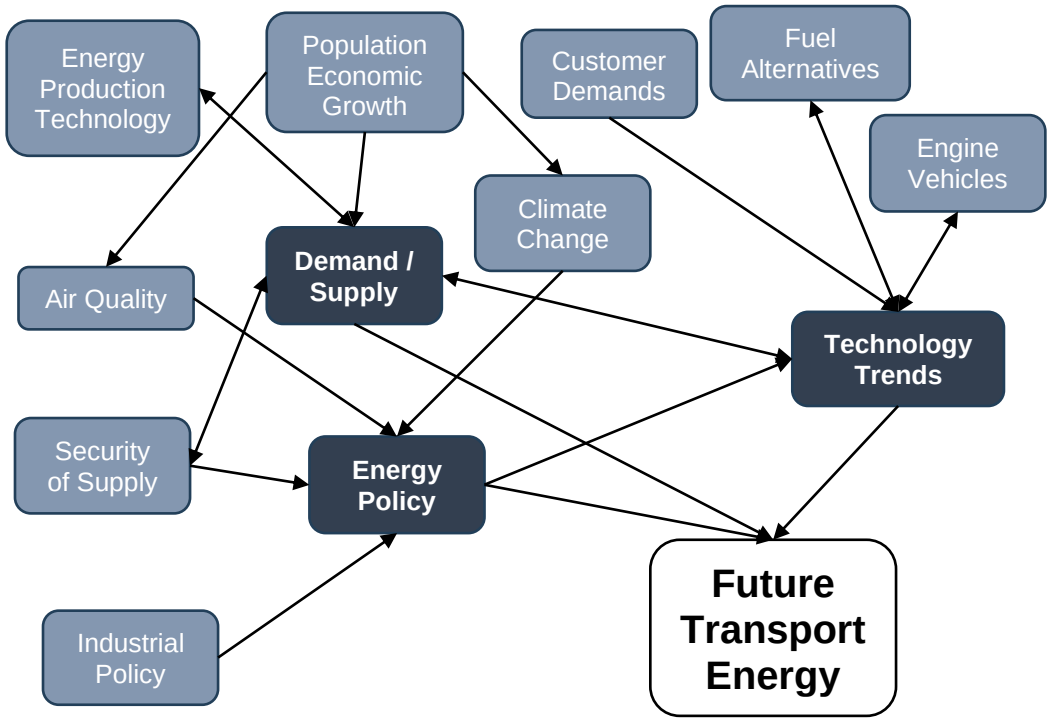

Figure 2.6: The influences in evolution of the transport energy supply chain
Source: (KALGHATGI, 2018), author's own elaboration.

2.2.ICEs Typical Combustion Cycles

ICEs are typically classified in two forms: two-stroke engines and four-stroke engines. This classification is based on the type of cycle to produce work. The two-stroke engine completes its power cycle in only one crankshaft revolution, with two strokes – up and down movements of the piston. The four-stroke engine proceed in two crankshaft revolutions, with four phases: intake, compression, power, and exhaust. The four-stroke engine cycle has been studied during several decades to make improvements and develop a cycle that turn possible to the ICEs work better through the years. The following subsections will present the most relevant ones for the study of Spark-Assisted Compression Ignition Engines.

2.2.1. Four-Stroke Spark Ignition Engine (SI)

The Otto cycle is the ideal cycle for spark ignition reciprocating engines. It owes its name to Nikolaus A. Otto, who successfully created a four-stroke engine in 1876, in Germany, starting from the cycle proposed by the Frenchman Beau de Rochas in 1862. Commonly in spark ignition engines, the piston operates through four full strokes (two mechanical cycles) within the cylinder, and the crankshaft executes two revolutions for each thermodynamic cycle. These engines are called four-stroke internal combustion engines (ÇENGEL; BOLES, 2013).

The sequence followed by the SI engine goes through four steps, as indicated below, and showed in Figure 2.7:

I. Compression stroke

   Initially, the intake and exhaust valves are closed, and the piston is in its lowest position, Bottom Dead Center (BDC). During the compression stroke, the piston moves upward, compressing the fuel-air mixture (ÇENGEL; BOLES, 2013). The cylinder's pressure and temperature rise in this process.

II. Power stroke

   Soon after the piston reaches its highest position – Top Dead Center (TDC) –, the spark plug is activated and the mixture ignites, significantly increasing the pressure and temperature of the system. The high-pressure gases force the piston down, which forces the crankshaft to turn, producing useful work during the expansion stroke. At the end of this time, the piston is in

the lowest position (the completion of the first crankshaft revolution) and the cylinder is filled with combustion products (ÇENGEL; BOLES, 2013).

III. Exhaust stroke

The piston moves upward once more, expelling the exhaust gases through the exhaust valve (ÇENGEL; BOLES, 2013). The exhaust manifold channels the exhaust from individual cylinders into a central exhaust pipe (FERGUSON; KIRKPATRICK, 2016).

IV. Intake stroke

The piston moves once more, this time downwards, allowing the fuel-air mixture to enter through the intake valve, resulting in a homogeneous mixture (ÇENGEL; BOLES, 2013). Typically, the fuel used is gasoline. In this process, generally the exhaust valves are closed (FERGUSON; KIRKPATRICK, 2016).

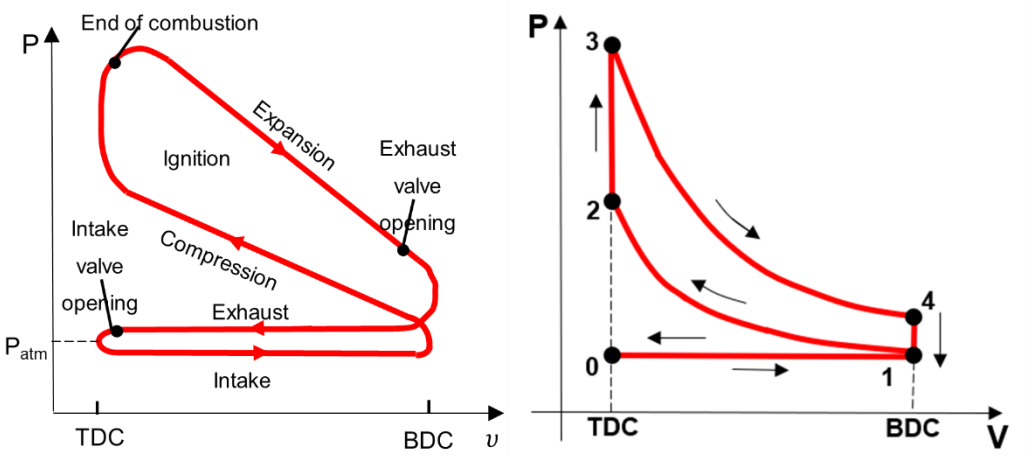

(a) *Real* four-stroke spark ignition engine cycle (b) *Idealized* Otto cycle

Figure 2.7: *Real* and *Idealized* cycles of four-stroke spark ignition engines and their P-υ diagrams. Sources: (ÇENGEL; BOLES, 2013) and (FURLANI; SILVA, 2006), author's own elaboration.

To make a thermodynamic analysis of the real four-stroke cycles previously described is not an easy job. However, the analysis can be much more simply if some standard assumptions are used. The resulting cycle, to maintain very similar characteristics to real operating conditions, is the ideal Otto cycle (ÇENGEL; BOLES, 2013). It is composed by four internally reversible processes:

1 – 2 Isentropic compression process

2 – 3 Isochoric heat supply process

3 – 4 Isentropic expansion process

4 – 1 Isochoric heat rejection process

In addition to these four processes, one more can be added: the reversible isobaric process 0 ↔ 1, in which the fuel-air mixture is admitted (0 → 1) and the combustion gases are exhausted (1 → 0), as showed in Figure 2.7.

The fuel used in a SI engine must have significant volatility to make easy its vaporization, to increase engine acceleration and reach the ideal operating temperature in a shorter time, avoiding the formation of steam bubbles in the supply circuit. Besides, it is necessary the use of a fuel with high temperature auto-ignition to prevent knock. On the other hand, this fuel considerably decreases the engine efficiency. Therefore, gasoline, ethanol and natural gas are usually used as fuel for a spark ignition engine close to stoichiometry (LEITE; PRADELLE; LEAL, 2021).

As advantages, these engines have lower cost; generate high rpm at low torque; pollute less; are light in weight and require less space. On the other hand, SI engines have low efficiency, are not economical at high load, and have higher fuel consumption (HEYWOOD, 1988).

2.2.2. Four-Stroke Compression Ignition Engine (CI)

The Diesel cycle is the ideal cycle for reciprocating compression ignition engines. The compression-ignition engine, first proposed by Rudolph Diesel in the 1890s, is very similar to the SI engine, differing mainly in the method of starting combustion. In SI engines, the fuel-air mixture is compressed up to a temperature below the auto-ignition temperature of the fuel, and the combustion process is started by the spark from a spark plug. In CI engines, the air is strongly compressed up to a temperature above the auto-ignition temperature of the fuel, and combustion is initiated by contact as fuel is injected into this hot and heavily compressed air. So, the spark plug is replaced by a fuel injector in diesel engines (ÇENGEL; BOLES, 2013). This change enables a high engine compression ratio, increasing the cycle's efficiency (LEITE; PRADELLE; LEAL, 2021).

In gasoline engines, a fuel-air mixture is compressed during the compression stroke, and compression ratios are limited by the onset of self-ignition or engine knock. In diesel engines, only air is compressed during the compression stroke, eliminating the possibility of self-ignition. Therefore, diesel engines can be designed to operate at much higher compression ratios, typically between 12 and 24. The fuel injection process of diesel engines starts when the piston approaches

the TDC, lasting the first part of the expansion time. Thus, the combustion process in these engines takes a longer interval. Due to this longer duration, the ideal Diesel cycle combustion process is approximated as an isobaric heat supply process. In fact, this is the only process in which the Otto and Diesel cycles differ. The remaining three processes are the same for both ideal cycles (ÇENGEL; BOLES, 2013). The sequence followed by the CI engine also goes through four processes:

1-2 – Isentropic compression process
2-3 – Isobaric heat addition process
3-4 – Isentropic expansion process
4-1 – Isochoric heat rejection process

The similarity between the two cycles is also apparent in the P-v and T-s diagrams of the Diesel cycle, shown in Figure 2.8.

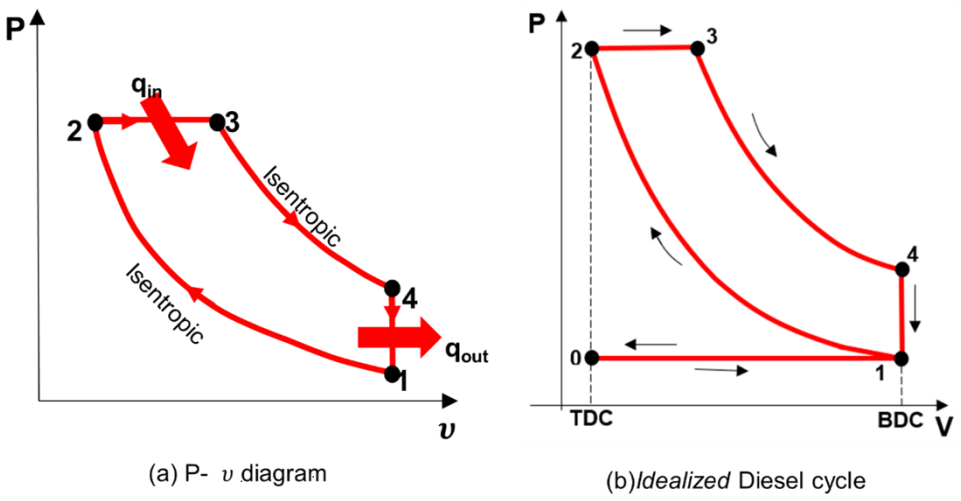

Figure 2.8: T-s and P-v diagrams of *idealized* Diesel cycle. Source: (ÇENGEL; BOLES, 2013), author's own elaboration.

In addition to these four processes, as in previous section, one more process can be added: the reversible isobaric process 0 ↔ 1, in which air is admitted (0 → 1) and the combustion gases are exhausted (1 → 0), as showed in Figure 2.8.

2.2.3. Homogeneous Charge Compression Ignition Engine (HCCI)

Homogeneous Charge Compression Ignition engines are one more of the ICEs technologies available, in which a uniformly blended fuel-air mixture is compressed up to the moment of autoignition. The chemical reaction releases energy, producing work and heat, as expected from the study of the other internal

combustion engines. Despite of that, there's still a question to be concerned about HCCI engines: they have a limited operating range. At high loads and speeds, the rates of heat production and pressure increase lead to engine knock. At low loads, misfire may occur. Hence, several researchers have been studying the various parameters that affect HCCI combustion (CHARALAMBIDES, 2013).

The autoignition combustion process can be described as an oxidation of the fuel managed only by chemical reactions controlled by chain-branching mechanisms. Two temperature regimes exist: one below 850K – low temperature oxidation or cool flame combustion; and another around 1050K – high temperature oxidation or main combustion. Moreover, depending on the fuel composition and the engine conditions, the autoignition process varies significantly. Images of autoignition phenomenon produced by Chemiluminescence and Planar Laser Induced Fluorescence (PLIF) has shown that autoignition would begin equally at several spots all over the combustion chamber, probably due to local inhomogeneities (CHARALAMBIDES, 2013).

The heat released from the burn regions cause the rise of the temperature and pressure in the cylinder. Owing to this, more autoignition points appear, leading to the complete ignition of the whole fuel-air mixture. Whereas there is no need of a spark plug or direct injection near TDC to start the combustion in HCCI engines, lean mixtures can be used allowing a significant economy of fuel. Due to that, the combustion temperature stays at a low level and so NOx emissions diminish considerably compared to SI and CI operation (CHARALAMBIDES, 2013). The comparison of emissions produced by the SI, CI and HCCI engines is shown in Figure 2.9.

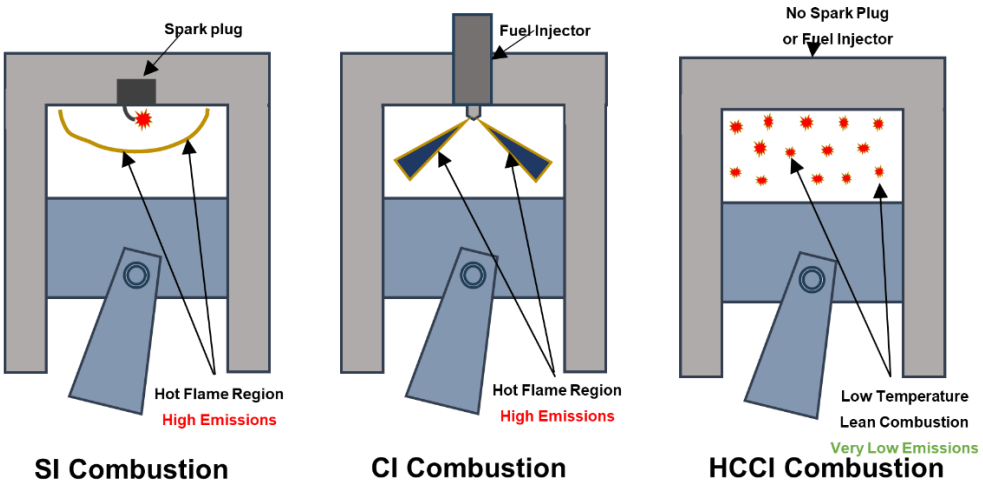

Figure 2.9: Differences between SI, CI and HCCI combustions. Source: (CHARALAMBIDES, 2013), author's own elaboration.

All these constraints mean that HCCI combustion needs to be implemented under harsh operating conditions. At these conditions, HCCI combustion offers Carbon Monoxide (CO) and Hydrocarbon (HC) emissions like SI and CI combustions. Beneath very lean conditions, consequently at low temperatures (around 1500K), incomplete combustion may happen and cause partial oxidation of fuel. This situation leads to lower combustion efficiency, which increase CO and HC emissions. Nevertheless, rich fuel-air mixtures can cause the HCCI engine to knock (CHARALAMBIDES, 2013). Therefore, although HCCI technology is well known in the literature, such facts prevent significant commercial applications. The challenges of using HCCI technology compared to traditional engine technologies (SI and CI engines) are shown in Figure 2.10.

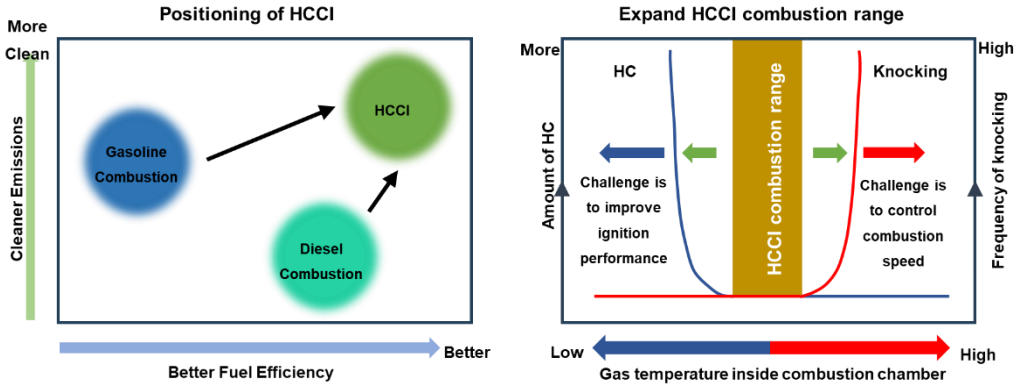

Figure 2.10: Challenges of using HCCI technology compared to traditional engine technologies (SI and IC engines). Source: Nissan Global web page with content related for HCCI, author's own elaboration.

The sequence followed by the HCCI engine also goes through four processes:

I. Compression Stroke:
   Pressure and temperature inside the cylinder rise. Geometry of cylinder and piston are designed to make the fuel-air mixture homogeneous to start the ignition properly.

II. Power Stroke:
   The ignition starts spontaneously. The several spots of autoignition speed up the propagation of combustion. The formation of NOx is controlled, due to the low cylinder peak temperature.

III. Exhaust Stroke:
   The exhaust stroke happens as the other ICEs discussed previously.

IV. Intake Stroke:

As in SI engines, the intake valves admit the lean fuel-air mixture.

2.3. Spark-Assisted Compression Ignition Engine (SACI)

2.3.1.Main concepts on SACI technology

Due to the operating restrictions of the HCCI engine and the great need to improve the functioning of traditional engines (SI and CI engines), a new combustion modality has been studied in the last two decades. From these new researches, the Spark-Assisted Compression Ignition (SACI) engine emerged in the automotive industry as a new kind of internal combustion engine. The SACI technology works alike HCCI engine, but with a promising capability of enhance ignition control robustness, accomplish stable phase control, and enlarge the load range of HCCI engines (CHEN et al., 2020). This technology may also be referred as Spark-Controlled Compression Ignition (SPCCI), Spark-Induced Compression Ignition (SICI), Spark Assisted Homogeneous Charge Compression Ignition (SA-HCCI) and Spark Ignition - Homogeneous Charge Compression Ignition (SI-HCCI).

This technology works as follows: a lean air-fuel mixture is admitted and compressed up to rates applied in CI engines. At this moment, temperature and pressure of the air-fuel mixture increase until the edge of autoignition. To start the ignition at the certain time, a small amount of fuel is directly injected near the spark plug. Right after, the spark plug inflames this part of the mixture. Around the spark, a flame front is created likewise in the SI engine. This one is responsible for diffusing a pressure wave that runs through the combustion chamber. Pressure and temperature are elevated up to the critical point where the main body of fuel combusts (MAZDA UK, 2018). In Figure 2.11, the most important moment of combustion in the SACI engine is shown.

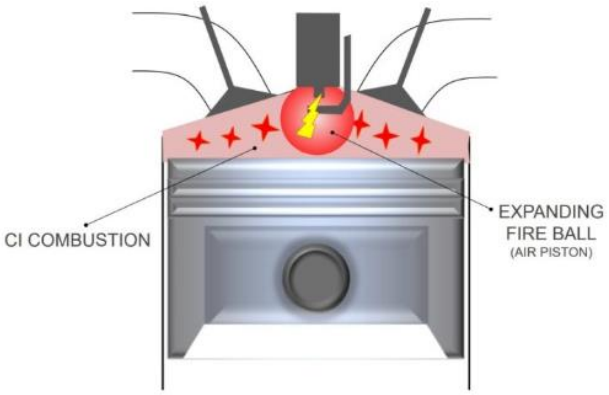

Figure 2.11: Schematic lateral view of the combustion process inside the SACI engine. Source: (MAZDA UK, 2018).

As mentioned previously, HCCI engines actuates between two opposites points of operation, which leads to a narrow range of optimal performance: knock and misfire, that are responsible for decreasing the engine's efficiency. On the other hand, SACI combustion mode is more stable compared to HCCI and achieves higher thermal efficiency compared to SI combustion (CHEN et al., 2020).

Particularities of the traditional engines (SI and CI) and of the HCCI engine put SACI engine in the spotlight to the automotive industry. As seen earlier, SI engines are not able to reach high compression ratios due to the possibility of knocking sooner than the total combustion of the fuel-air mixture. However, to achieve bigger thermal efficiencies, greater compression ratios are necessary. So, the main mentioned technology in this section seeks self-ignition. Then, its success comes from the union of the octane fuel with a high compression ratio, by managing the autoignition timing with the spark.

Pollutant emission and excessive fossil fuel consumption have become major challenges for the NZE in 2050 forcing the automotive industry to response properly (REITZ, 2013). To address these concerns, global researchers have focused more attention on the development of advanced combustion strategies (YAO; ZHENG; LIU, 2009). To an ideal engine work decently, less thermal energy loss and fewer GHG emissions are expected. In this context, as a transition between traditional engines and an electrification future of the engines, SACI technology opts for a very lean mixture (fuel-air equivalence ratio of 0.3-0.5), with the aim of guaranteeing reduction of the engine's temperature, heat loss, and NOx emissions. As a complement to guarantee the improvement of engine operation, a turbocharger is placed before the inlet manifold, making possible the disposition of amounts of air into the cylinder.

The sequence followed by the SACI engine also goes through four processes, as seen in previous engines:

I. Intake Stroke:

The fuel-air mixture enters the cylinder by the intake valves, similarly to SI and HCCI engines. The mixture is very lean, and the turbocharger is responsible for driving the air into the cylinder.

II. Compression Stroke:

The mixture is compressed, raising its temperature and pressure, as in SI, CI, and HCCI engines. With the presence of a fuel injector near the spark plug, stratification of the fuel happens in SACI engines. The injection of fuel nearby the spark plug makes the mixture richer at this place during the compression stroke. It allows the development of a flame front at the surroundings before the autoignition of the unburned gases.

III. Power Stroke:

The electric discharge causes the ignition of the mixture close to the spark plug. This combustion increases the pressure and the temperature throughout the cylinder, which lead to the critical point to the unburned gases self-ignite simultaneously. In Figure 2.12, SACI combustion inside the cylinder is illustrated showing the separation of the spark ignition (SI) flame front from the compression ignition (CI).

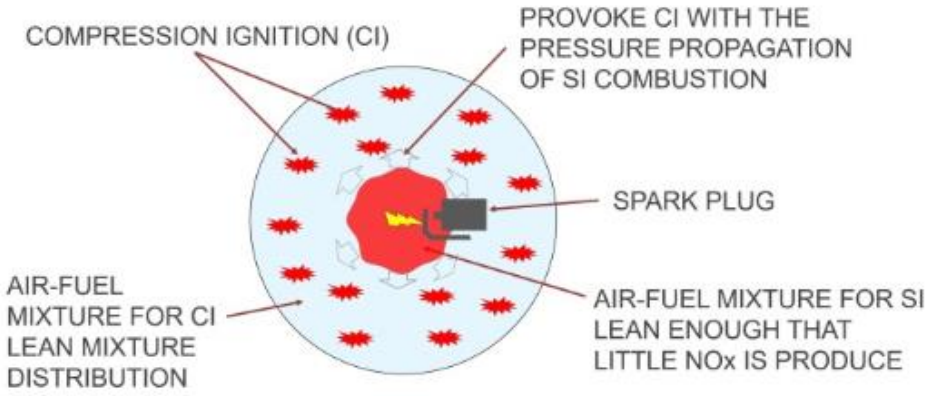

Figure 2.12: Schematic upper view of the combustion process inside the SACI engine. Source: (MAZDA UK, 2018).

IV. Exhaust Stroke:

As in other engines, the piston expels the burned gases through the exhaust valves. While inlet valves are closed, discharge valves are opened.

How SACI technology works as a combination of SI and CI engine technology, a transition point in which the SACI engine changes operation from a SI engine to a HCCI engine can be clearly detected. This transition point is called SOHCCI (Start Of HCCI), as shown in Figure 2.13. Mass fraction burned as a function of the crankshaft angle is presented. It can be seen the variation of Wiebe curve after the autoignition point, exhibiting faster combustion, like an HCCI.

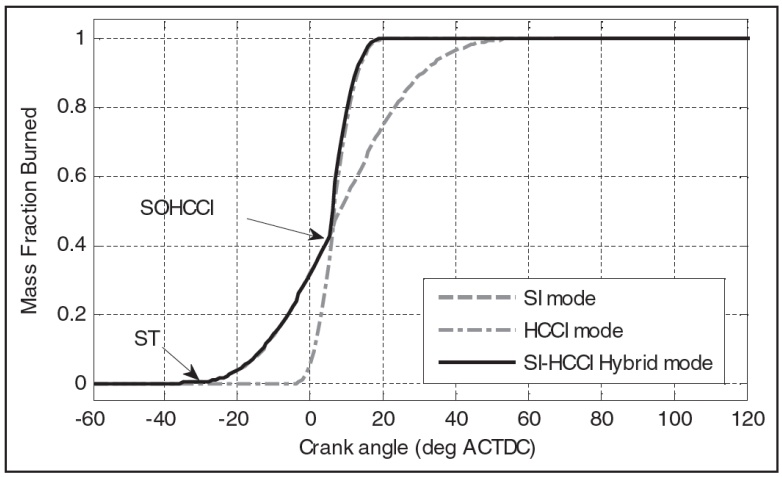

Figure 2.13: Mass fraction burned curve for SI, HCCI and SACI combustion as a function of the crank angle. Source: (YANG; ZHU, 2012).

2.3.2.State-of-the-art on SACI technology

The SACI technology history begins in 2005 with the studies of Wang et al. (WANG et al., 2005) and Urushihara et al. (URUSHIHARA et al., 2005). A combination of high exhaust gas residuals, spark ignition, and two-stage direct fuel injection is proposed as a means of: advancing HCCI combustion phasing, extending HCCI operating range (URUSHIHARA et al., 2005); understanding the effects of spark-ignition and stratified charge in a gasoline fueled HCCI engine, and to obtain better HCCI combustion stability (WANG et al., 2005). In a subsequent study (WANG et al., 2006), the results showed the strategy increased average IMEP (+39%), and decreased emissions of NOx (-64%), HC (-35%), and CO (-6%). At that time, the authors were just thinking about SACI combustion as a possibility of better stabilizing a particular HCCI engine applying a previous SI operation regarding this operation transition.

Bunting, in 2006, studied the effects of different spark timings and fuels in SACI combustion. Results showed that early exhaust valve closing – referred as negative valve overlap (NVO) – strategy allow the mixture's autoignition time to be

better determined. Moreover, higher octane fuels were found to more easily ignite and quickly burn when compared with lower octane fuels (BUNTING, 2006). In 2011, Manofsky et al. also studied the effects of different spark timings and NVO in SACI combustion. Results showed that earlier spark timing resulted in earlier combustion, higher rates of pressure rise, and higher in cylinder pressures and temperatures. Spark advance also resulted in earlier and more rapid heat release (MANOFSKY et al., 2011).

In 2013, Olesky et al. showed that the association of varying simultaneously spark timing and unburned temperature, while maintaining approximately constant the composition, lead to control of burn duration and combustion phasing. Increasing unburned gas temperature and advancing spark, a greater portion of flame-based heat release and a longer 0-90% burn durations were observed. The rise in flame propagation combustion reduced the mass of fuel available for autoignition, shortening the peak of heat release rates, ringing intensity, and combustion stability without implying a reduction of thermal efficiency. The variable mixture, ~24.5% to 29% of internal exhaust gas recirculation (iEGR), associated with the studied NVO range,104 to 130°CA, implicate in a negligible effect over combustion (OLESKY et al., 2013).

In 2013, Yoo et al. studied the effects of initial temperature fluctuations (T'), spark ignition timing (τ_s), turbulence intensity and length scale on self-ignition of a lean homogeneous iso-octane/air mixture at fixed volume and high pressure for HCCI and SACI combustions. About thermal stratification, a higher T' causes greater temporal dispersion of the mean heat release rate (HRR) due to predominance of deflagration mode in combustion at the reaction fronts. Nevertheless, spontaneous ignition prevails for small T', and hence, simultaneous autoignition occurs all over the domain, implying in an excessive rate of pressure rise (YOO et al., 2013).

About spark timing, ignition delay diminishes with the drop of τ_s, while the propagation of HRR is minimal. Heat release occurs by deflagration only before the maximum HRR happens and thereafter occurs by a combination of deflagration and spontaneous ignition through the compression heating of the remaining charge. These results suggest that thermal stratification is necessary for the proper functioning of pure HCCI engines and, furthermore, that spark ignition can be effectively used to control SACI technology ignition timing (YOO et al., 2013).

NVO is a widely used strategy to achieve SACI combustion (GLEWEN et al., 2009; PERSSON et al., 2004, 2005; PERSSON; JOHANSSON; REMÓN, 2007; WAGNER et al., 2006, 2007). In this strategy, part of the hot burned gas is trapped

inside the cylinder by early exhaust valve closing, which benefits the in cylinder thermal state upholding SACI combustion. The use of NVO shows that even for large intervals, which consequently cause larger residual fractions, it is the SI flame that predominates in the HCCI combustion method (PERSSON et al., 2007). As the NVO methodology was initially proposed for HCCI combustion (YANG; ZHAO, 2011), its application to SACI combustion can be used to fill the gap between HCCI and SI operation (CHEN et al., 2011; MANOFSKY et al., 2011). However, SACI combustion using the NVO strategy experiences extra pumping loss and limited intake charge mass outcoming from capture and recompression of the burned gas (XIE et al., 2013a).

Another efficient method to adjust in-cylinder thermal state taking advantage of hot burned residual gas is through a rebreathing way. This method is known as positive valve overlap (PVO). Combustion of HCCI can be successfully carried out by rebreathing exhaust gases, performing better at higher loads (BABAJIMOPOULOS; LAVOIE; ASSANIS, 2003; DUFFOUR et al., 2009). Because this type of rebreathing cannot acquire sufficient hot residual gas, high inlet temperatures and high compression ratios are required to achieve HCCI combustion (YANG; ZHAO; MEGARITIS, 2009).

Compared with HCCI combustion, SACI combustion request less internal residual gas at medium-high load. Research has been conducted to compare SACI combustion performance between the use of NVO and PVO strategies, and it is evidenced that the PVO strategy performs better in fuel economy, whilst the ideal residual fraction can be achieved, resulting in improved efficiency due to optimal combustion phasing, lower pumping loss and lower heat transfer loss (YUN; WERMUTH; NAJT, 2011). SACI combustion can also be achieved using smaller PVO, which is likewise traditional SI valve lift profiles, but the load range is narrow due to the relatively high compression ratio and fixed valve timing (WANG et al., 2010).

In 2013, Xie et al. studied three types of PVO and its influence over SACI combustion: early intake valve opening (EIVO), late exhaust valve closing (LEVC) and early intake valve opening combined with late exhaust valve closing (EIVO&LEVC). The nature of EIVO strategy is exhaust gas backflow through intake ports. The nature of LEVC strategy is exhaust gas rebreathing through exhaust ports. And in EIVO&LEVC strategy, the burned gas is obtained in the cylinder by both exhaust gas back flow through intake ports and exhaust gas re-breathing through exhaust ports (XIE et al., 2013a).

Numerical simulations were carried out initially to evaluate how valve configurations affects the gas exchange process. Thus, its relevance to combustion were investigated and compared experimentally to optimize the engine performance with PVO. Finally, the best fuel consumption strategy for SACI combustion at medium–high load were identified. Within the acceptable combustion stability range, the combination of smaller PVO, higher external EGR (eEGR) and earlier spark timing were recommended to lower fuel consumption and NOx emission, at the same engine load. Compared with traditional SI combustion, fuel economy is uplifted by 5–12%. Compared with SACI combustion employing NVO strategy, the PVO strategy provide up to 9% improvement on fuel consumption with a reduction of 35–70% in NOx emission (XIE et al., 2013a).

In 2024, Li et al. showed both air and exhaust gas dilution methods can reduce NOx and HC emissions. The exhaust gas dilution method showed excellent performance in reducing NOx, with maximum NOx emission improvement rates above 80% for gasoline, 15%/85% methanol/gasoline, 30%/70% methanol/gasoline and 15%/85% ethanol/gasoline. The air dilution method achieved the best results at the same time for fuel consumption and NO emissions, reducing both. Air dilution had a better effect on reducing HC emissions. The addition of methanol and ethanol proved to be beneficial for reducing HC emissions (LI et al., 2024).

The effects of swirl and fuel stratification were studied by Persson, Johansson and Remón. In these studies, they showed that in-cylinder turbulence affects the mixture's autoignition timing and, therefore, SACI combustion as a whole (PERSSON; JOHANSSON; REMÓN, 2007). In 2013, Yoo et al. also studied the effect of turbulence on mixture stratification. In HCCI combustion, to homogenize the mixture a fast turbulence timescale frequently may be applied so the combustion is more apt to happen by spontaneous ignition (YOO et al., 2011). In SACI combustion, turbulence with high velocity fluctuations significantly enhances the overall combustion causing many flame propagations, driving the mixture to a more homogeneous state of combustion during its last phase (YOO et al., 2013).

Keros et al. studied SACI emissions in comparison with those related to SI and HCCI, for a limited range of conditions. In these experiments, HC emissions were slightly sensitive to the engine operation. NOx emissions are shown to be strongly related with spark timing for SACI engines. Furthermore, it is important to observe that both HCCI and SACI combustions could provide low NOx emissions (under 100 ppm) (KEROS et al., 2009).

In 2017, Albayrak Çeper et al. realized a study about the relation of emissions and performance with changing the engine mode (SI, HCCI and SACI engines) and varying engine speed, the excess air ratio (EAR) and wide-open throttle (WOT) (ALBAYRAK ÇEPER et al., 2017). CO emissions formation is related to two main factors, depending on combustion temperature and mixture homogeneousness (YAO; ZHENG; LIU, 2009). When comparing the CO emissions for the combustion modes, the maximum CO emission was obtained at HCCI combustion mode with high speed and EAR = 1.3. And CO emissions for both SACI and HCCI combustions were at a higher level than that of SI combustion. Here, HC emissions are also shown to be weakly sensitive to engine operation. The formation of NOx depends strongly on the combustion temperature. In the case of HCCI combustion, NOx emissions had a quite lower level than those of SI and SACI combustion modes for all EAR values.

NOx emissions presented a quite high level for SACI combustion as in the literature (URUSHIHARA et al., 2005), although these emission values were lower levels than those of SI combustion at both WOT and 50% WOT (ALBAYRAK ÇEPER et al., 2017). Chang et al. presented the difference in emissions among SI, HCCI, and SACI combustion regarding intake air temperature. While SI engines emit around 9.5 g/kWh of NOx, HCCI and SACI engines have on average, an emission of 3.5 g/kWh, i.e., 63% lower (CHANG et al., 2017). Varying the loads, the SACI engine emissions under medium loads (4 bar) were significantly better than those under low loads (2 bar) due to more complete combustion. Lower total HC, CO and PM emissions were achieved at the most efficient direct injection rate, while NOx emissions remained at a low level (ZHAO et al., 2023).

In 2010, Wang et al. analyzed SACI combustion visually. A gasoline engine was modified to enter in HCCI combustion after a first SI flame deflagration and took multiple pictures of the waves. In SI, the authors observed the flame development after the spark ignition. It grew until all the mixture was burned inside the cylinder. In SACI, however, before the flame was completely spread through the whole cylinder, the unburned volume attained the condition of autoignition and self-ignited almost simultaneously (WANG et al., 2010).

Ortiz-Soto et al. study revealed that, while the net thermal efficiency of SI engines varies from 24 to 32% and CI engines from 37 to 43%, at their optimal range, SACI engines present an efficiency of 41 to 43%, indicating a more stable condition than HCCI as a function of the mean effective pressure (MEP) (ORTIZ-SOTO et al., 2019).

This technique has also been the center of multiple sensitivity analysis. Many parameters have been studied, such as the influence of ambient temperature and humidity in the SACI combustion, affirming that higher ambient temperature formats higher NOx (CHANG et al., 2017); the addition of substances into the fuel to stabilize autoignition such as heptane (CHEN et al., 2020); spark timing for better efficiency (MIDDLETON et al., 2015); EGR injection strategy in autoignition control (ZHOU et al., 2018); and the numerical study of the flame front in hydrogen/air blend SACI engines (ZHANG et al., 2017).

A quick search in July 2024 at Portal de Periódicos of Coordenação de Aperfeiçoamento de Pessoal de Nível Superior (CAPES) for related names of SACI engines returned a total of 120 articles, categorized as follows:

- SI-HCCI (2002 – 2021): 40
- SPCCI (2021 – 2024): 2
- SICI (2004 – 2024): 14
- SA-HCCI (2010 – 2023): 5
- SACI (2007 – 2024): 59

Table A.1, in the . Appendices, presents a summary of the studies discussed in this section. This table presents 34 articles, published between 2004 and 2024. From this number of articles, 24 are experimental, 9 are numerical and 1 is experimental and numerical. The fuels that appear in these articles are methane, polyoxymethylene dimethyl ether (PODE), hydrogen, gasoline, n-heptane, isooctane, ethanol, methanol, ethanol + gasoline blends, methanol + gasoline blends, indolene, heptane, indolene + ethanol blend and gasoline + indolene blends. From them, and also from the total of articles found at Periódicos of CAPES, just one article presented a study analyzing the effects of hydrogen as fuel in SACI engines.

2.4. Relevance of the study

With the requirements of the decrease in emissions emitted from internal combustion engine, manufacturers of road vehicles and other machinery powered by these engines are under enormous pressure to reduce the environmental impact of their products. Tank-to-wheels emission of CO_2 can be reduced by increasing engine thermal and mechanical efficiency, while introducing biofuels or electrofuels can help to reduce well-to-tank emissions. Apart from the CO_2 issue, emissions of toxic exhaust compounds, in particular nitrogen oxides (NOx) and

particulate matter (PM), still pose a challenge for contemporary combustion engines (HUNICZ et al., 2020).

The action of catalytic converters, responsible for converting harmful emissions into non-toxic gases, is temperature sensitive. Furthermore, a compensatory relation occurs: it reduces the viscosity of the lubricant at high exhaust temperatures, leading to poor lubrication and rapid wear of parts, while low temperatures can result in increased viscosity of the lubricant, aggravating engine wear and, ultimately, leading to serious mechanical failures such as pulled cylinders and melted tiles. Therefore, it is necessary to keep these indicators within a small variation range to maintain stable engine performance. And it is extremely important to study the sensitivity of these indicators to changes in the fuel-air ratio (YANG et al., 2023).

In the last decade, SACI combustion has been profoundly investigated as an alternative engine to the limited range of operation of HCCI engine. These studies present promising experimental and numeric results for this new type of combustion compared to traditional techniques (LEITE, 2021). So, because of the need of reduction in fossil fuel consumption, the automotive industry is continuously looking for alternatives to spark ignition (SI) and compression ignition (CI) engines (ALBAYRAK ÇEPER et al., 2017). Hydrogen takes place in this context as an option of clean fuel in order to reduce GHG emissions.

The engine performance and emissions can be affected by some of the input conditions, such as fuel composition, engine speed, fuel-air equivalence ratio, intake pressure, and valve overlap. Due to the small number of studies related to the SACI engine and the absence of studies with a view of the impact of hydrogen as a fuel for this type of engine, this work aims to contribute to the academic community with new technical information combining the best efficiency of SACI engines with the renewable energy of hydrogen. The previously cited input conditions will have its effect over engine performance and emissions analyzed in section 5.

3 Mathematical Modeling

The thermodynamics of an internal combustion engine is governed by the engine's geometry, the conservation laws of mass and energy, and the combustion reaction. In this chapter, the two-zone model will be presented, followed by the generically presentation of conservation laws. Then, the auxiliary equations will be presented: the engine's main geometric parameters, physicochemical properties, thermodynamic hypotheses adopted, the chemical equilibrium of the combustion reaction, the intake and exhaust flow, the blowby, the heat transfer, the combustion progress, and the auto-ignition. Finally, the emission calculation will be explained. All this mathematical modelling was first developed by LEITE (2021).

3.1. Two-Zone Model

To better define the chemical species and properties of the mixture, a two-zone combustion model is used (HEYWOOD, 1988). This representation divides the gas mixture into two control volumes: burned and unburned.

In this approach, each part has its own: mass, volume, temperature, chemical species, internal energy, entropy, and enthalpy. However, the in-cylinder pressure is assumed to be the same at both zones.

Therefore, it is possible to formulate:

$$V = V_u + V_b \, [m^3] \tag{3-1}$$

$$V = \frac{V}{m} = x_b v_b + x_u v_u \left[\frac{m^3}{kg}\right] \tag{3-2}$$

where v is the specific volume in $\left[\frac{m^3}{kg}\right]$, and x_b and x_u are the mass fraction of burned and unburned gases, respectively. It is noteworthy that $x_b + x_u = 1$.

To compute the parameters involved in an internal combustion engine's thermodynamic cycle, it is necessary to consider the state changes at every stage, such as intake, compression, power, and exhaust. To simplify the analysis, the

fuel-air mixture and the products of combustion are modeled as ideal gases. An ideal gas has a simplified relation between pressure, temperature, and volume.

$$PV = mrT \tag{3-3}$$

where P is the pressure in kPa, V is volume in m^3, m is the mass of gas in kg, r is the mass-specific gas constant in $kJ/(kg \cdot K)$, and T is the temperature in K. The mass-specific gas constant can be calculated as

$$r = \frac{R_{univ}}{M} \left[\frac{kJ}{kgK}\right] \tag{3-4}$$

where R_{univ} is the universal gas constant ($R_{univ} = 8.314\ kJ/(kmol \cdot K)$) and M is the molar mass of the mixture in $kg/kmol$.

The mass fraction, x_i, of any given species is defined as

$$x_i = \frac{m_i}{m} \tag{3-5}$$

resulting in

$$\sum_{i=1}^{n} x_i = 1 \tag{3-6}$$

And the molar fraction, y_i, of a given species, is

$$y_i = \frac{n_i}{n} \tag{3-7}$$

also resulting in

$$\sum_{i=1}^{n} y_i = 1 \tag{3-8}$$

Assuming the two zones to be ideal gases,

$$Pv_u = r_u T_u \tag{3-9}$$

$$Pv_b = r_b T_b \tag{3-10}$$

where,

$$r_i = \frac{R_{univ}}{MW_i} \tag{3-11}$$

and MW_i is the molecular weight of species i in $kg/kmol$.

Finally, the properties of each zone (specific volume v, specific internal energy u, and specific enthalpy h) are a function of the in-cylinder pressure and its zone temperature.

$$v_u = v_u(P, T_u);\ u_u = u_u(P, T_u);\ h_u = h_u(P, T_u); \tag{3-12}$$

$$v_b = v_b(P, T_b);\ u_b = u_b(P, T_b);\ h_b = h_b(P, T_b); \tag{3-13}$$

These relations will be helpful to simplify the conservation equations and, consequently, calculate the in-cylinder pressure and temperatures at every numerical step.

3.2. Conservation Equations

The engine model is based on the equations for mass, energy, and entropy conservation. The independent variables are the derivatives of pressure and temperatures (burned and unburned) regarding the crank angle. The following subsections show the equations that were integrated into a Matlab routine, software that allows programing and used in latest 2024 version released.

3.2.1. Conservation of Mass

The first conservation law to be studied is the conservation of mass. Equation (3-14) shows the mass rate balance entering the cylinder $\dot{m}_I$ through the valves and leaking through piston rings (blowby mass), where $\dot{m}_{int}$ is the intake mass rate, $\dot{m}_{exh}$ is the exhaust mass rate and $\dot{m}_{bb}$ is the blowby mass rate. Equation (3-15) shows the derivative form of conservation of mass. Differentiating the specific volume, it can be found a helpful form of the conservation of mass. Equation (3-16) is derived from the equality of cylinder volume and the volumes of

the burned and unburned gases. For these equations, the intake and exhaust valves may be open or not.

$$\dot{m}_I = \dot{m}_{int} - \dot{m}_{exh} - \dot{m}_{bb} \tag{3-14}$$

$$\frac{d\rho}{d\theta} = \frac{d}{d\theta}\left(\frac{m}{V}\right) = \frac{d}{d\theta}\left(\frac{1}{x_i v_i}\right), i = u, b; \tag{3-15}$$

$$\frac{d}{d\theta}\left(\frac{V}{m}\right) = \frac{d}{d\theta}(x_b v_b + (1 - x_b)v_u) \tag{3-16}$$

Expanding the differentiation,

$$\frac{1}{m}\frac{dV}{d\theta} - \frac{V}{m^2}\frac{dm}{d\theta} = x_b\frac{dv_b}{d\theta} + v_b\frac{dx_b}{d\theta} + (1 - x_b)\frac{dv_u}{d\theta} - v_u\frac{dx_b}{d\theta} \tag{3-17}$$

Applying the chain rule and rearranging,

$$\begin{aligned}\frac{1}{m}\frac{dV}{d\theta} - \frac{V}{m^2}\frac{dm}{d\theta} = (v_b - v_u)\frac{dx_b}{d\theta} + x_b\left[\frac{dv_b}{dT_b}\frac{dT_b}{d\theta} + \frac{dv_b}{dP}\frac{dP}{d\theta}\right] \\ + (1 - x_b)\left[\frac{dv_u}{dT_u}\frac{dT_u}{d\theta} + \frac{dv_u}{dP}\frac{dP}{d\theta}\right]\end{aligned} \tag{3-18}$$

To simplify resolving the equation, one can put the independent variables in evidence and find the constants that multiply each one of them.

$$A_1\frac{dP}{d\theta} + B_1\frac{dT_u}{d\theta} + C_1\frac{dT_b}{d\theta} = D_1 \tag{3-19}$$

The constant that multiplies the derivative of pressure is

$$A_1 = x_b\frac{dv_b}{dP} + (1 - x_b)\frac{dv_u}{dP} \tag{3-20}$$

The term that multiplies the unburned temperature derivative is

$$B_1 = (1 - x_b)\frac{dv_u}{dT_u} \tag{3-21}$$

The burned temperature derivative expression is

$$C_1 = x_b \frac{dv_b}{dT_b} \tag{3-22}$$

Finally, the independent term is

$$D_1 = \frac{1}{m}\frac{dV}{d\theta} - \frac{V}{m^2}\frac{dm}{d\theta} - \frac{dx_b}{d\theta}(v_b - v_u) \tag{3-23}$$

3.2.2. Conservation of Energy

The differentiation form of the conservation of energy equation is the following:

$$\frac{dU}{d\theta} = \frac{dQ}{d\theta} - P\frac{dV}{d\theta} - \frac{\dot{m}_l h_l}{\omega} \tag{3-24}$$

where U is the internal energy in kJ, Q is the heat transfer in kJ and $\dot{m}_l h_l$ is the liquid energy entering the cylinder in kJ/s, calculated by

$$\dot{m}_l h_l = \dot{m}_{int} h_{int} - \dot{m}_{exh} h_{exh} - \dot{m}_{bb} h_{bb} \tag{3-25}$$

where the subscripts int, exh and bb respectively mean intake, exhaust and blowby. Expanding the internal energy differentiation,

$$\frac{dm}{d\theta}u + m\frac{du}{d\theta} = \frac{dQ}{d\theta} - P\frac{dV}{d\theta} - \frac{\dot{m}_l h_l}{\omega} \tag{3-26}$$

Now, the mass and internal energy can be divided into burned and unburned.

$$\begin{aligned}\frac{dm}{d\theta}[x_b u_b + (1 - x_b)u_u] + m\frac{d}{d\theta}[x_b u_b + (1 - x_b)u_u] \\ = \frac{dQ}{d\theta} - P\frac{dV}{d\theta} - \frac{\dot{m}_l h_l}{\omega}\end{aligned} \tag{3-27}$$

Expanding,

$$\frac{dm}{d\theta}[x_b u_b + (1 - x_b)u_u] + m\left[\frac{dx_b}{d\theta}u_b + x_b\frac{du_b}{d\theta} - \frac{dx_b}{d\theta}u_u + (1 - x_b)\frac{du_u}{d\theta}\right] = \frac{dQ}{d\theta} - P\frac{dV}{d\theta} - \frac{\dot{m}_I h_I}{\omega} \quad (3\text{-}28)$$

Now, it is possible to substitute the specific internal energy derivative.

$$\frac{dm}{d\theta}[x_b u_b + (1 - x_b)u_u] + m\left\{\frac{dx_b}{d\theta}(u_b - u_u) + x_b\left[\left(c_{p,b} - P\frac{dv_b}{dT_b}\right)\frac{dT_b}{d\theta} - \left(T_b\frac{dv_b}{dT_b} + P\frac{dv_b}{dP}\right)\frac{dP}{d\theta}\right] + (1 - x_b)\left[\left(c_{p,u} - P\frac{dv_u}{dT_u}\right)\frac{dT_u}{d\theta} - \left(T_b\frac{dv_u}{dT_u} + P\frac{dv_u}{dP}\right)\frac{dP}{d\theta}\right]\right\} = \frac{dQ}{d\theta} - P\frac{dV}{d\theta} - \frac{\dot{m}_I h_I}{\omega} \quad (3\text{-}29)$$

As done in the conservation of mass equation, it is possible to put in evidence the independent variables.

$$A_2\frac{dP}{d\theta} + B_2\frac{dT_u}{d\theta} + C_2\frac{dT_b}{d\theta} = D_2 \quad (3\text{-}30)$$

The multiplying constants A_2, B_2, C_2, and D_2 are the following:

$$A_2 = -m\left[x_b\left(T_b\frac{dv_b}{dT_b} + P\frac{dv_b}{dP}\right) + (1 - x_b)\left(T_b\frac{dv_u}{dT_u} + P\frac{dv_u}{dP}\right)\right] \quad (3\text{-}31)$$

$$B_2 = m(1 - x_b)\left(c_{p,u} - P\frac{dv_u}{dT_u}\right) \quad (3\text{-}32)$$

$$C_2 = mx_b\left(c_{p,b} - P\frac{dv_b}{dT_b}\right) \quad (3\text{-}33)$$

$$D_2 = \frac{dQ}{d\theta} - P\frac{dV}{d\theta} - \frac{\dot{m}_I h_I}{\omega} - \frac{dm}{d\theta}[x_b u_b + (1 - x_b)u_u] - m\frac{dx_b}{d\theta}(u_b - u_u) \quad (3\text{-}34)$$

3.2.3. Entropy Balance (Unburned Volume)

Since three independent variables (P, T_u, T_b) and two equations (conservation of mass and energy) are already defined, another equation is necessary. Because of its simplicity, the entropy balance on the unburned volume is chosen. Treating it as an open system losing mass via leakage and combustion, it can be showed that

$$\frac{dS_u}{d\theta} = \frac{d}{d\theta}(m_u s_u) = -\frac{1}{T_u}\frac{\dot{Q}_u}{\omega} \quad (3\text{-}35)$$

where $\dot{Q}_u$, described by Newton's relation, is the heat loss in the unburned volume in kW, calculated by

$$\dot{Q}_u = \alpha_u A_u (T_u - T_\omega)\ [kW] \quad (3\text{-}36)$$

and

$$A_u = \left(1 - \sqrt{x_b}\right) A(\theta)\ [m^2] \quad (3\text{-}37)$$

Expanding the derivatives on the left-hand side of the equation,

$$\frac{dm}{d\theta}(1 - x_b)s_u - m\frac{dx_b}{d\theta}s_u + m(1 - x_b)\left[\frac{c_{p,u}}{T_u}\frac{dT_u}{d\theta} - \frac{dv_u}{dT_u}\frac{dP}{d\theta}\right] = -\frac{1}{T_u}\frac{\dot{Q}_u}{\omega} \quad (3\text{-}38)$$

Now, it is possible to obtain the same type of equation as in the conservation of mass and energy.

$$A_3\frac{dP}{d\theta} + B_3\frac{dT_u}{d\theta} + C_3\frac{dT_b}{d\theta} = D_3 \quad (3\text{-}39)$$

The A_3, B_3, C_3, and D_3 constants are:

$$A_3 = -m(1 - x_b)\frac{dv_u}{dT_u} \tag{3-40}$$

$$B_3 = m(1 - x_b)\frac{c_{p,u}}{T_u} \tag{3-41}$$

$$C_3 = 0 \tag{3-42}$$

$$D_3 = -\frac{1}{T_u}\frac{\dot{Q}_u}{\omega} + m\frac{dx_b}{d\theta}s_u - \frac{dm}{d\theta}(1 - x_b)s_u \tag{3-43}$$

3.3. Auxiliary Equations

Next, the auxiliary equations necessary for the complete understanding of the basic equations of the mathematical development applied to the numerical simulator used will be presented.

3.3.1. Engine Geometry

The geometry of an internal combustion engine is fundamental for understanding its thermodynamics. The following parameters, shown in Figure 3.1, are of particular interest: cylinder bore, $B\ (m)$; connecting rod length, $L\ (m)$; crank radius, $R\ (m)$; cylinder stroke, $S\ (m)$; and crank angle, θ (°). One can notice that the crank radius is one-half of the stroke and that when the piston is at the TDC, the crank angle is 0º.

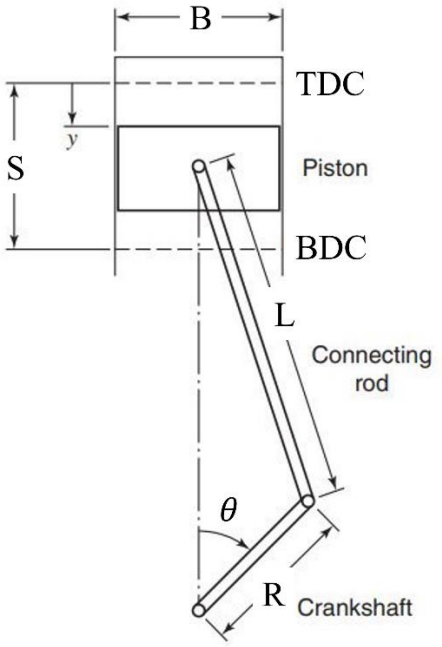

Figure 3.1: Engine schematic geometry (FERGUSON; KIRKPATRICK, 2016).

The first geometric relation of an engine to be presented in this chapter is the compression ratio, r_c, which is the ratio of the maximum and minimum cylinder volume.

$$r_c = \frac{V_{BDC}}{V_{TDC}} \tag{3-44}$$

Another vital parameter is the displacement volume, V_d, the difference between the maximum and minimum volume for a single cylinder.

$$V_d = V_{BDC} - V_{TDC} = \frac{\pi B^2}{4} S \ [m^3] \tag{3-45}$$

It is noteworthy that the total displacement volume, V_d^{tot}, is calculated as the displacement volume for single-cylinder times the number of cylinders in an engine. After defining the compression ratio, one can calculate the Top Dead Center Volume, V_{TDC}, as a function of the bore, the stroke, and the compression ratio.

$$V_{TDC} = \frac{\pi B^2}{4} \frac{S}{(r_c - 1)} \ [m^3] \tag{3-46}$$

The cylinder volume, V, can be written as a function of the crank angle and the geometric parameters cited above.

$$V(\theta) = V_{TDC} \cdot \left[1 + \frac{(r_c - 1)}{2} \cdot \left[1 - \cos(\theta) + \frac{1}{\epsilon} \cdot \left[1 - \sqrt{1 - (\epsilon \cdot \sin(\theta))^2}\right]\right]\right] \tag{3-47}$$

where ϵ is the ratio between the half-stroke and the connecting rod length:

$$\epsilon = \frac{S}{2 \cdot L} = \frac{R}{L} \tag{3-48}$$

Beyond that, the compression ratio is defined as the biggest volume value. The cylinder's lateral area can be calculated with the cylinder volume and the cylinder bore.

$$A(\theta) = V(\theta) \cdot \frac{4}{B} \quad [m^2] \tag{3-49}$$

The engine geometry can be well defined using five parameters: cylinder bore (B), compression ratio (r_c), total displacement volume (V_d^{tot}), number of cylinders (N_{cyl}) and half-stroke to rod ratio (ϵ). Although these five relations are sufficient to describe the engine geometry, it is possible to use another one without losing information. This other one relation is the cylinder stroke (S). Therefore, the description of the geometry admitted was based on six parameters, accepting the existence of redundant variables.

Table 3.1: Engine main geometric parameters

Parameter	Symbol	Unit
Bore	B	mm
Stroke	S	mm
Compression Ratio	r_c	-
Total Displacement Volume	V_d^{tot}	cm^3
Number of Cylinders	N_{cyl}	-
Half-stroke to Rod Ratio	ϵ	-

3.3.2. Thermodynamic Properties

The engine's pressure and temperatures, calculated from the conservative equations, depends on some thermodynamic properties of the gas mixture and its chemical species. These properties (c_p, h, and s) are a function of temperature and were determined by numerous institutions of research. The thermodynamic properties are calculated with data from two researches: NASA (MCBRIDE et al., 1993) and Perry (MALONEY, 2008). Leite et al. (LEITE; PRADELLE; LEAL, 2021) also compared these two thermodynamic properties values with the model used by Ferguson (FERGUSON; KIRKPATRICK, 2016).

NASA model was the one chosen for almost all the species. Its predictions were consistent for the variables such as heat capacity, enthalpy, and entropy at the temperature range needed. It also takes into consideration the effect of intermediate species, as H, O, OH and NO radicals, differently from Perry's model which only presents species at chemical equilibrium (Table B.1). The equations for the necessary thermodynamic properties of NASA model are shown below.

$$c_p(T) = r(a_1 \cdot T^{-2} + a_2 \cdot T^{-1} + a_3 + a_4 \cdot T + a_5 \cdot T^2 + a_6 \cdot T^3 + a_7 \cdot T^4) \quad [-] \tag{3-50}$$

$$h(T) = r\left(-a_1 \cdot T^{-1} + a_2 \cdot \ln(T) + a_3 \cdot T + a_4 \cdot \frac{T^2}{2} + a_5 \cdot \frac{T^3}{3} + a_6 \cdot \frac{T^4}{4} + a_7 \cdot \frac{T^5}{5} + b_1\right) \quad [-] \tag{3-51}$$

$$s(T) = r\left(-a_1 \cdot \frac{T^{-2}}{2} - a_2 \cdot T^{-1} + a_3 \cdot \ln(T) + a_4 \cdot T + a_5 \cdot \frac{T^2}{2} + a_6 \cdot \frac{T^3}{3} + a_7 \cdot \frac{T^4}{4} + b_2\right) \quad [-] \tag{3-52}$$

Perry's model was used to predict the fuel's thermodynamic properties. Through this, the c_p is modeled, and the enthalpy and entropy are calculated using the enthalpy and entropy of formation at the temperature of reference, as can be seen in the following equations. Table B.2 shows this model's constants for methane and hydrogen.

$$c_p(T) = C_1 + C_2\left[\frac{C_3/T}{\sinh(C_3/T)}\right] + C_4\left[\frac{C_5/T}{\cosh(C_5/T)}\right] \quad \left[\frac{kJ}{kmol \cdot K}\right] \tag{3-53}$$

$$h(T) - h(T_{ref}) = \int_{T_{ref}}^{T} c_p dT \quad \left[\frac{kJ}{kmol}\right] \tag{3-54}$$

$$s(T) - s(T_{ref}) = \int_{T_{ref}}^{T} \frac{c_p}{T} dT \quad \left[\frac{kJ}{kmol \cdot K}\right] \tag{3-55}$$

Due to Perry's model present data on a molar basis, specific heat capacity, enthalpy, and entropy will have to be divided by the fuel's molecular weight (kg/kmol). So these properties will be in the format needed in the conservation laws, i.e., kJ/(kg.K), kJ/(kg), and kJ/(kg.K), respectively.

The choice of Perry's model for the fuel's heat capacity were defined by the presence of an aggressive negative slope under 500 K at NASA's model. Ferguson and NASA models showed a monotonical increase of the adimensional heat capacity with temperature. However, the difference in the values of the heat capacity at lower temperatures did not affect the similarity of the enthalpy values in all three models (LEITE; PRADELLE; LEAL, 2021).

The Perry and NASA's unburned gases models are similar. The choice of NASA's model for most of the chemical species was justified by the presence of the radicals such as H, OH, O, and NO that do not appear in the equilibrium state (LEITE; PRADELLE; LEAL, 2021). Table 3.2 presents the Chemical and physical properties for methane and hydrogen.

Table 3.2: Chemical and physical properties for fuels (DI IORIO; SEMENTA; VAGLIECO, 2014).

	Methane	**Hydrogen**
Molecular weight (g/mol)	16.04	2.02
C/H ratio (%)	0.25	0
Density (kg/m^3)	0.67 (gas, 25°C, 1atm)	0.08 (gas, 20°C, 1atm)
Low heating value (MJ/kg)	50	120
Flammability limit (% vol)	5.3/14	4/75
Stoichiometric air/fuel ratio (kg/kg)	17.24	34.20
Max laminar burning velocity in air (m/s)	0.3E0.35	2E4
Net ignition energy (MJ)	0.29	0.02
Quenching distance (mm)	1.9	0.6
Energy density (MJ/l)	35.8	10.3

3.3.3. Maxwell's Relations

Maxwell's relations were used as an instrument for the simplification of the conservation laws equations. The four most common Maxwell relations are the following:

$$\left(\frac{\partial T}{\partial v}\right)_s = -\left(\frac{\partial P}{\partial s}\right)_v \tag{3-56}$$

$$\left(\frac{\partial T}{\partial P}\right)_s = +\left(\frac{\partial v}{\partial s}\right)_P \tag{3-57}$$

$$\left(\frac{\partial s}{\partial v}\right)_T = +\left(\frac{\partial P}{\partial T}\right)_v \tag{3-58}$$

$$\left(\frac{\partial s}{\partial P}\right)_T = -\left(\frac{\partial v}{\partial T}\right)_P \tag{3-59}$$

These equations perform the parity of the second derivatives of each of the four thermodynamic potentials (FERGUSON; KIRKPATRICK, 2016), referring to its thermal variable (temperature T or entropy s) and its mechanical variable (pressure P or volume V).

Maxwell's relations makes possible to quantify entropy changes, which cannot be directly measured. In addition, it facilitates the solution of conservation laws by allowing all thermal and mechanical changes to be transformed into a

single parameter of each nature. In this work, the chosen parameters were pressure and temperature. This is why all changes will ultimately be expressed by pressure or temperature differentiation.

The mixture's specific internal energy can be divided into two specific internal energies (burned and unburned) weighted by its mass fraction.

$$u = u(T,P) = \frac{U}{m} = x_b \cdot u_b + (1 - x_b) \cdot u_u \quad [kJ/kg] \tag{3-60}$$

With equation (3-60), it is possible to employ the chain rule for both zones. So, considering relations (3-12) and (3-13), that highlight the dependence of the internal energy of each zone on in-cylinder pressure and its zone temperature, the chain rule is applied, as seen below.

$$\frac{du_u}{d\theta} = \frac{\partial u_u}{\partial T_u} \cdot \frac{dT_u}{d\theta} + \frac{\partial u_u}{\partial P} \cdot \frac{dP}{d\theta} \tag{3-61}$$

$$\frac{du_b}{d\theta} = \frac{\partial u_b}{\partial T_b} \cdot \frac{dT_b}{d\theta} + \frac{\partial u_b}{\partial P} \cdot \frac{dP}{d\theta} \tag{3-62}$$

To simplify equations (3-61) and (3-62), one of them can be derived in terms of the specific internal energy. Considering pressure and temperature as independent variables and differentiating the definition of enthalpy as a function of temperature, and the fundamental thermodynamic relation as a function of pressure, the following relations are obtained:

$$\frac{\partial h}{\partial T} = \frac{\partial u}{\partial T} + P \cdot \frac{\partial v}{\partial T} \rightarrow \frac{\partial u}{\partial T} = c_p - P \cdot \frac{\partial v}{\partial T} \tag{3-63}$$

$$\frac{\partial u}{\partial P} = T \cdot \frac{\partial s}{\partial P} - P \cdot \frac{\partial}{\partial P} \rightarrow \frac{\partial u}{\partial P} = -T \cdot \frac{\partial v}{\partial T} - P \cdot \frac{\partial v}{\partial P} \tag{3-64}$$

Now, substituting these expressions into equations (3-61) and (3-62):

$$\frac{du_u}{d\theta} = \left(c_{p,u} - P \cdot \frac{\partial v_u}{\partial T_u}\right) \cdot \frac{dT_u}{d\theta} - \left(T_u \cdot \frac{\partial v_u}{\partial T_u} + P \cdot \frac{\partial v_u}{\partial P}\right) \cdot \frac{dP}{d\theta} \tag{3-65}$$

$$\frac{du_b}{d\theta} = \left(c_{p,b} - P \cdot \frac{\partial v_b}{\partial T_b}\right) \cdot \frac{dT_b}{d\theta} - \left(T_b \cdot \frac{\partial v_b}{\partial T_b} + P \cdot \frac{\partial v_b}{\partial P}\right) \cdot \frac{dP}{d\theta} \tag{3-66}$$

Finally, these equations are only in function of the specific volume derivatives, temperature, and pressure.

3.3.4.Combustion Progress

Combustion modeling has an essential purpose in engine simulation. By the prediction of cylinder pressure development and engine performance, combustion progress can be forecasted with a high level of accuracy. The Wiebe function, which represents the fraction of mass burned (MFB) as a function of the crank angle position, is frequently used to present the combustion progress (YILDIZ; ALBAYRAK ÇEPER, 2017).

In 2017, Yildiz et al. (YILDIZ; ALBAYRAK ÇEPER, 2017) analyzed the combustion progress in a predictive zero-dimensional (Zero-D) single zone engine modeling of an SI engine fueled with methane and methane-hydrogen blend. To this end, the authors calculated the parameters of the Wiebe function using the least squares method, fitting the MFB curves calculated from experimental pressure data.

The characteristic of the mass fraction burned curve is an initial low-slope region beginning with spark ignition and the onset of energy release at θ_s, followed by a section of rapid growth and then a more gradual decay. This S-shaped curve can be analytically expressed by an exponential relation (HEYWOOD, 1988), known as a Wiebe function, shown in equation (3-67):

$$x_b(\theta) = 1 - exp\left[-a_W \cdot \left(\frac{\theta - \theta_s}{\theta_d}\right)^{k_W}\right] \quad [-] \tag{3-67}$$

where x_b is the mass fraction burned (fraction of energy released), θ is the crank angle (in rad), θ_s is the start of energy release, θ_d is the duration of energy release, a_W is the Wiebe efficiency factor, and k_W is the Wiebe form factor.

The cumulative energy release curve asymptotically approximates of a value of 1, thus the end of combustion needs to be defined by an arbitrary limit. In the present work, this limit is defined as 99.99% (FERGUSON; KIRKPATRICK, 2016). Regarding the Wiebe constants, in this study a model was developed for each of the SI engine constants based on the constants estimated by the analysis of the combustion progress curves obtained from the experimental data in the works of Yildiz et al. (YILDIZ; ÇEPER, 2017) and Diaz et al. (DIAZ et al., 2019), for SI engine

and a Cooperative Fuel Research Engine (CFR), respectively, both fueled with methane and methane/hydrogen blends.

The models were obtained using the least squares method considering linear, quadratic, and rectangular terms and then only the significant terms were kept. It was considered that the equations do not depend on the engine geometry, load, and rotation, as a simplification. They depend on the percentage of methane present (%CH_4) in the fuel used in simulation, that varies from 0.5 to 1, and on the fuel-air equivalence ratio (ϕ), in a range between 0.8 to 1. Equations (3-68), (3-69) and (3-70) show these models. These three equations presents R^2 of 0.69914, 0.70528 and 0.93322, respectively.

$$a_W = 3.123799 + 2.565978 \cdot \left[\frac{(1 - \%CH_4) - 0.75}{0.25}\right] + 2.585548 \cdot \left[\frac{(1 - \%CH_4) - 0.75}{0.25}\right]^2 \quad (3\text{-}68)$$

$$k_W = 3.542553 - 0.623281 \cdot \left[\frac{(1 - \%CH_4) - 0.75}{0.25}\right] - 0.820541 \cdot \left[\frac{(1 - \%CH_4) - 0.75}{0.25}\right]^2 \quad (3\text{-}69)$$

$$\theta_d = 32.11964 + 14.90724 \cdot \left[\frac{(1 - \%CH_4) - 0.75}{0.25}\right] + 14.96428 \cdot \left[\frac{(1 - \%CH_4) - 0.75}{0.25}\right]^2 - 1.97206 \cdot \left[\frac{\phi - 0.9}{0.1}\right] - 1.92530 \cdot \left[\frac{\phi - 0.9}{0.1}\right]^2 \quad (3\text{-}70)$$

Data from the statistical analysis of models presented in equations (3-68), (3-69) and (3-70) are at . Appendices B (Table B.3, Table B.4, and Table B.5). The Matlab™ simulations with these three last equations were analyzed to the ϕ range of 0.30 to 1 and the percentage of methane from 0.5 to 1. The results numerically fitted to the literature data for percentage of methane to a_W and k_W equations, but to $\phi = 0.3$ the results presented to θ_d were negative. Showing that the extrapolation of ϕ to equation (3-70) did not produce results with physical meaning. Due to that, equations (3-68) and (3-69) were applied to simulations and $\theta_d = 46\ CAD$. For HCCI engine, a_W is the same as for the SI engine, $k_W = 6$, and $\theta_d = 11\ CAD$ (LEITE, 2021). In addition, even though combustion efficiency cannot be

considered 100%, its effect was not considered for the calculus in this work. Figure 3.2 plots the cumulative mass fraction burned x_b versus the crank angle for the base case analyzed. In this case, θ_s = −20 °aTDC.

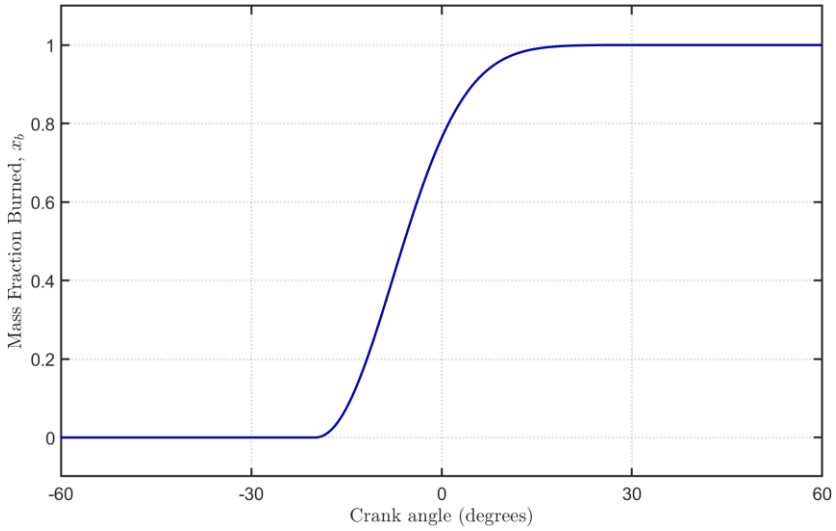

Figure 3.2: Mass fraction burned versus crank angle for the base case (25/75% H_2+CH_4 blend, SI engine).

3.3.5.Intake and Exhaust Flow

The most significant airflow restriction in an internal combustion engine is the flow through the intake and exhaust valves (FERGUSON; KIRKPATRICK, 2016). Therefore, to predict the in-cylinder mass it is necessary to have a good valve model and then, consequently, the engine's performance parameters are obtained.

Yin, in 2017, did extensive work on four-stroke ICEs valve modeling (YIN, 2017). In the present thesis, his results were used to create a simple and robust valve model. Equation (3-71) shows the valve lift motion L_V as a function of the crank angle.

$$L_V = L_{V_{max}} \cdot \sin\left[\pi \cdot \frac{(\theta - \theta_{VO})}{(\theta_{VC} - \theta_{VO})}\right] \quad [m] \tag{3-71}$$

where $L_{V_{max}}$ is the maximum valve lift in m, and θ_{VO} and θ_{VC} are the opening and closing's valve crank angle. Figure 3.3, from the base case analyzed, illustrates the valve lift model in the Matlab routine. In this engine geometry, the exhaust valve lifts slightly higher than the intake valve (Table 3.3).

Table 3.3: Base case valve lift parameters

Parameter	Value	Unit
IVO	-360	CAD
IVC	-135	CAD
EVO	+145 ± 10	CAD
EVC	+360 ± 10	CAD
$L_{V_{max}}^{IV}$	8.75	mm
$L_{V_{max}}^{EV}$	8.80	mm

In this work, to evaluate valve superposition, the negative valve overlap (NVO) and positive valve overlap (PVO) methodologies were used. It was applied as follows: the opening and closing positions of the intake valves (IVO and IVC, respectively) were kept unchanged in all simulations; the opening and closing position of the exhaust valves (EVO and EVC, respectively) were varied simultaneously by -10 CAD or +10 CAD.

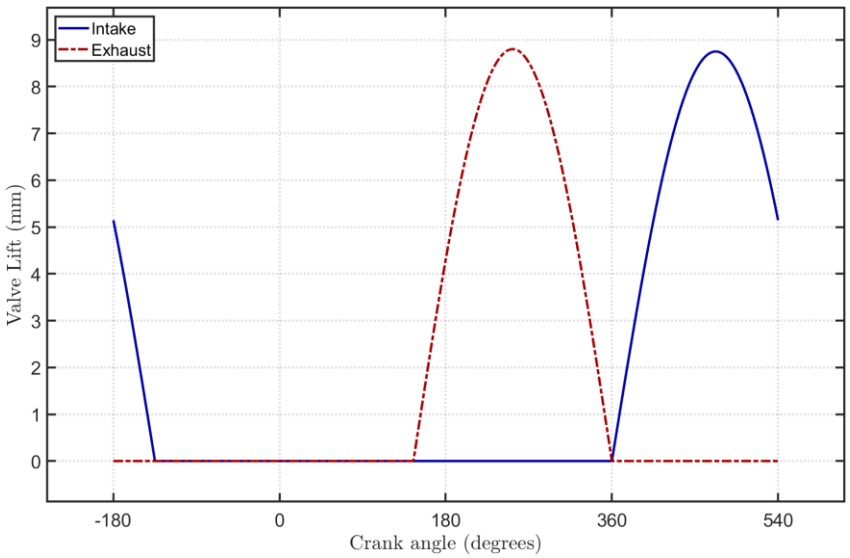

Figure 3.3: Matlab routine valve lift model for the base case (25/75% H_2+CH_4 blend, SI engine).

Equation (3-72) presents the valve's seat area.

$$A_V = \frac{\pi \cdot D_V^2}{4} \quad [m^2] \tag{3-72}$$

where D_V is the valve seat diameter in m. However, not all the seat area is used in the mass flow. Equation (3-73) shows the effective valve area.

$$A_f = C_f \cdot A_V \quad [m^2] \tag{3-73}$$

where $C_f$is the flow coefficient. In the present work, the flow coefficient is modeled by the equation (3-74) (YIN, 2017).

$$C_f = -0.001 + 3.5477 \cdot \left(\frac{L_V}{D_V}\right) - 6.566 \cdot \left(\frac{L_V}{D_V}\right)^2 \quad [-] \tag{3-74}$$

Considering the hypothesis that the flow through the valves is a one-dimensional quasi-steady compressible flow, the desired mass relation can be obtained.

$$\dot{m} = \rho_{up} \cdot A_f \cdot c_{up} \cdot \left[\frac{2}{\gamma - 1} \cdot \left(\left(\frac{P_{down}}{P_{up}}\right)^{\frac{2}{\gamma}} - \left(\frac{P_{down}}{P_{up}}\right)^{\frac{\gamma+1}{\gamma}}\right)\right]^{\frac{1}{2}} \quad \left[\frac{kg}{s}\right] \tag{3-75}$$

where $\dot{m}$ is the mass flow in kg/s, γ is the heat capacity ratio, ρ_{up} is the upstream gas density, c_{up} is the upstream gas sound speed ($c = \sqrt{\gamma \cdot R_{univ} \cdot T}$), and P_{up} and P_{down} are the valve's upstream and downstream pressure. For the intake valve, the upstream conditions are collected at the intake manifold, and the downstream, are at the cylinder. For the exhaust valve, however, the upstream is at the cylinder, and the downstream is at the exhaust manifold.

3.3.6.Blowby

The piston has two types of rings: compression rings, to seal the combustion chamber, and oil control rings, to control the supply of oil to the cylinder wall, to lubricate itself and the piston skirt (LEITE; PRADELLE; LEAL, 2021). Once the cylinder rings do not provide a complete seal of the combustion chamber, combustion gases leak or pass through them. The blowby may affect the engine's indicated performance, friction and wear, and hydrocarbon emissions. Blowby mass flow (3-76) is assumed to pass through the combustion chamber rings at a

rate proportional to the mass of the cylinder contents (FERGUSON; KIRKPATRICK, 2016).

$$\dot{m_{bb}} = C \cdot m \quad [kg/s] \tag{3-76}$$

where C is the blowby coefficient in s^{-1}.

New engines typically have an initial life of 0.5% blowby, then operate for most of their days at a level of 1% blowby, and gradually reach a maximum blowby of 2.5–3.0% at the end of its useful life (FERGUSON; KIRKPATRICK, 2016). In this work, the blowby was assumed to be of 0.8%.

For a complete analysis of the combustion process, it is necessary to specify the enthalpy of mass loss due to blowby, h_{bb} (kJ/kg). At the beginning of the combustion process, unburned gas leaks through the rings. Later in the combustion process, the burned gas leaks through the rings. As a larger portion of the burned gas leaks more than the unburned mass fraction, the equation (3-77) was assumed based on the analysis of Ferguson (2016) and Kirkpatrick.

$$h_{bb} = x_b^2 \cdot h_b + \left(1 - x_b^2\right) \cdot h_u \quad [kJ/kg] \tag{3-77}$$

3.3.7. Heat Transfer

Lounici et al. (2011) and Dabbaghi et al. (2021) studied the most weel-known heat transfer correlations and compared with results obtained in experiment, respectively with a SI engine fueled with methane and a toroidal engine with a crank-rocker mechanism fueled with gasoline.

Heat transfer within internal combustion engines has both convective and radiative nature (DABBAGHI et al., 2021; LOUNICI et al., 2011). In SI engines, the amount of radiation can be approximated to around 20%. Even though it is significantly smaller than the in-cylinder heat loss, it is often considered to the correlation of convective heat transfer (CUDDIHY, 2014; KLEIN; ERIKSSON, 2004). On the other hand, the heat transfer in CI engines suffer a great influence from radiation, reaching a maximum of about 40% (HEYWOOD, 1988), showing an explicit need of consideration in this case (ANNAND, 1963).

In order to estimate the heat losses through engine walls during a cycle, the heat transfer coefficient become the main parameter to be determined. The gas-to-wall heat transfer processes in SI and CI engines have been investigated over the years, providing a wealth literature in this subject. Due to that, correlations have

been proposed for calculating the instantaneous heat transfer coefficient (α) (ANNAND, 1963; CHANG et al., 2004; EICHELBERG, 1939; HOHENBERG, 1979; SITKEI; RAMANAIAH, 1972; WOSCHNI, 1967). In this work, four heat transfer correlations were analyzed: Eichelberg, Woschni, Sitkei and Hohenberg correlations. Those correlations can be splitted into two categories, related to the hypothesis for the heat transfer origin, by means of natural or forced convection.

Back in 1939, Eichelberg proposed a heat transfer correlation based on the dimensionless Nusselt's Correlation, that assumed natural convection. Eichelberg adjusted Nusselt's correlation using experimental test results performed on internal combustion engines. However, years after Woschni showed these formulas were only very approximate, leading to the use of a dimensional analysis considering forced convection. Even though, Eichelberg's correlation still provides a well estimate for heat transfer calculation. Equation (3-78) presents it.

$$\alpha_{Eich} = 7.67 \cdot 10^{-3} \cdot Up^{1/3} \cdot (P \cdot T)^{1/2} \quad [W/(m^2 \cdot K)] \tag{3-78}$$

The Woschni's correlation uses a varying characteristic gas velocity to regard the increase in gas velocity induced by combustion. Equation (3-79) presents this correlation.

$$Nu = 0.035 \cdot Re^{0.8} \quad [-] \tag{3-79}$$

where Nu is the Nusselt number of the gas, and Re is the Reynolds number for the fluid flow, calculated by equation (3-80).

$$Re = \frac{\rho_f \cdot S_f \cdot L_c}{\mu_f} \tag{3-80}$$

where ρ_f is the fluid's density in kg/m^3, S_f is the characteristic fluid velocity in m/s, L_c is the characteristic length in m, and μ_f is the fluid's dynamic viscosity in $Pa.s$.

The characteristic gas velocity in the Woschni's correlation is proportional to the average piston velocity during intake, compression, and exhaust strokes. During combustion and expansion, when the valves are closed, it was assumed that gas velocities are higher due to the combustion process. Equation (3-81) models the average speed of the gas in the cylinder, in m/s.

$$w = C_1 \cdot \overline{S_p} + C_2 \cdot T_{IVC} \cdot \frac{V_d}{V_{IVC}} \cdot \frac{P - P_m}{P_{IVC}} \quad [m/s] \tag{3-81}$$

where $\overline{S_p}$ is the mean piston speed (m/s), T_{IVC} is the temperature at the closing of the intake valve (K), V_{IVC} is the volume of the cylinder at the closing of the intake valve (m^3), P_{IVC} is the pressure at closing of the intake valve (kPa), P_m is the motorized pressure (kPa) and C_1 and C_2 are the Woschni's constants. They are presented in Table 3.4 for each cycle phase (HEYWOOD, 1988). Lastly, it is possible to calculate the Woschni's heat transfer correlation by equation (3-82).

$$\alpha_{Wos} = 3.26 \cdot B^{-0.2} \cdot P^{0.8} \cdot T^{-0.55} \cdot w^{0.8} \quad [W/(m^2 \cdot K)] \tag{3-82}$$

Table 3.4: Woschni constants (HEYWOOD, 1988)

	C_1	**C_2**
Gas exchange period	6.18	0
Compression period	2.28	0
Combustion and expansion period	2.28	3.24E-3

Hohenberg mentioned in his work that Woschni's correlation has some shortcomings in accuracy, which are underestimate heat transfer coefficient in the compression process and overestimate it in the combustion process leading to a cycle with exaggerated average heat flux (HOHENBERG, 1979). Hohenberg came up with another correlation, which is shown below.

$$\alpha_{Hoh} = 130 \cdot {V_d}^{-0.06} \cdot P^{0.8} \cdot {T_{avg}}^{-0.4} \cdot \left(1.4 + \overline{S_p}\right)^{0.8} \quad [W/(m^2 \cdot K)] \tag{3-83}$$

where P is in bar and T_{avg} is the average temperature in K.

Sitkei's correlation is consistent with Woschni's and Hohenberg's correlations. It was developed based on diesel experimental data (SITKEI; RAMANAIAH, 1972) and is shown in equation (3-84).

$$\alpha_{Sit} = 2.36 \cdot 10^{-4}(1 + b) \cdot \frac{\left(P \cdot \overline{S_p}\right)^{0.7} \cdot A^{0.3}}{T^{0.2} \cdot (4 \cdot V)^{0.3}} \quad [W/(m^2 \cdot K)] \tag{3-84}$$

where the value b was found to some types of combustion chambers – direct combustion chamber: $b = 0 - 0.03$; piston chamber: $b = 0.05 - 0.1$; swirl chamber: $b = 0.15 - 0.25$; and pre-combustion chamber: $b = 0.25 - 0.35$ (DABBAGHI et al., 2021). In this work, the value b was considered to piston chamber configuration.

Both the burned and unburned volume have their own heat transfer coefficient. For this purpose, equation (3-85) shows how to obtain the average heat transfer coefficient.

$$\alpha = \sqrt{x_b} \cdot \alpha_b(P, T_b) + \left(1 - \sqrt{x_b}\right) \cdot \alpha_u(P, T_u) \quad [kW/(m^2 \cdot K)] \tag{3-85}$$

Lounici et al. (2011) showed that Woschni's correlation overestimates heat transfer during combustion and underestimates it during compression; Sitkei's correlation severely underestimates heat transfer during the entire cycle, overestimating cycle performance; Hohenberg produced closest results to study experimental data; and Eichelberg predicted results were also close to the study experimental data. Figure 3.4 and Figure 3.5 show the results used for Lounici et al. (2011) conclusions.

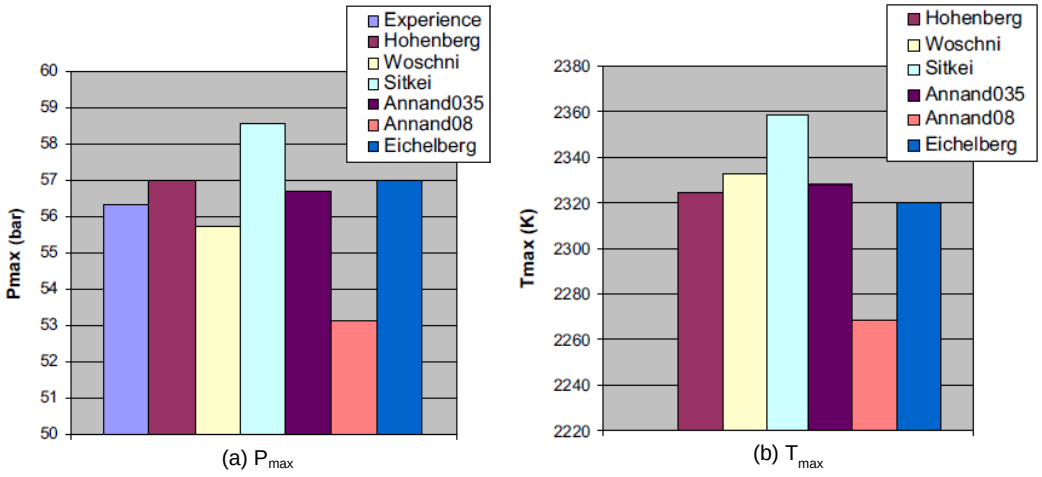

Figure 3.4: Maximum pressure and maximum temperature comparison in relation to heat transfer correlation variation and study experimental data. Source: (LOUNICI et al., 2011).

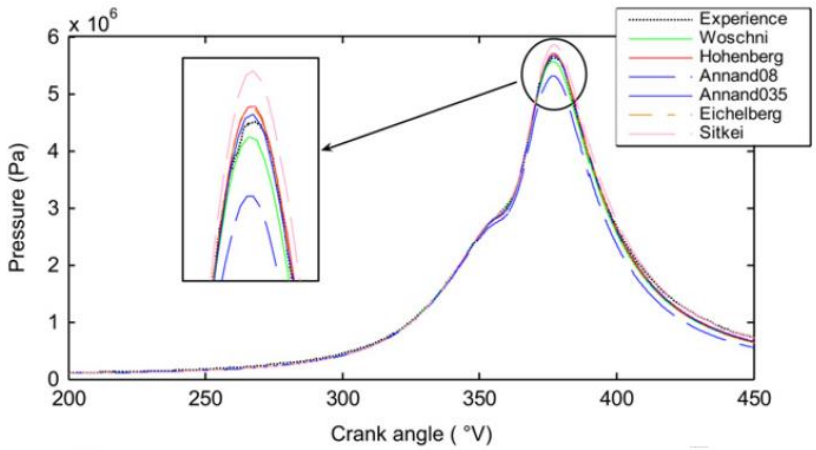

Figure 3.5: Pressure rise along the cycle in relation to heat transfer correlation variation and study experimental data. Source: (LOUNICI et al., 2011).

For the present work, Figure 3.6 shows the average instantaneous cylinder heat transfer coefficients plotted along the crank angle for the base case analyzed to SI engine. Heat transfer presents higher values in the power stroke, when the crank angle is closer to TDC. It is noticeable that due to the change in Woschni constants in each phase, the heat transfer coefficient presents a non-continuous behavior differing in this matter from the others. Due to Lounici et al. (2011) results, Hohenberg correlation was used as reference in the results in the present work. About Annand correlation, it was not implemented for the analysis in this study.

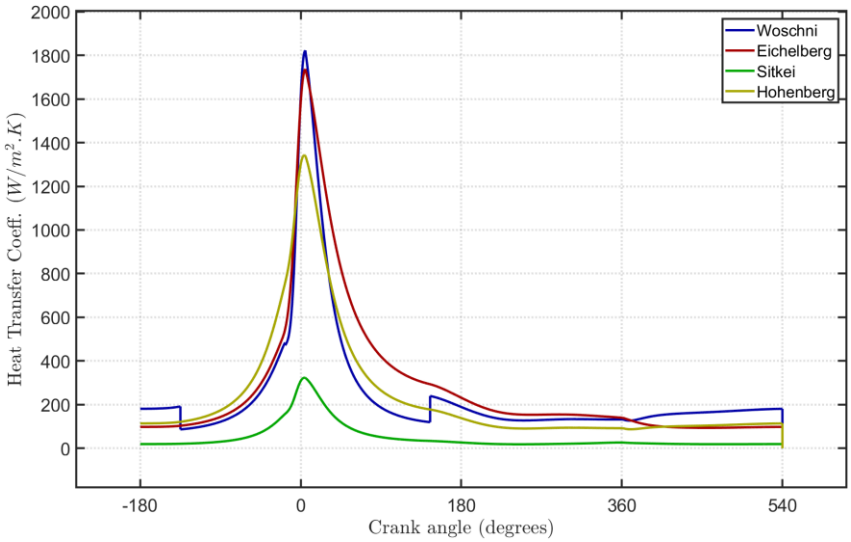

Figure 3.6: Instantaneous Cylinder Average Heat Transfer Coefficient for base case (25/75% H_2+CH_4 blend, SI engine). Souce: MATLAB™ routine.

3.3.8. Burned Mass Initial Temperature

When the chemical reaction begins, it is necessary to define the temperature of the first burned mass. A common approach is to define the temperature of the first mass burned as the adiabatic temperature of the flame. It is defined as the temperature of the combustion products when completely burned without shaft work (W = 0) or heat transfer (Q = 0) to the surroundings (LEITE, 2021).

Assuming the hypothesis of constant pressure combustion, the first law of thermodynamics with no work neither heat transfer to the surroundings presents itself as

$$H_p = H_r \tag{3-86}$$

where H_p is the enthalpy of the product gases in kJ and H_r is the enthalpy of the reactant gases, also in kJ. Whereas the product temperature is generally unknown in first-law combustion calculations, iteration from an initial temperature estimate is necessary to determine the enthalpy of the product mixture. From equation (3-83), the adiabatic temperature of the flame can be found.

3.3.9. Autoignition

According to current scientific literature, two different approaches can be followed for predicting autoignition in thermodynamic simulations: the detailed chemical kinetics and autoignition delay approaches. The first considers the basic steps of the reactions that occur during combustion. However, due to the large volume of reactions to be considered, this model requires a large computational effort, in addition to being difficult to implement. The autoignition delay approach instead relies on unburned gas pressure and temperature history. Although this second approach is less accurate than the first, it is significantly easier to implement in zero-dimensional simulations. For this reason, this approach is often chosen to determine an estimate of the auto-ignition time of air-fuel mixtures (PIPITONE; BECCARI, 2019).

To model knock, it can be assumed that there is a critical mass fraction of combustion precursors, which if reached anywhere within the unburned gas causes autoignition. Typically, knock will occur before the end of normal flame front propagation if the integrated rate of precursor formation is equal to this critical mass

fraction (LEITE, 2021). Equation (3-78) defines the proportion of precursor reaction.

$$\zeta = \frac{x_p}{x_c} \quad [-] \tag{3-87}$$

where x_p is the precursor mass fraction and x_c is the critical mass fraction to auto-ignition. Normalizing the rate of formation of precursors for a better representation is shown by the equation (3-88).

$$\frac{d\zeta}{dt} = \frac{1}{x_c} \cdot \frac{dx_p}{dt} = \frac{1}{\tau} \quad [s^{-1}] \tag{3-88}$$

where τ is the auto-ignition delay time in s. This property is commonly modeled based on Arrhenius type equations. Equation (3-89) shows its definition.

$$\tau = a_{AI} \cdot P^{-n_{AI}} \cdot exp\left[\frac{E_{a_{AI}}}{RT}\right] = a_{AI} \cdot P^{-n_{AI}} \cdot exp\left[\frac{b_{AI}}{T}\right] \quad [s] \tag{3-89}$$

where, P (bar) and T (K) are the pressure and temperature of the air-fuel mixture inside the engine cylinder a_{AI}, and n_{AI} are auto-ignition constants, and $E_{a_{AI}}$ (kJ/kmol) and b_{AI} (K) are auto-ignition activation energy constants.

PIPITONE; BECCARI, (2019) did multiple experiments with methane and approximated the auto-ignition constants as the following: $a_{AI} = 0.0056$, $b_{AI} = 11875$, and $n_{AI} = 3.25$. This model is the Knock-Integral mechanism that is used in this work. Knowing the auto-ignition constants, the knock-integral can be calculated.

$$KI(t) = \zeta(t) = \int_{t_{IVC}}^{t} \frac{d\zeta}{dt} dt = \int_{t_{IVC}}^{t} \frac{1}{\tau} dt \quad [-] \tag{3-90}$$

According to this approach, the knock integral reaches the value of 1 when auto-ignition occurs (i.e., when the radical species in the unburned gas reach the critical concentration), therefore:

$$KI(t_{AI}) = \int_{t_{IVC}}^{t_{AI}} \frac{1}{\tau} dt = 1 \quad [-] \tag{3-91}$$

Applying both equations (3-89) and (3-91), it is possible to specify the time at which knock occurs (t_{KO}). Furthermore, the Knock-Integral and the extent of the precursor reaction can be obtained as a function of crank angle, rather than time, as seen in equation (3-92).

$$\zeta = \frac{1}{\dot{\theta}} \int_{\theta_{IVC}}^{\theta} \frac{d\zeta}{dt} d\theta \tag{3-92}$$

3.3.10. SACI Technique

To model the SACI combustion technique, combustion is divided into two zones: SI and HCCI. The engine starts in SI mode. In this mode, the flame front propagates in the cylinder volume represented by the Wiebe function (with Wiebe constants related to SI combustion). The routine then recalculates the extent of the precursor reaction (Knock-integral) at each crank angle step. If the Knock-Integral reaches one before the end of combustion, the remaining unburned mass burns at a HCCI combustion rate (with Wiebe constants related to HCCI combustion). Equation (3-93) performs this scheme.

$$x_b = \begin{cases} 1 - exp\left[-a_W^{SI} \cdot \left(\dfrac{\theta - \theta_s^{SI}}{\theta_d^{SI}}\right)^{k_W^{SI}}\right], if\ \zeta < 1 \\ 1 - exp\left[-a_W^{HCCI} \cdot \left(\dfrac{\theta - \theta_s^{*}}{\theta_d^{HCCI}}\right)^{k_W^{HCCI}}\right], if\ \zeta = 1 \end{cases} \tag{3-93}$$

where,

$$\theta_s^* = \theta_{SOHCCI} - \theta_d^{HCCI} \cdot \left(\frac{\theta_{SOHCCI} - \theta_s^{SI}}{\theta_d^{SI}}\right)^{\frac{k_W^{SI}}{k_W^{HCCI}}} \tag{3-94}$$

and,

$$\zeta(\theta_{SOHCCI}) = 1 \tag{3-95}$$

3.3.11. Chemical Equilibrium

In this work, the chemical combustion reaction is based on an equilibrium constant method (OLIKARA; BORMAN, 1975). By using equilibrium constants to solve chemical reactions, the algebra performed is less complex than the Lagrange multiplier approach (minimization of Gibbs free energy), considering that the species list is restricted. Treating as important only the radicals O, H, OH, and NO from dissociation as product species, only ten product species are evaluated in this analysis. Equation (3-96) shows the chemical reaction per mole of fuel.

$$\begin{aligned} C_a H_b O_c N_d + \frac{a_s}{\phi}(O_2 + 3.76N_2) \\ \longrightarrow n_1 CO_2 + n_2 H_2O + n_3 N_2 + n_4 O_2 + n_5 CO \\ + n_6 H_2 + n_7 H + n_8 O + n_9 OH + n_{10} NO \end{aligned} \tag{3-96}$$

The fuel is initially mixed with air with an equivalence ratio ϕ, temperature T_u and pressure P. After combustion, the reaction products are in equilibrium at temperature T_b and pressure P. From this overview, the composition and properties thermodynamics of the product mixture can be determined by atom balancing (equation (3-97)).

$$\begin{cases} C: a = (y_1 + y_5) \cdot n \\ H: b = (2y_2 + 2y_6 + y_7 + y_9) \cdot n \\ O: c + 2\dfrac{a_s}{\phi} = (2y_1 + y_2 + 2y_4 + y_5 + y_8 + y_9 + y_{10}) \cdot n \\ N: d + 7.52\dfrac{a_s}{\phi} = (2y_3 + y_{10}) \cdot n \end{cases} \tag{3-97}$$

where n is the amount of substance in the gaseous phase. From equation (3-97), three constants can be defined:

$$\begin{cases} d_1 = \dfrac{b}{a} \\ d_2 = \dfrac{c}{a} + 2\dfrac{a_s}{\phi} \\ d_3 = \dfrac{b}{a} + 7.52\dfrac{a_s}{\phi} \end{cases} \tag{3-98}$$

After substitution into the atom balance equations, and with some rearrangement, the following system is obtained:

$$\begin{cases} 2y_2 + 2y_6 + y_7 + y_9 + d_1 y_1 - d_1 y_5 = 0 \\ 2y_1 + y_2 + 2y_4 + y_5 + y_8 + y_9 + y_{10} - d_2 y_1 - d_2 y_5 = 0 \\ 2y_3 + y_{10} - d_3 y_1 - d_3 y_5 = 0 \\ \sum_{i=1}^{10} y_i = 1 \end{cases} \quad (3\text{-}99)$$

From the system presented in equation (3-99), there are ten variables and only four equations. These remaining equations come from six gas-phase equilibrium reactions. These reactions include the dissociation of hydrogen, oxygen, water, and carbon dioxide, and the formation of OH and NO radicals, as seen below.

$$\begin{cases} \frac{1}{2}H_2 \rightleftharpoons H \quad K_1 = \frac{y_7 P^{1/2}}{y_6^{1/2}} \\ \frac{1}{2}O_2 \rightleftharpoons O \quad K_2 = \frac{y_8 P^{1/2}}{y_4^{1/2}} \\ \frac{1}{2}H_2 + \frac{1}{2}O_2 \rightleftharpoons OH \quad K_3 = \frac{y_9}{y_4^{1/2} y_6^{1/2}} \\ \frac{1}{2}O_2 + \frac{1}{2}N_2 \rightleftharpoons NO \quad K_4 = \frac{y_{10}}{y_4^{1/2} y_3^{1/2}} \\ H_2 + \frac{1}{2}O_2 \rightleftharpoons H_2O \quad K_5 = \frac{y_2}{y_4^{1/2} y_6 P^{1/2}} \\ CO + \frac{1}{2}O_2 \rightleftharpoons CO_2 \quad K_6 = \frac{y_1}{y_4^{1/2} y_5 P^{1/2}} \end{cases} \quad (3\text{-}100)$$

The unit of pressure in the above six equations is in units of atmospheres (atm). Olikara and Borman (OLIKARA; BORMAN, 1975) have curve fitted the equilibrium constants ($K_i(T)$) to JANAF Table data for the temperature range 600 < T < 4000 K:

$$\log_{10} K_i(T) = A_i \cdot \ln(T/1000) + \frac{B_i}{T} + C_i + D_i \cdot T + E_i \cdot T^2 \quad (3\text{-}101)$$

where T is in Kelvin.

The equilibrium constant $K_i(T)$ curve-fit coefficients are listed in Table 3.5. Knowing the mixture mole fraction composition, the steps necessary to compute the thermodynamic properties of interest: specific heat, enthalpy, entropy, specific volume, and internal energy for the given conditions. Figure 3.7 and Figure 3.8

show the result from the enhanced Matlab routine for the in-cylinder chemical species. It is clear the influence of intake, combustion, and exhaust strokes on the species.

Table 3.5: Equilibrium constant K_i curve-fit coefficients

K_i	A_i	B_i	C_i	D_i	E_i
K_1	+0.432E+00	−0.112E+05	+0.267E+01	−0.745E−04	+0.242E−08
K_2	+0.310E+00	−0.129E+05	+0.321E+01	−0.738E−04	+0.344E−08
K_3	−0.141E+00	−0.213E+04	+0.853E+00	+0.355E−04	−0.310E−08
K_4	+0.150E−01	−0.470E+04	+0.646E+00	+0.272E−05	−0.154E−08
K_5	−0.752E+00	+0.124E+05	−0.260E+01	+0.259E−03	−0.162E−07
K_6	−0.415E−02	+0.148E+05	−0.475E+01	+0.124E−03	−0.900E−08

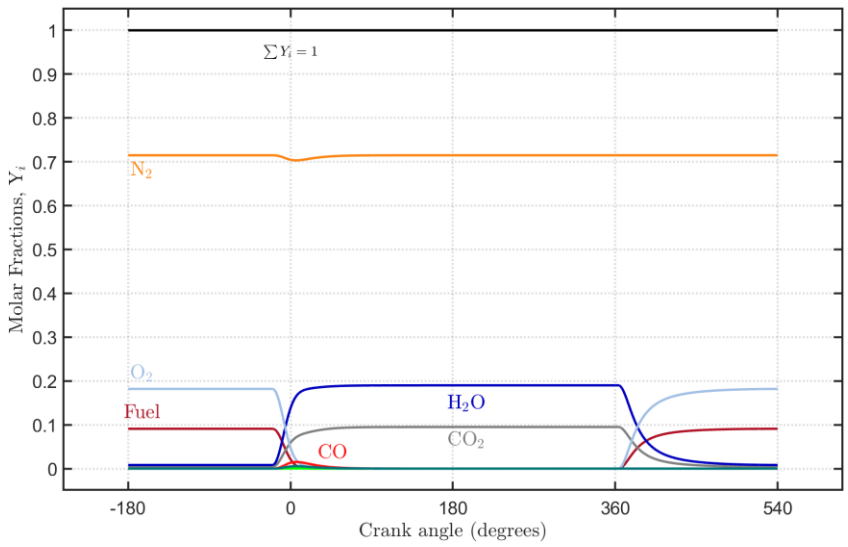

Figure 3.7: ICE species molar fractions over the crank angle for base case analyzed (25/75% H_2+CH_4 blend, SI engine): Major species molar fractions.

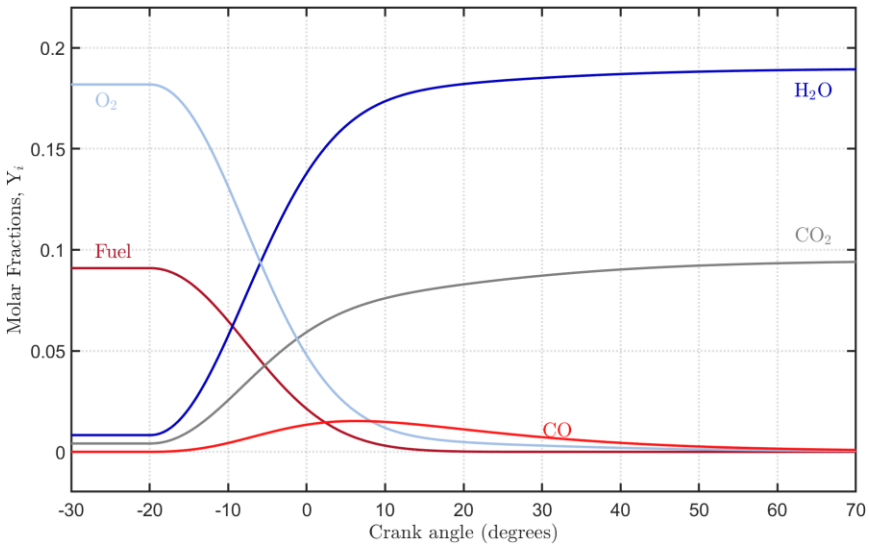

Figure 3.8: ICE species molar fractions over the crank angle for base case analyzed (25/75% H_2+CH_4 blend, SI engine): Combustion phase zoom.

The air-fuel mixture that is directly impacted by the combustion (Fuel and O_2) see their molecular fraction augment in the intake stroke. Then, they are consumed in the combustion and their molecular fraction are transformed into the burned gases (primarily H_2O, CO_2, and CO).

The minor species are illustrated in Figure 3.9. Their behavior with oxygen consumption as a reference can be analyzed. Due to the difference in scale, the minor species molar fractions are multiplied to fit the graph.

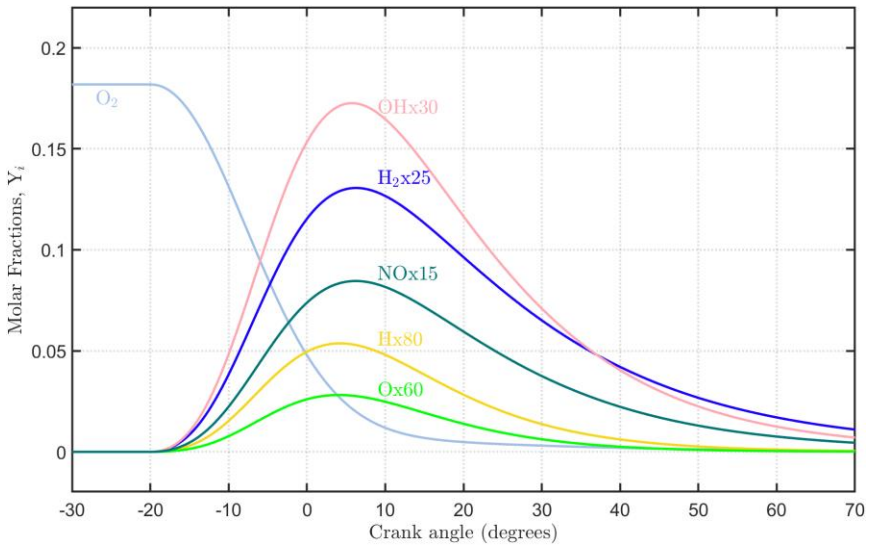

Figure 3.9: Minor species molar fractions as a function of the crank angle for the base case (25/75% H_2+CH_4 blend, SI engine).

The minor species with the highest molar fraction is the radical OH, followed by the radical NO and H_2. The greatest growth of these minor species happens when consumption of oxygen is maximum. Beyond that, their maximum values are reached at the end of the O_2 consumption.

It is fundamental to point out that the fuel and the combustion products are predicted within the unburned and burned volume. Thus, if the fuel or the oxygen does not react, they will account as a burned mass at the end of the combustion. Thereby, everything inside the cylinder is considered as burned at the end of the combustion phase. Similarly, at the opening of the intake valves at the start of the cycle, there will be burned mass inside the cylinder. This burned mass (burned residual mass) is considered an unburned mass with combustion products species. Meaning that inside the cylinder at the start of the cycle there is unburned gas, even though the mixture presents burned species (LEITE; PRADELLE; LEAL, 2021).

3.3.12. NOx Emissions - Zeldovich Mechanism

The most important chemical tool for internal combustion engines that produce NO is the Zeldovich mechanism. This mechanism allow the calculus of NOx emissions accumulated through the cycle, since the NO specie calculated by the chemical equilibrium mechanism refers only to the NO formed instantaneously due to changes in composition of mixture.

Zeldovich's theory indicates that combustion temperature and in-cylinder oxygen concentration are the main factors influencing NOx emissions. Increasing the air dilution ratio by 15%, the main factor causing the increase in NOx emissions is the increase in in-cylinder oxygen concentration. As air dilution continues to increase, the decrease in combustion temperature in the cylinder becomes the main factor contributing to NOx reduction. The exhaust gas contains a large amount of high specific heat capacity and inactive gases, which reduces the cylinder temperature and oxygen concentration in the cylinder, resulting in a significant reduction in NOx (LI et al., 2024).

In this model, NO is formed in the high temperature burned gases behind the flame front. The following three chemical equations form the extended Zeldovich reaction mechanism (MILLER; BOWMAN, 1989):

$$O + N_2 \quad \rightleftharpoons^{k_{1,fwd}}_{k_{1,bwd}} \quad NO + N \tag{3-102}$$

$$N + O_2 \quad \rightleftharpoons^{k_{2,fwd}}_{k_{2,bwd}} \quad NO + O \tag{3-103}$$

$$N + OH \quad \rightleftharpoons^{k_{3,fwd}}_{k_{3,bwd}} \quad NO + H \tag{3-104}$$

where k is the rate constant in $cm^3/(mol \cdot s)$, and the subscripts fwd and bwd indicate, respectively, the forward and backward reactions. Equation (3-103) present the rate constants for the extended Zeldovich reaction mechanism. The coefficients for each rate constant are shown in Table 3.6, (HANSON; SALIMIAN, 1984).

$$k_{Ze} = A_{Ze} \cdot 10^{n_{Ze}} \cdot exp(-B_{Ze}/T) \quad [cm^3/(mol \cdot s)] \tag{3-105}$$

Table 3.6: Zeldovich extended mechanism constants (HANSON; SALIMIAN, 1984)

Reaction	A_{Ze}	B_{Ze}	n_{Ze}
1 - Forward	1.8	38370	14
1 - Backward	3.8	425	13
2 - Forward	1.8	4680	10
2 - Backward	3.8	20820	9
3 - Forward	7.1	450	13
3 - Backward	1.7	24560	14

After Heywood (HEYWOOD, 1976), the rate of change of nitric oxide concentration can be written by the following expression, with the brackets denoting molar concentrations in units of mol/cm^3.

$$\begin{aligned}\frac{d}{dt}[NO] = &+k_{1,fwd}[O][N_2] - k_{1,bwd}[NO][N] + k_{2,fwd}[N][O_2] \\ &- k_{2,bwd}[NO][O] + k_{3,fwd}[N][OH] \\ &- k_{3,bwd}[NO][H]\end{aligned} \tag{3-106}$$

Two hypothesis need to be assumed: first, that the C-O-H system is in equilibrium and is not disturbed by N_2 dissociation, and second, the N atoms change concentration by a quasi-steady process. By these approximations, it can be shown that:

$$\frac{d[NO]}{dt} = \frac{2R_1(1-\xi^2)}{1+\xi\, R_1/(R_2+R_3)} \quad [mol/(cm^3 \cdot s)] \tag{3-107}$$

where ξ is the ratio of the nitric oxide concentration to its equilibrium value ($\xi = \frac{[NO]}{[NO]_e}$), and R_i (i = 1, 2, 3) are rates of reaction, with the equilibrium concentrations with the subscript e:

$$\begin{cases} R_1 = k_{1,fwd}[O]_e[N_2]_e \\ R_2 = k_{2,bwd}[NO]_e[O]_e \\ R_3 = k_{3,bwd}[NO]_e[H]_e \end{cases} \tag{3-108}$$

Finally, the total amount of nitric oxide that appears in the exhaust is computed by summing the mass fractions for all the fluid elements ($\tilde{x}_{NO} = \int_0^1 x_{NO} dx$).

4 Methodology

With all this mathematical modelling, finally the internal combustion engine simulator is modeled. Next step is to develop a methodology for studying its parameters. The Matlab routine allow an easy procedure to change them. Therefore, the study of multiple parameters sensitivity become simple of implementation, even though the interpretation is not so simple. As the simulator gives several performance parameters to analyze, there is a significantly augment of the data to be studied and interpretated.

There are several methods to assess the parameters' sensibility in a process. The most common one is the Univariate Analysis (UA). In this method, the analysis evaluate variable by variable separately. So, for the success of this analysis it is required a great amount of data to study multiple variables. Moreover, it does not consider the impact influence between these factors.

Another well-known approach is the use of a design of experiments (DoE) that allows the investigation of more than one variable and considers possible interaction between the factors in an empirical mathematical model. One of the most common design is the Box-Behnken Design (BBD). It is commonly used in multi-objective response surface methodology (MORSM) to forecast and optimize the operating parameters (SHARMA et al., 2021). In a full factorial central composite design (CCD) 81 operation points are required for five factors, while in the BBD 46 operation points are enough (SHAMUN et al., 2017). Although it is harder to analyze than UA, it has two-factors relations and optimizes data operating points. That is why the simulator operated in a BBD design. A Research flowchart at . Appendices C presents a resume of the steps followed in this work to reach the results.

4.1. Numerical Integration

To solve a linear system of equations of three independent variables, three independent equations are required to have a single solution. In this work, the three independent variables are those derived from pressure and temperature (burned and unburned) with respect to crank angle. For these three variables, there are three equations: conservation of mass, conservation of energy and conservation

of entropy in the unburned region. The system of equations to be solved is represented in a matrix form at equation (4-1).

$$\begin{bmatrix} A_1 & B_1 & C_1 \\ A_2 & B_2 & C_2 \\ A_3 & B_3 & C_3 \end{bmatrix} \cdot \begin{bmatrix} \frac{dP}{d\theta} \\ \frac{dT_u}{d\theta} \\ \frac{dT_b}{d\theta} \end{bmatrix} = \begin{bmatrix} D_1 \\ D_2 \\ D_3 \end{bmatrix} \quad (4\text{-}1)$$

With the solution to this system of equations, it is necessary to solve three differential equations to calculate the properties (P, T_u and T_b) of the next stage of the simulation.

After a quick assessment, it is noted that the system of equations in the intake, compression and exhaust strokes has only two independent variables and, thus, two equations. There are no gases burned in the intake and compression strokes, so there is no need to calculate the burning temperature (equation (4-2)). In the exhaust stroke, there are no unburned gases, and only two independent variables (equation (4-3)). In these cases, only the mass and energy conservation equations are needed to execute the simulation. In the power stroke, however, there are burned and unburned gases. In this case, all three conservation equations are needed to solve the problem.

$$\begin{bmatrix} A_1 & B_1 \\ A_2 & B_2 \end{bmatrix} \cdot \begin{bmatrix} \frac{dP}{d\theta} \\ \frac{dT_u}{d\theta} \end{bmatrix} = \begin{bmatrix} D_1 \\ D_2 \end{bmatrix} \quad (4\text{-}2)$$

$$\begin{bmatrix} A_1 & C_1 \\ A_2 & C_2 \end{bmatrix} \cdot \begin{bmatrix} \frac{dP}{d\theta} \\ \frac{dT_b}{d\theta} \end{bmatrix} = \begin{bmatrix} D_1 \\ D_2 \end{bmatrix} \quad (4\text{-}3)$$

The derivative' equations were previously calculated and implemented in the program with another resolution method, a Matlab function called ODE45 (LEITE, 2021). However, in the present work, it was found that ODE45 did not work correctly for the new questions to be solved. The resolution steps, set as a default parameter, were used only to visualize the results, while the resolution of the equations was done with a random step determined by the function. Thus, in this work, no other Matlab numerical calculation function was used to obtain the

derivative results. The entire iterative procedure for solving the system of conservation' equations was built and implemented directly in the Matlab routine to solve the integration by a finite analysis of the derivatives instead of using a preexisting Matlab function.

4.2. Convergence Criteria

The internal combustion engine is a heat engine that works in cyclic mode. Therefore, it is expected that some properties also show cyclical behavior. The mass, pressure and temperature at the beginning theoretically must be the same as at the end. In addition to these properties, the initial temperature of the unburned gas, mole fractions and residual fraction must be the same, or at least similar at the beginning and end of the cycle. The Matlab routine operated in cycles that started in the compression stroke and ended in the intake stroke. Then, convergence criteria were modeled to force these cyclical properties.

The engine simulation will run until all three convergence criteria are met simultaneously. Both pressure, temperature and residual fraction must have a maximum error of the relative difference between the initial and final values of 1%. These criteria are, respectively: $\left|\frac{P_i - P_f}{P_i}\right| < 1\%$, $\left|\frac{T_{u,i} - T_{u,f}}{T_{u,i}}\right| < 1\%$ and $\left|\frac{F_i - F_f}{F_i}\right| < 1\%$. Besides, maximum error to mass was considered tolerable under 5%.

The routine compares the initial and final pressure and temperature values at the end of the cycle. If the convergence requirements are not met, it restarts with the new initial values being the final values from the previous iteration. If convergence is not satisfied by the 20th attempt, the program stops. Using the simulator showed that convergence is normally achieved in the third or fourth iteration.

4.3. Box-Behnken Design and Engine Parameters

Statistical tools have often been applied to optimize analytical methods to reduce the number of experiments to be performed, resulting in less use of resources for experiments and considerably less laboratory work. Furthermore, these methods allow the development of mathematical models that allow evaluating the relevance and statistical significance of the effects of the factors studied, as well as evaluating the impact of interactions between the factors. If there are significant interaction effects between the factors, the optimal conditions indicated by univariate studies will be different from the correct results of

multivariate optimization. The greater the interaction effects, the greater the difference that will be found using univariate and multivariate optimization strategies. Therefore, the univariate procedure may fail, since the effect of one variable may be dependent on the level of the others involved in the optimization. This is why multivariate optimization schemes involve designs in which the levels of all variables are changed simultaneously (FERREIRA et al., 2007).

Among the possible design of experiments (DoE) approach, some are dedicated to screening or predictive modeling with polynomial mathematical models (mostly, linear or quadratic). As the expected behavior of the engine is not linear and presented optimized operational conditions, the chosen DoE response with multiple regression's analysis is a second-order polynomial fitted model, as expressed in the equation (4-4).

$$Y = \beta_0 + \sum \beta_i X_i + \sum \beta_{ii} X_i^2 + \sum \beta_{ij} X_i \cdot X_j \qquad (4\text{-}4)$$

where Y is the predicted response, β_0 is the intercept coefficient, β_i is the linear coefficient, β_{ii} is the quadratic coefficient, and β_{ij} is the interaction coefficient.

Box-Behnken Designs (BBD) (BOX; BEHNKEN, 1960) are a class of rotatable or nearly rotatable second-order designs based on three-level incomplete factorial designs. For three factors, its graphical representation can be seen in Figure 4.1.

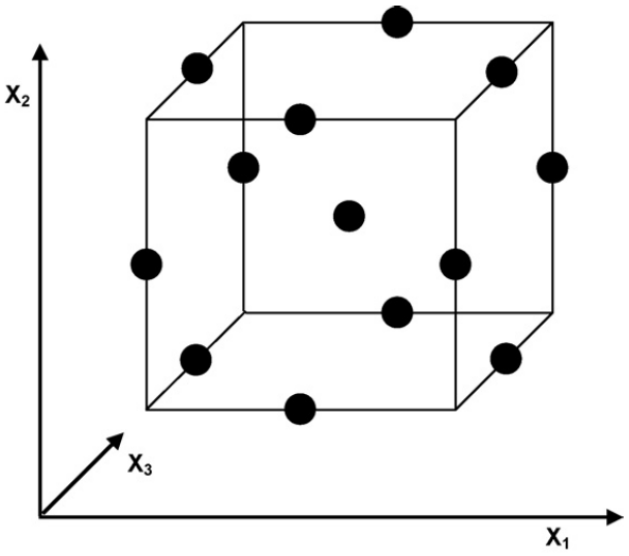

Figure 4.1: Illustration of the Box-Behnken design for three factors. Source: (FERREIRA et al., 2007).

A comparison between the BBD and other response surface experiments (central composite, Doehlert matrix, and three-level full factorial design) demonstrated that the BBD and the Doehlert matrix are slightly more efficient than the central composite design. But much more efficient than three-level full factorial designs. Another advantage of the BBD is that it contains no combinations for which all factors are simultaneously at their highest or lowest levels. Therefore, these designs are useful to avoid experiments carried out under extreme conditions, for which unsatisfactory results may occur. On the other hand, they are not suitable for situations where it is necessary to know the answers at the extremes, that is, at the vertices of the cube (FERREIRA et al., 2007).

The BBD for four and five factors can be organized into orthogonal blocks. Due to block orthogonality, the second-order model can be augmented to include block effects without affecting the parameter estimates, i.e., the effects themselves are orthogonal to the block effects. This orthogonal blocking is a desirable property when experiments need to be organized into blocks and block effects are likely to be large (FERREIRA et al., 2007).

To study the sensitivity of the performance parameters, it is necessary to select the model factors. In this work, the effects that are going to be studied are: percentage of H_2 ($\%H_2$), engine speed (RPM), fuel-air equivalence ratio (ϕ), intake pressure (P_{IV}) and valve overlap (VO) on SACI engines.

The performance parameters to be analyzed are indicated thermal efficiency (η_{th}), fuel mass (m_{fuel}), fuel energy (E_{fuel}), NOx emissions (NOx/kWh) and CO_2 emissions (CO_2/kWh). For each performance parameter, the influence of all factors and their linear relations are studied.

The calculus was performed using the Statistica software (version 14). Finally, the most influential parameters are analyzed. The factors (X) and performance parameters' (Y) symbols are percentage of H_2 (X_1), engine speed (RPM), fuel-air equivalence ratio (ϕ), intake pressure (P_{IV}) and valve overlap; indicated thermal efficiency (Y_1), specific NOx emissions (Y_2), specific CO_2 emissions (Y_3), and fuel energy (Y_4).

Knowing the DoE's properties desired, and the number of factors involved, it is possible to calculate the total number of simulations. These calculations are based on the sum of points at the center at each edge: $2k \cdot (k-1)$ and Central points (C_0), where k is the number of factors. The factor's value for each test are presented in Table 4.1. With the regression's coefficient, it is possible to study the impact of the factors on the response. Afterwards, it will be discussed Pareto

Charts, observed values, predicted values, and their residuals, for every performance parameter.

The Pareto Chart evidence the most important factors in a large set of them. This assessment is useful for prioritizing certain factors in univariate analysis later. The effects of the factors investigated are divided into linear, quadratic, and linear x linear two-factor interactions, with all effects listed in their order of significance. Additionally, the red line indicates whether the factor has a statistically important effect on the respective response. A low p value, that is, $p < 0.05$, indicates that the factor has a significance level of 5%. In this work, it was defined that a factor is significant if it has more than this 5% significance.

The *Observed vs. Residual Values* diagrams introduce the quality of the BBD model in the analysis. As previously mentioned, this model takes the linear and quadratic's factor effects and linear x linear two factor interactions into account.

In Table 4.2, the 21st test represents the one in which all the factors are at the central values. Due to the numerical nature of the study, the central point was variated around the central values to generate some uncertainty to simulations (tests 42 to 47).

The starting point of the study was to generate data for types of car engines in the simulations. Thus, the engine geometry adopted was a 1.8 L four-cylinder. It is worth mentioning that the only changes made to the simulator were the factors. The basic engine geometry remains the same in all tests. The complete engine specification is presented in Table 4.2, same as the one used by LEITE (2021). This engine specification is adequate for light duty vehicles comparison.

Table 4.1: BBD tests

Tests	$\%H_2$	RPM	ϕ	P_{IV}	VO
01	-1.00	-1.00	0.00	0.00	0.00
02	1.00	-1.00	0.00	0.00	0.00
03	-1.00	1.00	0.00	0.00	0.00
04	1.00	1.00	0.00	0.00	0.00
05	0.00	0.00	-1.00	-1.00	0.00
06	0.00	0.00	1.00	-1.00	0.00
07	0.00	0.00	-1.00	1.00	0.00
08	0.00	0.00	1.00	1.00	0.00
09	0.00	-1.00	0.00	0.00	-1.00
10	0.00	1.00	0.00	0.00	-1.00
11	0.00	-1.00	0.00	0.00	1.00
12	0.00	1.00	0.00	0.00	1.00
13	-1.00	0.00	-1.00	0.00	0.00
14	1.00	0.00	-1.00	0.00	0.00
15	-1.00	0.00	1.00	0.00	0.00
16	1.00	0.00	1.00	0.00	0.00
17	0.00	0.00	0.00	-1.00	-1.00
18	0.00	0.00	0.00	1.00	-1.00
19	0.00	0.00	0.00	-1.00	1.00
20	0.00	0.00	0.00	1.00	1.00
21	0.00	0.00	0.00	0.00	0.00
22	0.00	-1.00	-1.00	0.00	0.00
23	0.00	1.00	-1.00	0.00	0.00
24	0.00	-1.00	1.00	0.00	0.00
25	0.00	1.00	1.00	0.00	0.00
26	-1.00	0.00	0.00	-1.00	0.00
27	1.00	0.00	0.00	-1.00	0.00
28	-1.00	0.00	0.00	1.00	0.00
29	1.00	0.00	0.00	1.00	0.00
30	0.00	0.00	-1.00	0.00	-1.00
31	0.00	0.00	1.00	0.00	-1.00
32	0.00	0.00	-1.00	0.00	1.00
33	0.00	0.00	1.00	0.00	1.00
34	-1.00	0.00	0.00	0.00	-1.00
35	1.00	0.00	0.00	0.00	-1.00
36	-1.00	0.00	0.00	0.00	1.00
37	1.00	0.00	0.00	0.00	1.00
38	0.00	-1.00	0.00	-1.00	0.00
39	0.00	1.00	0.00	-1.00	0.00
40	0.00	-1.00	0.00	1.00	0.00
41	0.00	1.00	0.00	1.00	0.00
42	-0.04	0.07	0.00	-0.20	0.20
43	0.00	-0.07	0.14	0.00	-0.20
44	0.04	0.00	-0.14	0.20	0.00
45	-0.04	-0.07	-0.14	0.00	-0.20
46	0.00	0.00	0.00	0.20	0.20
47	0.04	0.07	0.14	-0.20	0.00

Table 4.2: Engine Specification for the BBD tests

Geometric parameters	
Number of cylinders	4
Bore (mm)	83
Stroke (mm)	81.4
Half-stroke to Rod Ratio	0.271
Total Displacement Volume (cm^3)	1761
Compression ratio, r_c	10(SI) or 17(SACI)
Valve timing	
IVO	0°aTDC
IVC	45°aBDC
EVO	***Variable***
EVC	***Variable***
Operating point	
Engine speed (rpm)	***Variable***
Fuel type	***Variable***
Equivalence ratio, ϕ	***Variable***
P_{IV} (bar)	***Variable***
T_{IV} (K)	380
T_{EV} (K)	480
Wiebe parameters	
a_W	***Variable***
θ_s	-20°
$\theta_{d,SI}$	46°
$k_{W,SI}$	***Variable***
$\theta_{d,HCCI}$	11°
$k_{W,HCCI}$	6.00

5 Results and Discussion

In this chapter, the influence of multiple factors on the performance of the SACI engine will be presented. It will be divided into four parts. Firstly, the engine simulator will be validated for SI engines with valve overlap. Leite et al. (LEITE; PRADELLE; LEAL, 2021) had previously validated the code for SI and HCCI engines without valve overlap. In the second (Case Study), the same central case studied by Leite et al. (LEITE; PRADELLE; LEAL, 2021) will be analyzed. The third is the BBD study itself, discovering the most significant factors for each performance parameter. The fourth is the UA of the main factors for the responses.

5.1.Validation

The engine for comparison comes from an experiment in a SI engine made by Caton (CATON, 2016). Almost all the results presented in his study are for the same engine: a 5.7-liter, V–8 configuration with a bore and stroke of 101.6 and 88.4 mm, respectively. For the Wiebe combustion parameters, the following values were used as recommended by Heywood (HEYWOOD, 1988): k = 3.0 and a = 5.0. The combustion duration was 60°CA. The cylinder heat transfer is calculated with the correlation recommended by Woschni (WOSCHNI, 1967). Table 5.1 lists the engine specifications.

Table 5.1: Engine specifications and input parameters (CATON, 2016)

Geometric parameters	
Number of cylinders	8
Bore (mm)	101.6
Stroke (mm)	88.4
Half-stroke to Rod Ratio	0.305
Total Displacement Volume (cm^3)	5733
Compression ratio, r_c	8
Valve parameters	
IVO	357°aTDC
IVC	-136°aTDC
D_{IV} (mm)	50.8
$L_{IV,max}$ (mm)	10
EVO	116°aTDC
EVC	371°aTDC
D_{EV} (mm)	39.6
$L_{EV,max}$ (mm)	10
Valve overlap (°CA)	14
Operating point	
Engine speed (rpm)	1400
Fuel type	Isooctane
Equivalence ratio, ϕ	1.0
P_{IV} (kPa)	50
T_{IV} (K)	319.3
P_{EV} (kPa)	102.6
Cylinder wall temperature (K)	450
Wiebe parameters	
a_W	5.0
θ_s	-22
$\theta_{d,SI}$	60°
$k_{W,SI}$	3.0

Now, it is possible to enter the combustion parameters as initial data in the Matlab engine simulator and run the model with Caton engine specification. Some performance parameters such as maximum burned temperature, break mean effective pressure, thermal efficiency, total trapped mass, and maximum pressure can be compared between the numerical simulation and the experimental results.

It can be noted that the maximum burned temperature has an error of only three percent. These parameters values and their relative errors are presented in Table 5.2. Additionally, the temperature and the BMEP also are slightly higher than the reported values. Such behavior is consistent with the expected impact of a higher mass within the cylinder.

Table 5.2: Engine comparison

Parameter	**Experiment**	**Model**	ϵ
$T_{b,max}$ (K)	2554	2634	+3.13%
BMEP (kPa)	324.6	337.3	+3.91%
η_{th}	31.5	31.4	-0.00317%
$m_{trapped}$ (g/cyl)	0.3609	0.3898	+8.01%
P_{max} (kPa)	1904	2451	+28.7%

To transform the other parameters, that were calculated in the model as indicated, into brake, it is necessary to use a friction correlation model (FMEP). Chen et al. (CHEN et al., 2021) compared some FMEP models. Although this model has been improved by some researchers, Pipitone (PIPITONE, 2009), after careful investigation, stated that “the Chen-Flynn model can also well predict FMEP if the constants are carefully calibrated.” And this model contains key engine operating parameters, differing from other models as Heywood one (HEYWOOD, 1988). In this model, the FMEP (bar) is calculated by $FMEP = A + B \cdot P_{max} + C \cdot S_f + D \cdot S_f^2$, where $S_f = \frac{\omega * S}{2}$. Therefore, this model was used, and the constants were calibrated through simulation results.

It can be observed that the numerical model generally represented the experiment well, with relative errors of less than 5% for maximum burning temperature, BMEP and thermal efficiency. However, the mass trapped in the closed system during the simulation cycle is greater than the mass presented in the experiment, showed in Figure 5.1. From this picture, it is clear that this variation in mass (~0.39g in simulation results and ~0.36g in Caton results, after IVO and before θ_s) significantly influences the increase in pressure, the variable that presented a large error in its maximum value (Table 5.2).

Due to that, some parameters needed to be re-evaluated. The difference in mass was mostly at begin and end of the iteration. Even presenting all the other variables converging, such as pressure, unburned temperature, residual fraction, specific volume, and molar fractions, the in-cylinder mass did not converge at begin

and end point. It was found that the mass entering the cylinder in the part of intake stroke after -180°CA (start point of simulations) was being summed two times, severely affecting the mass convergence. Another approximation was that a similar error was happening with residual mass, that is, the residual burned mass present inside the cylinder right after EVC and before IVO, was repeatedly being summed to the in-cylinder mass over the part of intake stroke that happens before 540°CA. With these considerations, the convergence criteria to mass diminished and could be considered within an acceptable error ($\epsilon < 0.05$). Most of the tests presented an error $\epsilon < 0.01$, that is the convergency criteria to pressure, unburned temperature, and residual fraction, but in all tests the maximum error for mass calculus was found to be under 5%.

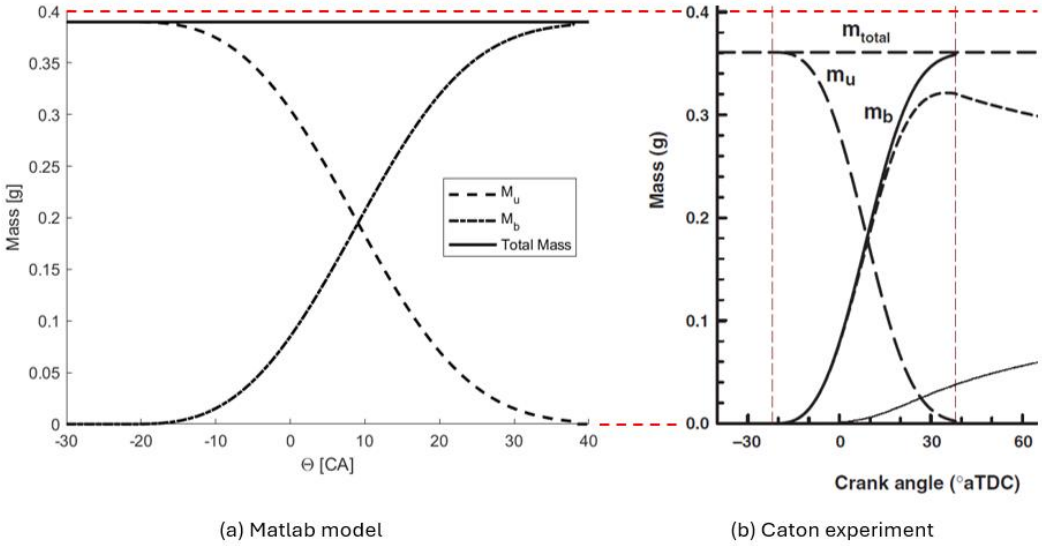

Figure 5.1: Cylinder mass in the various zones as functions of crank angle for the base case conditions. Source: (CATON, 2016) and Matlab routine.

5.2. Heat Transfer Correlations Analysis

The four heat transfer correlations presented in section 3.3.7 were analyzed by the MATLAB™ routine to the central point of the Box-Behnken Design to the SACI engine. Considering the Hohenberg correlation as the reference, it can be seen in the Figure 5.2 that the simulator presents similar results for Woschni, Hohenberg and Eichelberg. On the other hand, Sitkei correlation presented big difference from the other correlations.

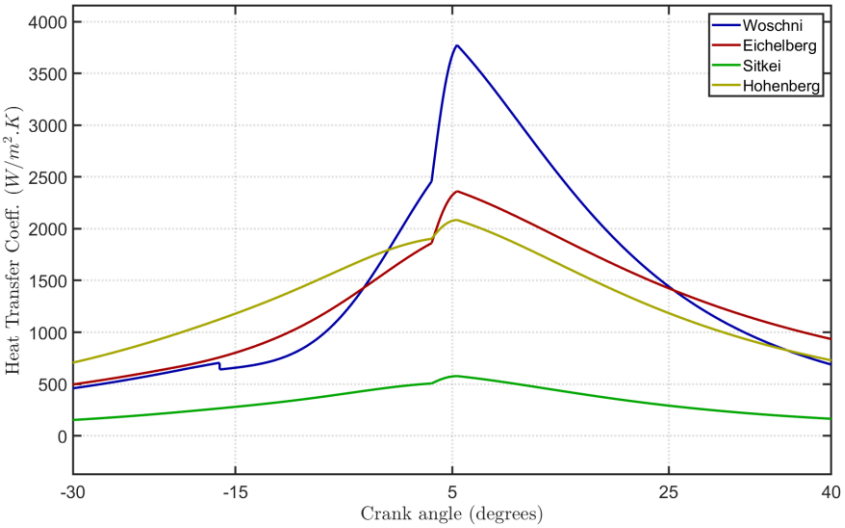

Figure 5.2. Instantaneous Cylinder Average Heat Transfer Coefficient for base case (25/75% H_2+CH_4 blend, SACI engine).

Analyzing the results of the performance parameters, shown in Table 5.3, the Eichelberg and Woschni correlations, respectively, differ from the Hohenberg correlation in the following proportions: -2.34% and -2.89% to η_{th}; +17.46% and +31.81% to specific NOx; +2.73% and +3.16% to specific CO_2. Both Eichelberg and Woschni showed more pronounced divergence for specific NOx than for thermal efficiency and specific CO_2, with Woschni's correlation being more pronounced than for Eichelberg's. The results of the Sitkei correlation were confirmed as unacceptable due to the high divergence from the reference.

Table 5.3. Performance parameters comparison for base case (25/75% H_2+CH_4 blend, SACI engine) in relation to heat transfer correlation analyzed.

Heat Transfer Correlation	η_{th}(%)	Specific NOx (g/kWh)	Specific CO_2 (g/kWh)
Woschni	29.90	1.56E-1	121.95
Sitkei	35.24	3.15E-1	102.51
Hohenberg	30.79	1.18E-1	118.21
Eichelberg	30.07	1.39E-1	121.44

On the other hand, (IHSAN SHAHID et al., 2024) research developed a comparative study about the effects of several heat transfer correlations (Woschni, Nusselt, Hohenberg, Han, Eichelberg, and Assanis correlations) over performance parameters (maximum pressure, IMEP and heat transfer rate) by varying hydrogen fractions, EGR ratios, engine speeds and load conditions on a hydrogen-compressed natural gas engine (heavy-duty spark ignition engine/bus). These

heat transfer models were systematically incorporated into a quasi-dimensional combustion model (QDCM) on Matlab using absolute percentage errors of the specified IMEP and maximum pressure within 5 % average error in case of calibration. For IMEP, Woschni's correlation presented the smallest absolute percentage deviations for all operation conditions. For maximum pressure, Woschni model presented the lowest mean of absolute percentage error sample points (2.17%) without calibration with reference to the maximum pressure. In relation to Eichelberg and Hohenberg's correlations, both presented higher deviations, with Hohenberg presenting the worst ones for IMEP and similar errors for maximum pressure.

The heat transfer correlation used to all Box-Behnken Design tests and univariate analysis was Woschni correlation, considering that Leite (2021) and Caton (2016) also used Woschni's correlation. Such correlation is conservative in terms of thermal efficiency and specific emissions.

5.3. Baseline Case Study for SACI engine

To understand the SACI mechanism in the ICE Matlab simulator and study the main responses of this new type of multimode combustion, the simulator result for the BBD center point case will be analyzed. In this configuration, the fuel composition in the hydrogen/methane blends ($\%H_2$), operating point (Engine speed, ϕ, and P_{IV}), and valve overlap are presented in the 21st test at Table 4.1. For comparison, the baseline case study for SI engine is at the . Appendices D.

Figure 5.3 illustrates the behavior of the SACI mass fraction burned (combustion progress) as a function of the crank angle. It is possible to note that SACI combustion begins as SI combustion, but when the precursor mass reaches the critical mass for self-ignition, the combustion rate increases, and the unburned gases burn in the HCCI form.

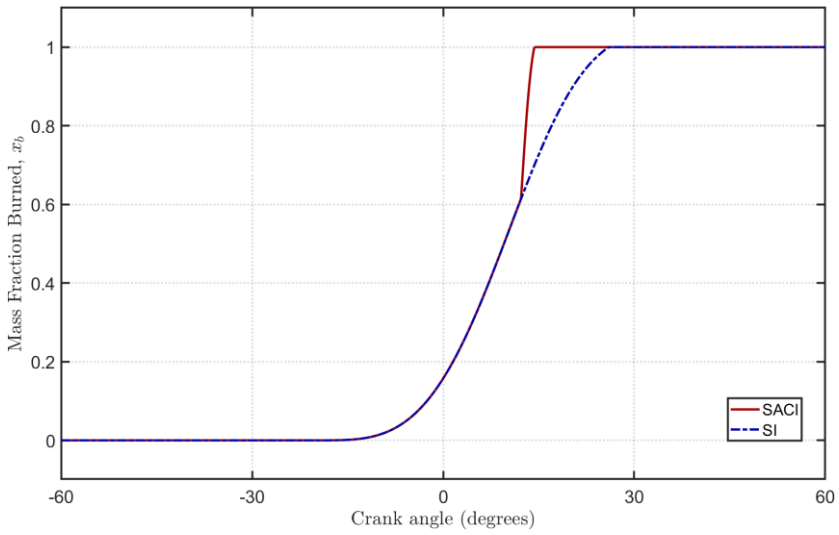

Figure 5.3: Mass fraction burned versus the crank angle in the BBD central point study for SACI engines.

Moreover, we see that the mixture reaches the auto-ignition state right before the TDC. This limit is obtained in $\theta = 12.2°aTDC$, as suggested by the simulator. In HCCI and SACI engines, the auto-ignition timing is normally considered to happen at the TDC, showing in this case a delay to the ideal auto-ignition timing (AIT). It can be justified based on the intake pressure (P_{IV}) used in the central point case (1.0 bar).

Figure 5.4 presents the pressure curve in the presence of the valves timing when compared to the motored pressure and Figure 5.5 focus on the difference between the motored and in-cylinder pressures at the combustion phase.

It can be observed that in the combustion phase, close to the beginning of combustion, the pressure in the cylinder is lower than the motorized pressure. This happens because the motorized pressure does not consider the heat transfer of the gas. The SACI numerical simulation, however, takes this into account at each stage of the simulation.

Due to the delay in AIT, pressure increases very fast after this point, the mass burns almost completely likely in a SI combustion. The remaining mass burns almost immediately after 12.2°aTDC because the additional pressure resulting from the start of the SACI combustion.

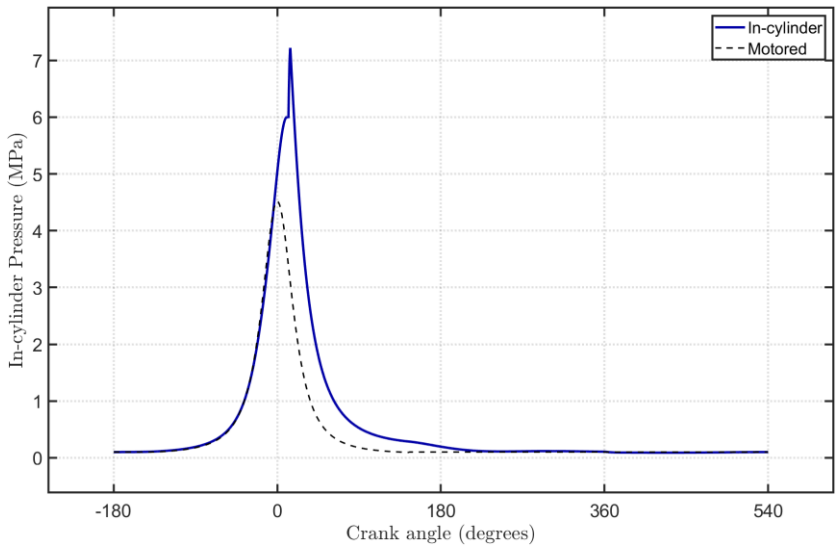

Figure 5.4: Pressure versus the crank angle in the BBD central point study for SACI engines.

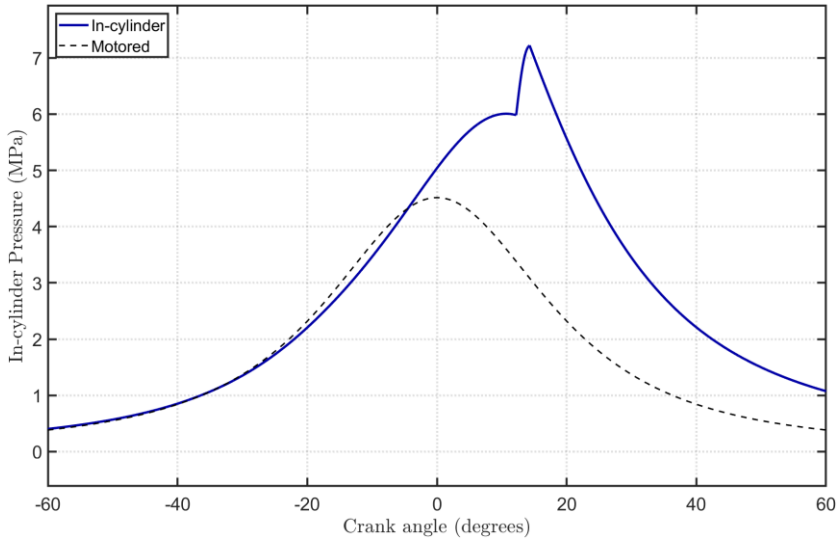

Figure 5.5: Combustion phase zoom of the pressure versus the crank angle in the BBD central point study for SACI engines.

Figure 5.6 shows burned, unburned, and average temperatures versus crank angle. The temperature at the inlet is low, close to ambient temperature. When the intake valve closes, the temperature of the unburned gases begins to increase rapidly until reaching its maximum near the end of combustion. Then, heat transfer causes the temperature of the burned gases to decrease. Finally, opening the exhaust valve allows the temperature of the burned gas to decrease even further.

HCCI and SACI combustion modes are low-temperature combustion methods. In this kind of engine, due to the leaner air-fuel mixture, the temperature inside the cylinder is not as high as in SI engines. However, comparing this curve

temperature with the temperature of Appendix A, it can be seen no big differences into SI and SACI engines at the central point case. Even though pressure is slightly higher in SACI engine, the temperature shows to have a similar behavior in two engines. Again, this behavior can be explained by the delay in AIT.

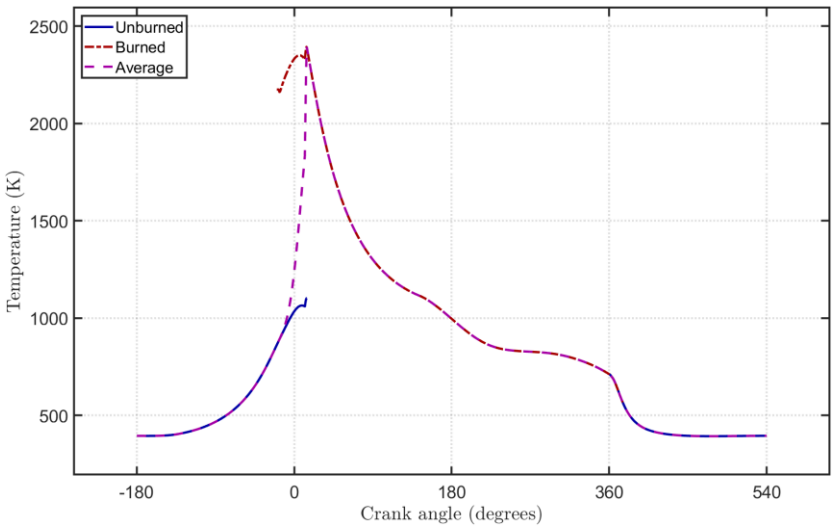

Figure 5.6: Temperature versus the crank angle in the BBD central point study for SACI engines.

The work and heat plot, in Figure 5.7, demonstrates that it is in the power stroke that the gross work is performed. Furthermore, gross heat loss occurs after TDC, when the average gas temperature is high. At the end of the cycle, a cylinder produces approximately 0.31 kJ of work and loses 0.16 kJ as heat transfer to the walls and coolant.

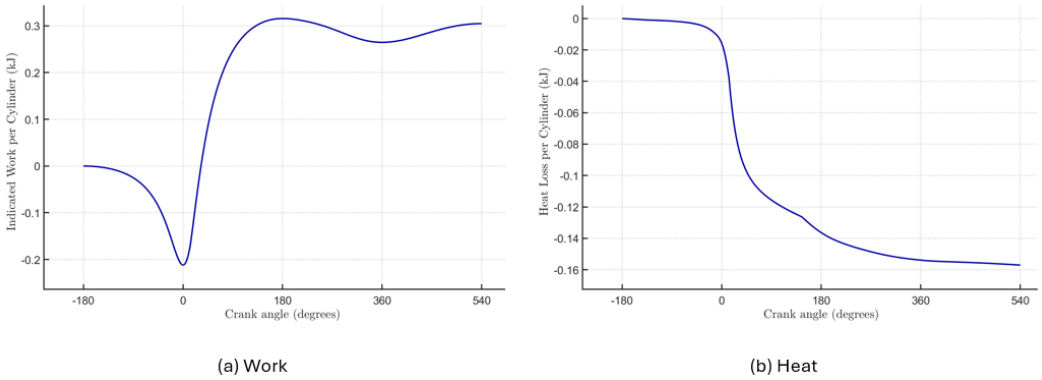

Figure 5.7: Work and heat versus crank angle.

Figure 5.8 points the mass in the cylinder as a function of the crank angle. It increases in the intake course until it reaches 4 g. Then, it reduces slightly because of the blowby, having 1.06% less mass in EVO compared to IVC, which corresponds to the blowby mass seen in Chapter 3. Besides, it can be noted that mass showed to be a harder to reach convergence criteria and does not attain the general criteria of 1% of relative error, which justifies the acceptance of a softer convergence criteria ($\epsilon_m < 5\%$).

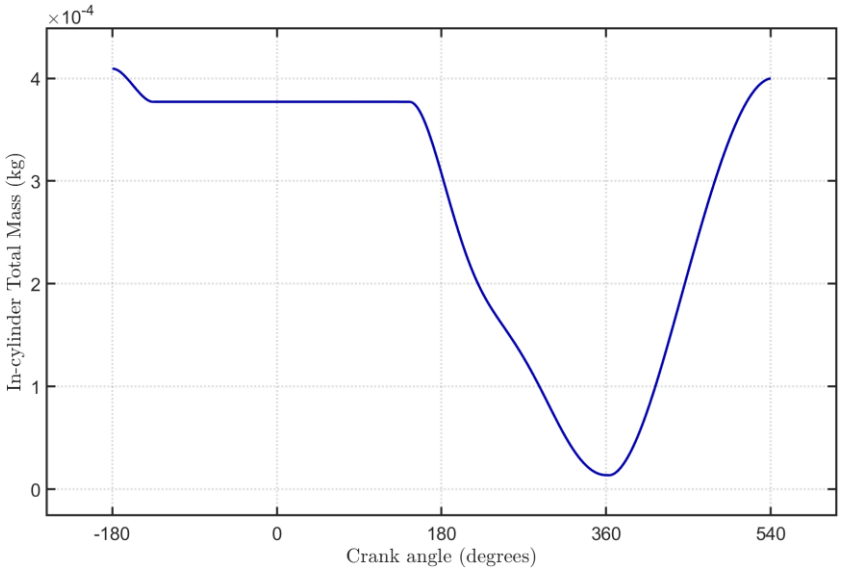

Figure 5.8: Mass in SACI engines.

Finally, the major species' molecular fraction during the combustion phase is represented in Figure 5.9. As expected, there is oxygen at the end of combustion. It is justified by the fuel-air equivalence ratio of 0.65 of the engine. Furthermore, the chemical species' production/destruction rate change is illustrated. It happens at the AIT.

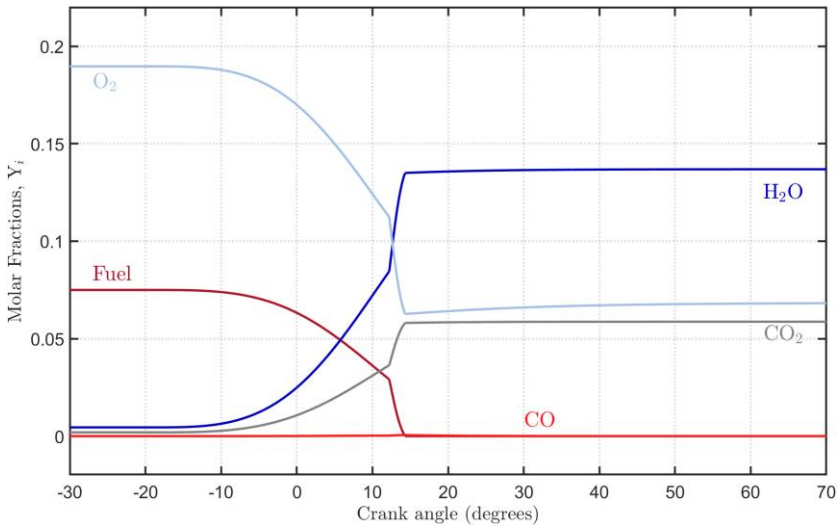

Figure 5.9: Major molar fractions in SACI engines.

Figure 5.10 shows the combustion process in the minor species molecular fraction as a function of the crank angle with the O_2 as a reference for the combustion timing. As can be seen, the combustion of HCCI significantly affects the mole fractions of the minor species, just as it does for the major species. The highest minor species are the radical NO, followed by OH, O, and the radical H_2.

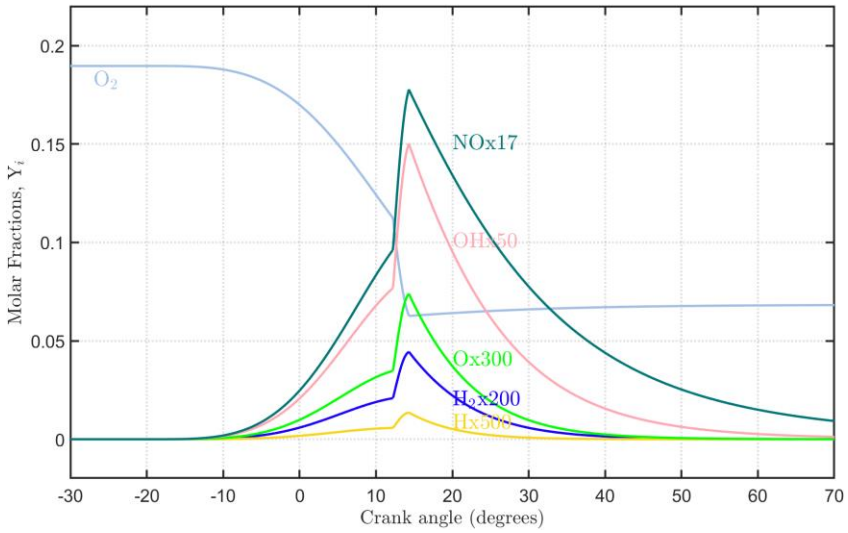

Figure 5.10: Minor species molar fractions in SACI engines.

5.4. Univariate Analysis

To better visualize the impacts of factors on the performance of the SACI engine and compare them with the SI engine, a Univariate Analysis can be performed. Therefore, five different studies were carried out:

1. Percentage of H_2 in fuel blend variation.
2. Engine speed variation.
3. Equivalence ratio variation.
4. Intake pressure variation.
5. Valve overlap variation.

The subsequent tests are performed with the engine specification from Table 4.2, as previously done by LEITE (2021). The performed simulations in both engines (SI and SACI) may help in the comparison of these two different combustion techniques. In order to realize a valid parallel between them, they will be performed at their normal operating points. Thus, the factors which do not variate during each UA will acquire the default values from Table 5.4.

Table 5.4:SI and SACI Default Parameters

Parameter	SI	SACI
$\%H_2$	25	25
Engine speed (rpm)	3000	3000
ϕ	1.0	0.65
P_{IV} (bar)	1.0	2.5
Valve overlap (°CA)	0	0

5.4.1. Percentage of H_2 in fuel blend variation

For the first UA, the engine's performance parameters with a variation in percentage of H_2 in fuel blend will be studied. Since the percentage of H_2 is a factor that is significant to all three performance parameters evaluated in BBD, all performance parameters were plotted. Percentage of H_2 ranged between 0 and 50%, with a step of 12.5%.

The first engine performance parameter analyzed is the thermal efficiency, in Figure 5.11.

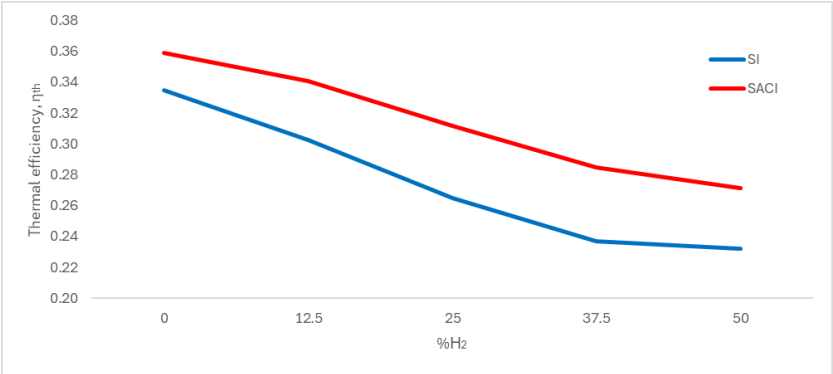

Figure 5.11: Thermal efficiency vs. Percentage of H_2.

It is possible to see that SACI and SI thermal efficiencies maximum values are between the percentages of 0 – 12.5% of H_2. But SACI thermal efficiency is slightly higher. With the increase in percentage of H_2, thermal efficiency keeps dropping, maintaining the tendency of $\eta_{th}^{SACI} > \eta_{th}^{SI}$. Thermal efficiency of SACI engine is 7% to 17% more efficient than SI engine.

DIMITROVA et al. (2022) analyzed HCCI engines fueled with very lean hydrogen/hydrogen peroxide mixtures and showed that, for the same equivalence ratio, increasing the hydrogen percentage generally reduces thermal efficiency. This is reasonable considering the ignition delay induced by the addition of hydrogen. It can be explained by concepts of density, flammability and burning velocity in air of the fuels (Table 3.2). Hydrogen compared to methane has smaller density, wider flammability limit, requires much less energy to initiate combustion and has a bigger burning velocity in air, the flame front caused by further addition of hydrogen delays ignition to values closer to 0 CAD aTDC. Evaluating the time data of burning progress for both engines (Table 5.5 and Table 5.6), it is found a reduction of 14% and 12% for SI and SACI engines, respectively, in burn duration by increasing percentage of H_2. Which has an adverse effect on thermal efficiency, due to the reduction of maximum pressure that diminishes the indicated work for both engines (Figure 5.12 and Figure 5.13).

Table 5.5: Correspondents crank angles (CA) of 1%, 10%, 90% and 99% of mass fraction burned and burn duration for SI engine

Percentage of H_2	CA1	CA10	CA90	CA99	Burn duration (CA)
0	-18.12	-14.24	5	25.99	44.11
12.5	-14.12	-7.22	15.19	25.99	40.11
25	-11.01	-2.56	20.39	25.99	37
37.5	-10.08	-1.13	21.74	25.99	36.07
50	-11.85	-3.56	20.04	25.99	37.84

Table 5.6: Correspondents crank angles (CA) of 1%, 10%, 90% and 99% of mass fraction burned and burn duration for SACI engine

Percentage of H_2	CA1	CA10	CA90	CA99	Burn duration (CA)
0	-18.12	-14.24	-8.01	-5.91	12.21
12.5	-14.12	-7.22	-3.05	-1.68	12.44
25	-11.01	-4.86	-0.88	-0.09	10.92
37.5	-10.08	-4.6	-0.63	-0.02	10.06
50	-11.85	-5.85	-1.87	-1.07	10.78

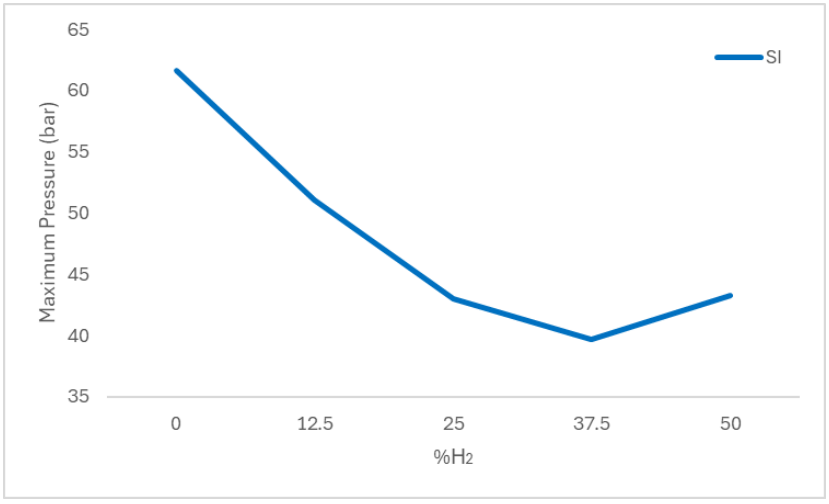

Figure 5.12: Maximum Pressure vs. Percentage of H_2 for SI engine.

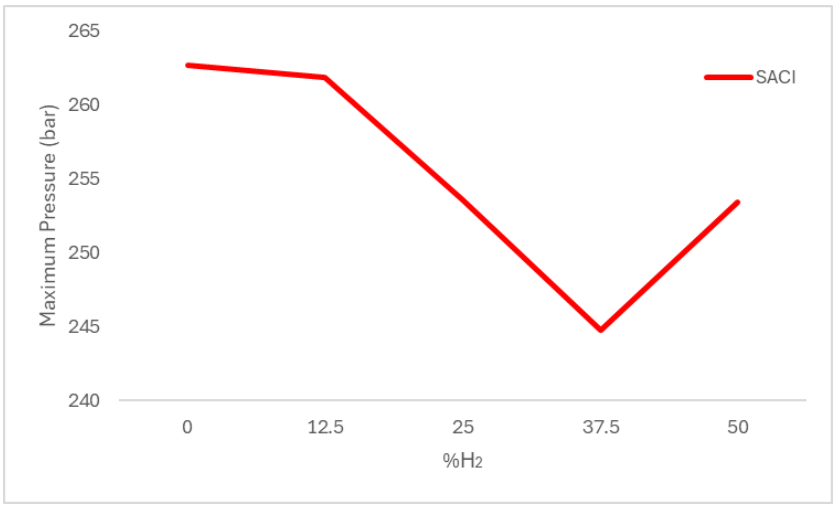

Figure 5.13: Maximum Pressure vs. Percentage of H_2 for SACI engine.

In Figure 5.14, it is possible to see that the NOx emissions under low percentages (0% to 12.5%) of H_2 are up to 64% smaller to SACI than for SI engine.

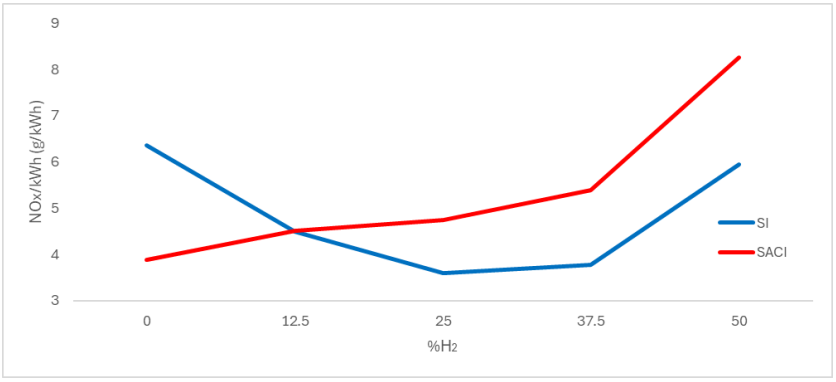

Figure 5.14: Specific NOx emission vs. Percentage of H_2.

But NOx emissions to SACI engine grow while the percentage of H_2 is increased. This behavior is in accordance with the literature for SI and CI engines, indicating that more H_2 leads to high temperatures in the combustion chamber which increase the formation of NOx (DI IORIO; SEMENTA; VAGLIECO, 2014; NADALETI et al., 2017).

In Figure 5.15, it is possible to see that the CO_2 emissions under low percentages of H_2 are the highest to both engines.

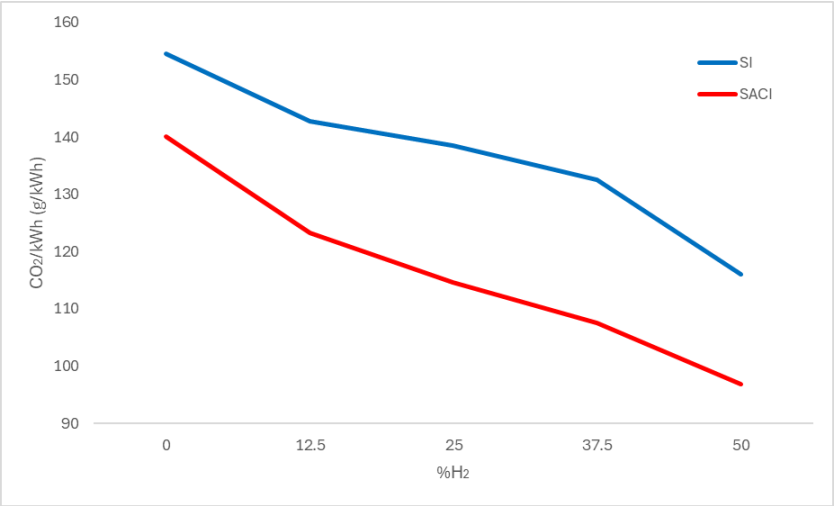

Figure 5.15: Specific CO_2 emission vs. Percentage of H_2.

Increasing the percentage of H_2, CO_2 emissions decreases showing an opposite tendency between this factor and response. CO_2 emissions are 10 to 23% smaller to SACI engine than to SI engine.

The literature reports basically two important factors to justify the reduction of CO_2 emitted when H_2 blended with methane: the reduction of present carbon atoms due to greater presence of H_2; and the burning rate of hydrogen: with higher maximum in-cylinder pressure and temperature, the CO_2 production mechanism approximates the equilibrium condition (DI IORIO; SEMENTA; VAGLIECO, 2014; NADALETI et al., 2017).

5.4.2. Engine speed variation

Engine speed is ranged between 1500 and 4500 rpm, with a step of 500 rpm, allowing the study of its impact on the performance parameters. The three performance parameters were plotted.

From Figure 5.16, it is possible to affirm that, under normal operation conditions, SACI engine is 12% to 16% more efficient than SI engine when varying engine speed.

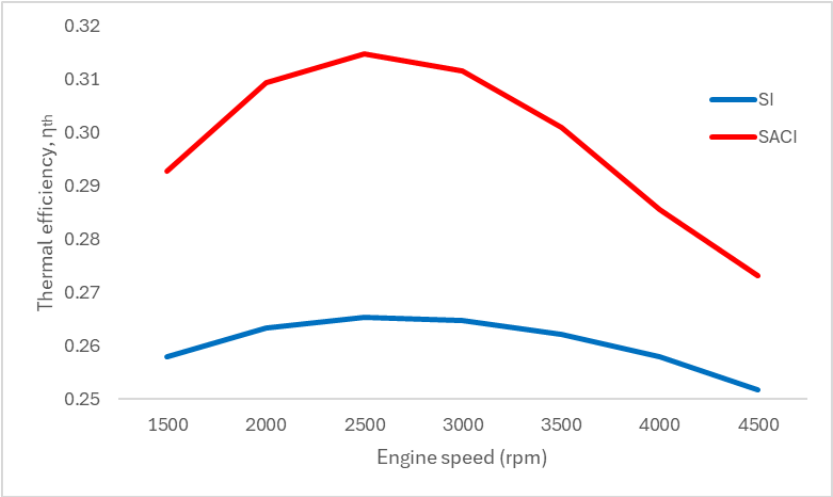

Figure 5.16: Thermal efficiency vs. engine speed.

Engines thermal efficiencies shown an increasing pattern from 1500 to 3000rpm and a decreasing pattern after this, agreeing with literature data that indicates this may occur due to the fact that flame propagation speed is more sensitive to fuel–air ratio at lower speeds (SINGH; SONAWANE; AGARWAL, 2022; YANG et al., 2023). Additionally, SACI engine's thermal efficiency drops significantly after 3000 and 3500 rpm. After 3000 rpm, the injected fuel energy for SACI engine decreases ($E_{fuel,1500} = 2.2533 \frac{kJ}{cycle}$; $E_{fuel,3000} = 2.2455 \frac{kJ}{cycle}$; $E_{fuel,3500} = 2.2335 \frac{kJ}{cycle}$; $E_{fuel,4500} = 2.1670 \frac{kJ}{cycle}$) leading to a reduction of maximum pressure ($Pmax_{1500} = 250.87\ bar$; $Pmax_{3000} = 253.57\ bar$; $Pmax_{3500} = 252.73\ bar$; $Pmax_{4500} = 243.96\ bar$), diminishing the thermal efficiency which justifies the SACI strategy implementation at lower engine speeds (WANG et al., 2010).

From Figure 5.17, one can see that specific NOx emissions when related to the variation of engine speed to SACI engine is higher (33% to 10%) than to SI engine.

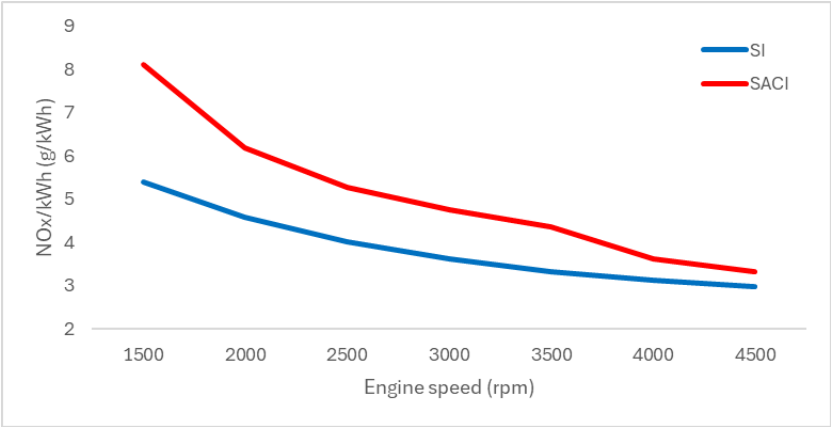

Figure 5.17: Specific NOx emission vs. engine speed.

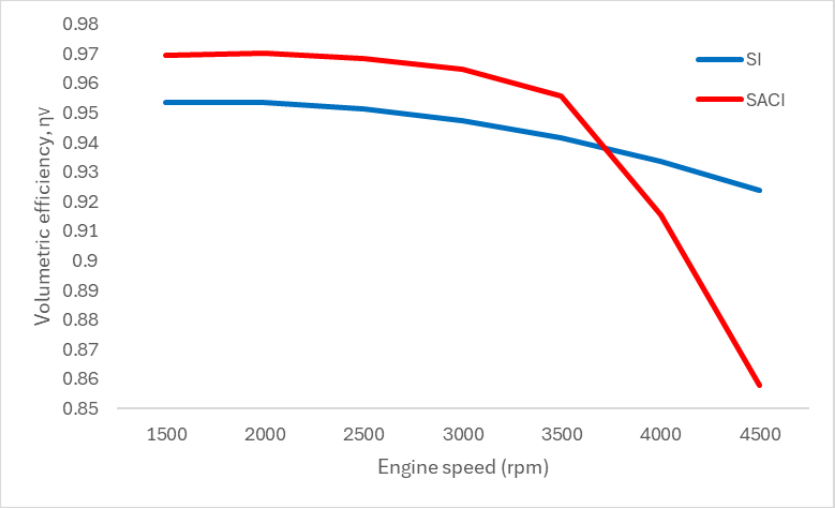

Figure 5.18: Volumetric efficiency vs. engine speed.

The variation of NOx emissions for SI engine remained low for all engine speeds, probably due to little correlation of gas temperature trends and speed (YANG et al., 2023). The smaller difference between SI and SACI NOx emissions is at 4500 rpm. It can be explained by the SACI volumetric efficiency tendency over the engine speed variation (Figure 5.18). Volumetric efficiency decreases significantly after 3500 rpm. Maximum temperature shows the same behavior, increasing until 3500rpm and decreasing after it ($Tmax_{1500} = 2546.30\ K$; $Tmax_{3000} = 2574.40\ K$; $Tmax_{3500} = 2578.00\ K$; $Tmax_{4500} = 2562.20\ K$). Therefore, with the drop in temperature, the chemical kinetics cannot maintain the high formation of this product (Figure 5.19) and NOx emissions fall.

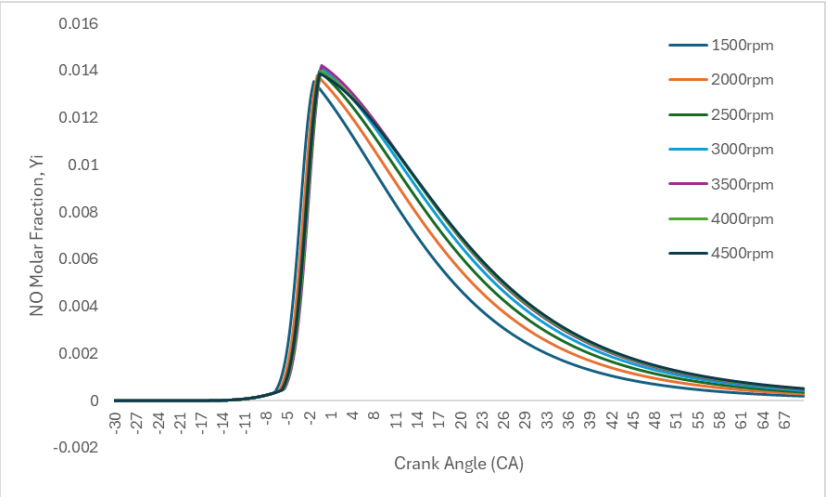

Figure 5.19: NO molar fractions vs. crank angle (°CA) at different speed engines for SACI engine.

From Figure 5.20, one can see that specific CO_2 emissions are considerably smaller to SACI engine than to SI engine.

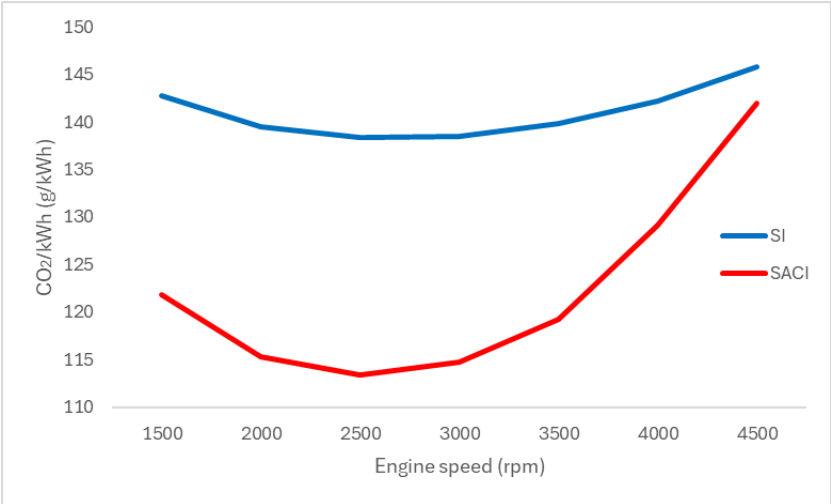

Figure 5.20: Specific CO_2 emission vs. engine speed.

The fluctuation amplitude of CO_2 production for SACI engine increased significantly with the increment of engine speed, which is mainly due to more time for mixing resulting in the more homogeneous distribution of fuel mixture in the cylinder at lower speeds (YANG et al., 2023). Furthermore, the CO_2 emissions to SACI engine increase significantly after 3500rpm. It also can be explained by the volumetric efficiency. Leaner combustions imply in less O_2 available inside the cylinder hindering the combustion to be more efficient. So, with less air less fuel

molecules are burned, and more molecules of CO_2 are formed (ZHANG et al., 2023).

5.4.3. Equivalence ratio variation

To further understand the influence of the air-fuel equivalence ratio on engine performance parameters, the SACI fuel-air mixture equivalence ratio was varied from 0.3 to 1.0, due to its operation being between mixtures poor and very poor, and SI fuel-air equivalence ratio of 0.9 to 1.1.

In Figure 5.21, it is notable that that there is an optimal point for maximizing thermal efficiency over fuel-air equivalence ratio variations.

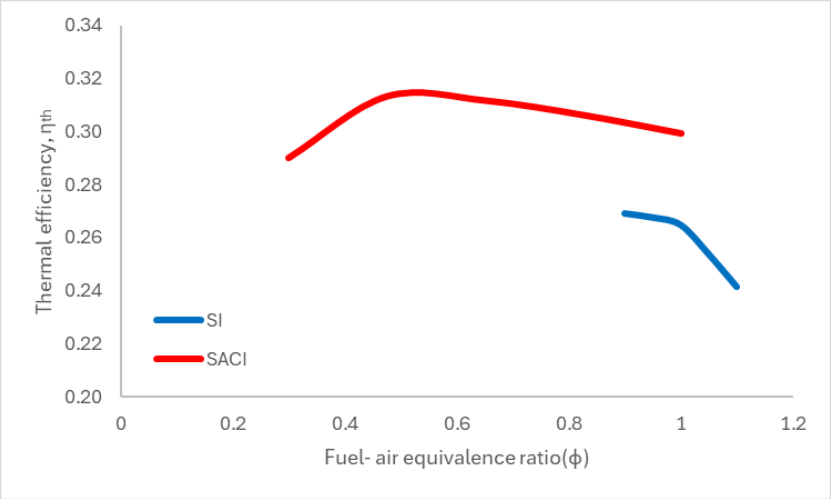

Figure 5.21: Thermal efficiency vs. fuel-air equivalence ratio.

In this case, the maximum efficiency is obtained at a leaner mixture of $\phi = 0.5$ to SACI engine, around $\eta_{th} = 31\%$. Looking at this image, SACI engine seems not to be much more efficient than SI engine. Nevertheless, this operation condition is not the optimal one and the AIT happened sooner than it is expected. Consequently, it is possible to say that even out of surroundings of the optimal operational point, SACI engine overcome the optimal SI thermal efficiency value. In addition, ZHAO et al. (2023) investigated SI and SACI engines fueled with gasoline and PODE under the same range of lean equivalence ratios and loads. They showed that SACI engine is more efficient (between 27% and 49%) than SI engine while varying equivalence ratio.

Recent publication (YANG et al., 2023) shown that the variation of thermal efficiency increased as the mixture become richer for SI engines fueled with

gasoline, which probably happens due to an increase in the change of combustion speed. They also indicated that IMEP behaves in opposition to thermal efficiency behavior in relation to equivalence ratio. Previous studies (HEYWOOD, 1988) also indicated that the trend of thermal efficiency over equivalence ratio was opposite to that of IMEP. HAGOS et al. (2019) had either indicated an ascending tendency of IMEP over leaner mixtures, enabling the conclusion that thermal efficiency increases as the amount of fuel in the fuel-air mixture increases.

Figure 5.22 shows that specific NOx emissions start to increase significantly in SACI engines when gets closer to stoichiometric mixtures.

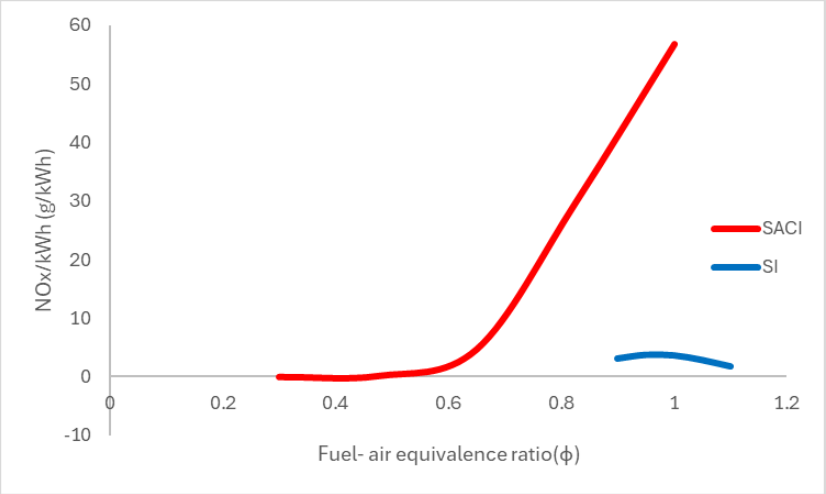

Figure 5.22: Specific NOx emission vs. fuel-air equivalence ratio.

NOx emissions decrease as equivalence ratio decreases for SACI engine, due to the increase in the compression stroke temperature leading pressure to increase the reactivity of the fuel. Furthermore, the change from SI to CI combustion reduces the high-temperature duration (ZHU et al., 2024).

In relation to SI engine, it can be said that this is the main difference of SACI engine. By operating with lean fuel-air ratios, its NOx emissions are low but still higher than SACI's NOx emissions.

Figure 5.23 shows that specific CO_2 emissions also have optimal operational points.

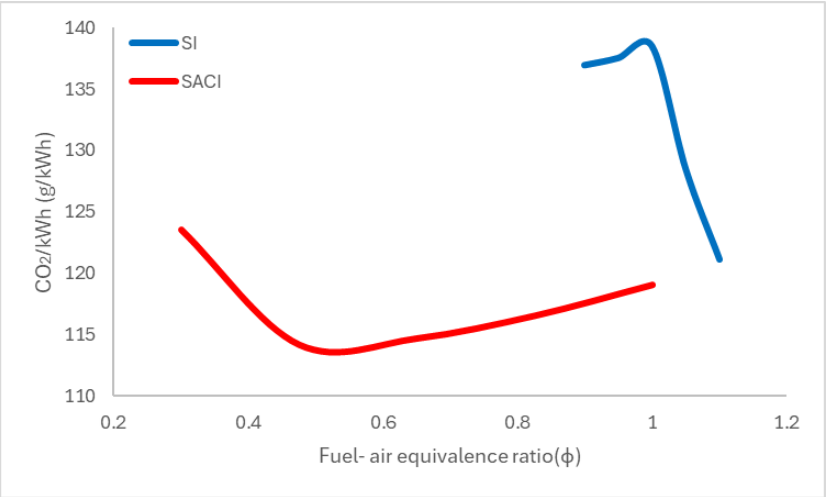

Figure 5.23: Specific CO_2 emission vs. fuel-air equivalence ratio.

For SACI engine, it happens at $\phi = 0.5$. And to SI engine, at $\phi = 1.1$. At these points, the CO_2 emissions are the smallest of each engine. Additionally, SACI engine presents to have an emission 6% smaller than SI engine emission at the optimal points.

The CO_2 emissions decrease gradually to SI engine as the mixture concentration increases from lean to rich. This is due to the lack of oxygen in the cylinder due to the concentration of the mixture and the incomplete oxidation of carbon in the fuel to CO_2 (LI et al., 2022).

For SACI engine, it is shown that CO_2 emissions is very sensitive to the equivalence ratio, followed by nitrogen oxides, in accordance with literature (ALI, 2017). This probably occurs due to difference between complete and incomplete combustion processes (YANG et al., 2023). The increase in CO_2 emissions is not surprising, since increasing the equivalence ratio means introducing more carbon-based fuel into the engine and, therefore, it is expected that CO_2 emissions also increase, as it is one of the main combustion products (DANDAJEH; SANUSI; AHMADU, 2020).

5.4.4. Intake pressure variation

The SACI's intake inlet manifold pressure was set from 1 to 3 bar, and SI range was set from 0.9 to 1.2 bar. As SACI combustion was first idealized to extend the HCCI load range, indicates this study the working path of intake pressures with a wider range for the SACI engine. The intake pressure range for SI engine was set to be around the working commercial values.

Figure 5.24 shows the thermal efficiency versus the intake pressure variation.

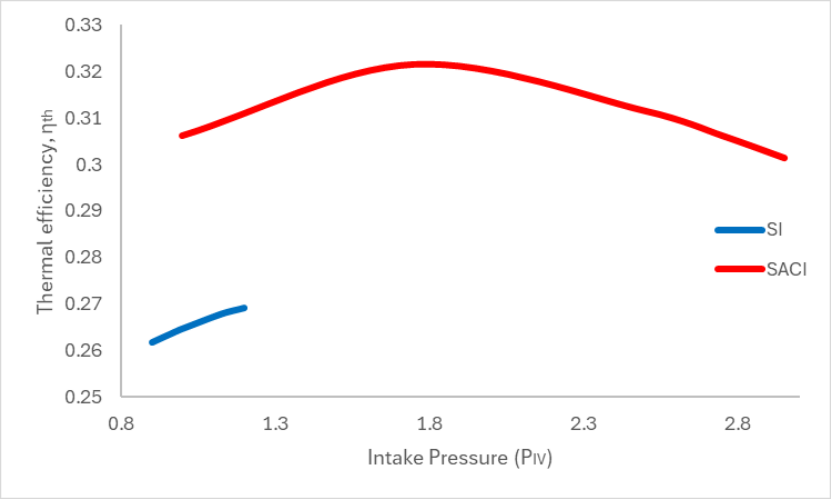

Figure 5.24: Thermal efficiency vs. the intake pressure variation.

Analyzing the image, SACI engine presents thermal efficiency to increase up to a maximum and a subsequent considerable decrease according to intake pressure increase. All the pressures were already high, and this context associated with early combustion, because of spark timing that had remained constant at -20°aTDC, made pressures increase even more. Thus, by the combustion occurring early, SACI combustion worked against the thermal efficiency after 1.8kPa of intake pressure (LEITE, 2021). Comparing the regions of the same pressure range for both engines, it is notable that the thermal efficiency pattern is to rise with augment of intake pressure (YANG et al., 2023) and that SACI thermal efficiency is significantly higher than SI engine one.

NOx emissions as a function of the intake pressure are illustrated in Figure 5.25.

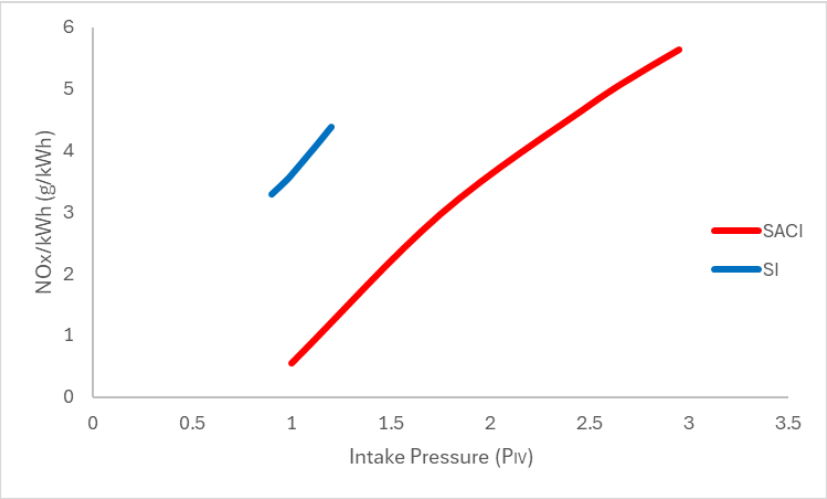

Figure 5.25: Specific NOx emission vs. intake pressure variation.

YANG et al. (2023) studied the influence over emission by increasing intake pressure. They showed nitrogen oxide emissions were sensitive to different loads. For the same fuel-air ratio, a heavier engine load increased nitrogen oxide emissions, which was probably due to the fact that the presence of richer mixtures at higher loads favored this variation.

Increasing the load increases the heat release without necessarily changing its capacity to exchange heat with the external environment (increasing the area is impossible and the change in the heat transfer coefficient is not significant). Resulting in an increase of maximum temperature, as observed in the simulations ($Tmax^{SACI}_{P_{IV}=1bar} = 2393.90\ K\ and\ Tmax^{SACI}_{P_{IV}=3bar} = 2585.20\ K\ \Longrightarrow \uparrow 8\%$; $Tmax^{SI}_{P_{IV}=0.9bar} = 2713.10\ K\ and\ Tmax^{SI}_{P_{IV}=1.2bar} = 2736.30\ K\ \Longrightarrow \uparrow 1\%$;).

From this comparison, it can be observed that for the SACI engine, in the range of 1 to 2.35 bar, NOx emissions are lower than or at most equal to the maximum NOx emission of the SI engine analyzed. Over 2.35 bar, NOx emissions of SACI engine are higher than that of SI engine. But at the same intake pressure conditions, SACI engines are eight times greener than SI engines.

Analyzing Figure 5.26, it is notable that there is a significant difference between SACI and SI engines specific CO_2 emissions.

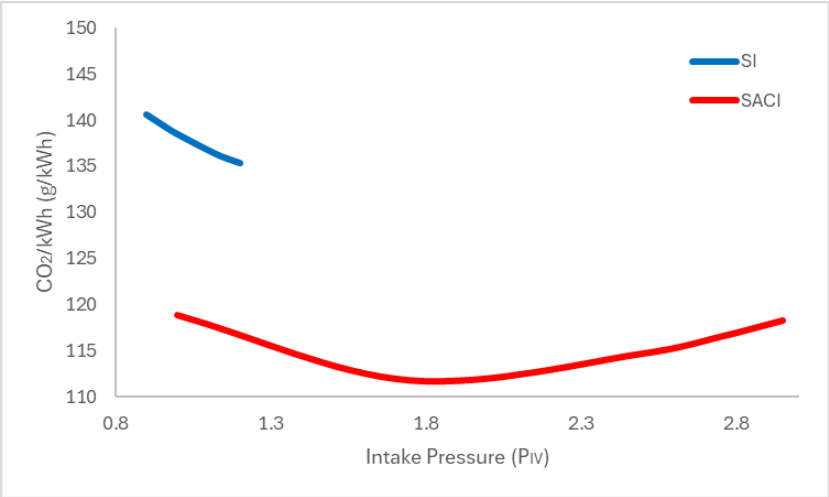

Figure 5.26: Specific CO_2 emission vs. intake pressure variation.

SACI engines are at all its range of application at least 12% greener than SI engines. On the other hand, for each of the engines the CO_2 emissions had little variation under different intake pressures (YANG et al., 2023).

5.4.5. Valve overlap variation

As previously mentioned in Chapter 2, there are two categories of valve overlap, negative (NVO) or positive valve overlap (PVO). XIE et al. (2013b) analyzed both strategies and showed that PVO to their operational conditions worked better. It was the expected influence of valve overlap with the simulations realized. It is also important to remember that the conditions applied at the univariate analysis was not the optimal conditions for both engines. The BBD statistical results (discussed in section 5.5) did not show significance of valve overlap coefficients in any complete or reduced models. So, the following univariate analysis was made over a step of 2.5°CA as a way of understanding better the effect of valve overlap to performance parameters of the engines.

Figure 5.27 shows the thermal efficiency versus the valve overlap variation.

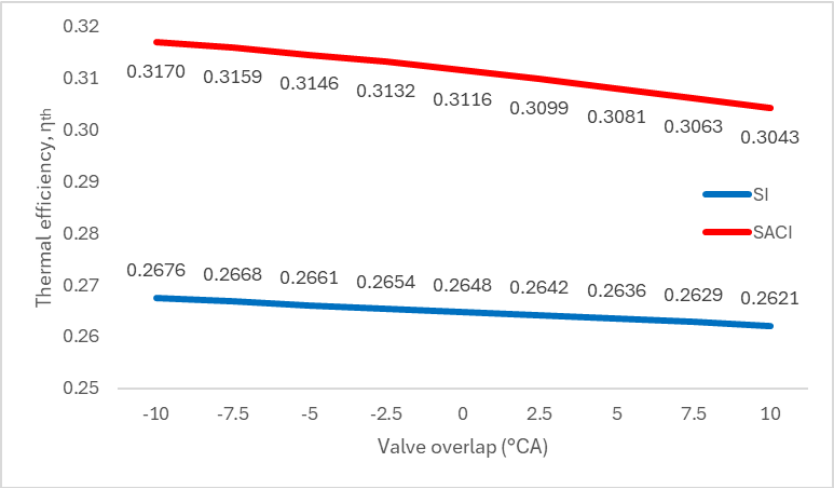

Figure 5.27: Thermal efficiency vs. the valve overlap variation.

It is notable that over the tests, the efficiency of the engines did not show significant variability to thermal efficiency. But it can be seen that with the higher NVO (-10°CA), both engines presented the highest thermal efficiencies. It can be explained by the bigger burned mass remaining inside the cylinder before the piston to arrive the TDC ($m_{-10°}^{SACI} = 2.7133 \cdot 10^{-05} kg \; and \; m_{+10°}^{SACI} = 1.5575 \cdot 10^{-05} kg \Longrightarrow \downarrow 43\%$; $m_{-10°}^{SI} = 2.0979 \cdot 10^{-05} kg \; and \; m_{+10°}^{SI} = 1.6457 \cdot 10^{-05} kg \Longrightarrow \downarrow 22\%$), increasing the temperature and pressure state of the initial conditions to the next cycle. Besides, the SACI thermal efficiency of -10°CA valve overlap is around 1% bigger than the efficiency at +10°CA, that can be explained by the much more diluted mixture at the EVC with +10°CA of PVO.

Figure 5.28 shows the relation between specific NOx emissions and valve overlap variation.

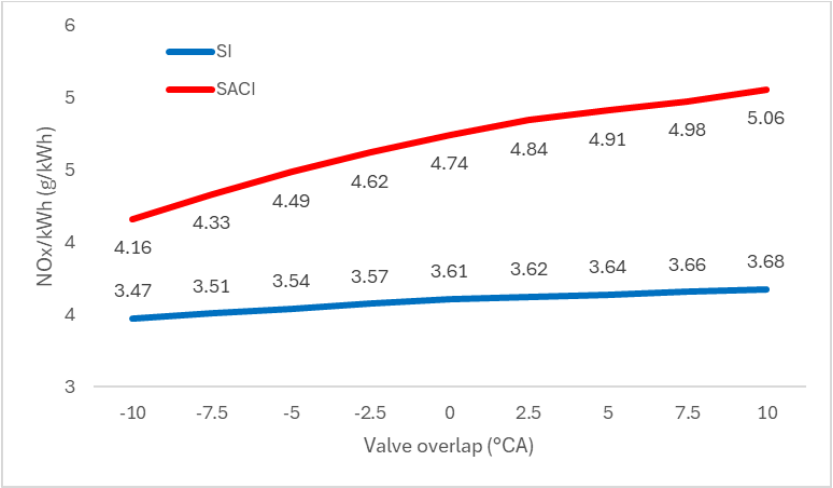

Figure 5.28: Specific NOx emissions vs. valve overlap variation.

At its normal operational conditions, SACI engine shows to emit more NOx than SI engine. The valve overlap shows to significantly affect the SACI engine emissions. NVO presents to have smaller NOx emissions than PVO. Additionally, the largest NVO have a NOx emission almost 20% smaller than the largest PVO to SACI engine. This reduction for SI engine is of approximately 6%, indicating that NVO influences less SI engines. Analyzing the temperature behavior, it can be seen that as the valve overlap moves in the direction of NVO, smaller are the maximum and means temperatures of the cycle for both engines, showing that even a small difference in temperature can cause a significant drop in NOx emissions, primarily to SACI engines ($Tmax_{-10°}^{SACI} = 2562.50\ K,\ Tmean_{-10°}^{SACI} = 800.64\ K, Tmax_{+10°}^{SACI} = 2578.70\ K\ and\ Tmean_{+10°}^{SACI} = 814.12\ K;\ Tmax_{-10°}^{SI} = 2716.60\ K,\ Tmean_{-10°}^{SI} = 1040.32\ K, Tmax_{+10°}^{SI} = 2721.20\ K\ and\ Tmean_{+10°}^{SI} = 1050.84\ K$). Besides, the fuel-air equivalence ratio (ϕ) remained constant for both engines ($\phi^{SACI} = 0.65\ and\ \phi^{SI} = 1$). Since efficiency drops slightly from NVO to PVO, the observed effect for NOx emissions is mainly due to efficiency drop.

Lastly, Figure 5.29 shows the relation between specific CO_2 emissions and valve overlap variation.

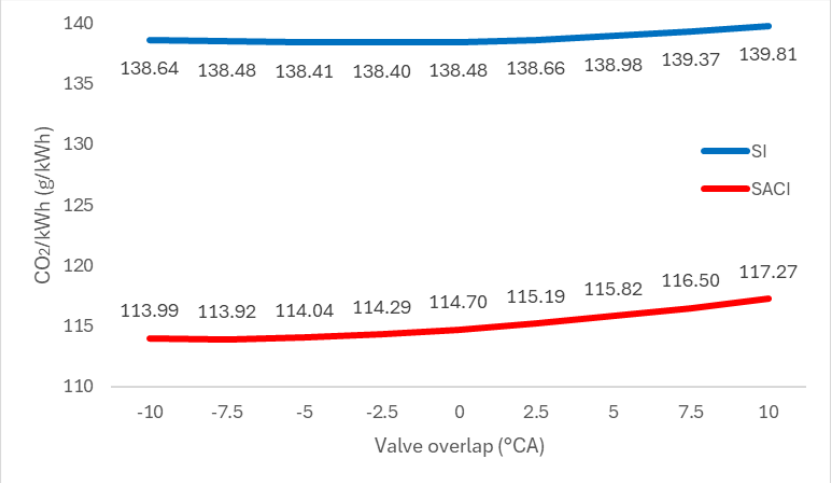

Figure 5.29: Specific CO_2 emissions vs. valve overlap variation.

Similarly to effect over thermal efficiency, valve overlap variation does not present significant variability in specific CO_2 emissions for both engines. Moreover, the optimal points of this analysis are different from the previous two observations. To SACI engine, CO_2 emission is numerically smallest at -7.5°CA. To SI engine, CO_2 emission is numerically smallest at -2.5°CA. But in both cases the immediate previous and later values are not significantly different from each other.

5.5. BBD Parameter Study

In this section, it is going to be studied the BBD model and analyzed the five responses for each test performed for SI and SACI engines and presented in Table 5.7 and Table 5.8, respectively. Besides, all the complete second-order polynomial regression models for the responses are at the . Appendices E, from Table E.1 to Table E.8.

Table 5.7: BBD Results for SI engine

Tests	η_{th} (%)	NOx (mg/kWh)	CO_2 (g/kWh)	E_{fuel} (kJ/cycle)
01	37.86	35.06	138.73	0.7293
02	27.44	29.68	99.72	1.0621
03	38.17	24.08	138.18	0.7056
04	26.40	20.05	104.02	1.0288
05	21.41	0.00	189.09	0.2259
06	26.65	180.92	142.97	0.6679
07	35.76	0.00	103.60	0.6748
08	30.14	495.07	119.97	2.0265
09	31.39	14.27	119.84	0.9248
10	30.85	8.91	125.02	0.8905
11	31.31	14.86	118.88	0.9258
12	29.27	10.81	126.64	0.9003
13	41.08	0.00	130.32	0.3500
14	28.80	0.00	96.99	0.5243
15	37.47	569.22	138.12	1.0642
16	25.97	530.59	103.71	1.5142
17	27.40	6.21	146.36	0.4570
18	33.21	15.12	111.49	1.3735
19	27.07	6.90	143.38	0.4587
20	32.35	18.31	112.80	1.3875
21	31.71	11.24	117.20	0.9184
22	33.21	0.00	113.76	0.4523
23	29.47	0.00	131.65	0.4402
24	29.13	477.38	126.37	1.3524
25	28.06	266.46	130.81	1.3095
26	33.48	16.04	164.23	0.3609
27	23.75	13.10	120.46	0.5261
28	41.49	42.02	124.10	1.0905
29	28.88	34.76	93.01	1.5870
30	33.05	0.00	118.52	0.4493
31	29.96	310.18	123.84	1.3335
32	32.44	0.00	116.36	0.4501
33	29.34	328.25	124.87	1.3397
34	40.36	25.64	132.21	0.7190
35	28.21	21.15	98.45	1.0481
36	39.57	28.01	132.11	0.7225
37	27.67	22.89	98.53	1.0527
38	26.51	8.73	147.48	0.4646
39	25.79	5.75	151.95	0.4475
40	33.16	23.20	110.30	1.3973
41	29.51	14.34	125.95	1.3441
42	31.46	10.22	120.11	0.8202
43	31.55	27.96	117.77	0.9816
44	32.05	4.24	114.24	0.9486
45	32.41	3.99	116.63	0.8484
46	32.05	12.51	115.31	1.0133
47	30.65	24.47	120.15	0.8885

Table 5.8: BBD Results for SACI engine

Tests	η_{th} (%)	NOx (mg/kWh)	CO_2 (g/kWh)	E_{fuel} (kJ/cycle)
01	35.06	243.80	146.79	0.7095
02	29.04	234.62	92.41	1.0356
03	40.64	144.96	126.84	0.6899
04	30.03	99.53	89.42	1.0069
05	23.28	164.57	156.82	0.2189
06	29.61	333.02	125.00	0.6570
07	39.95	0.02	90.59	0.6518
08	34.27	1783.67	104.67	1.9790
09	33.67	96.25	109.62	0.9015
10	34.86	35.33	108.19	0.8727
11	33.55	99.09	108.73	0.9023
12	33.47	40.06	108.56	0.8792
13	43.20	0.02	119.66	0.3381
14	30.97	0.00	87.30	0.5064
15	39.18	1706.47	130.09	1.0429
16	29.29	1721.52	90.79	1.4863
17	30.03	18.16	128.41	0.4474
18	37.04	177.84	98.69	1.3416
19	29.73	19.89	125.76	0.4488
20	36.38	203.99	99.01	1.3488
21	35.27	47.94	103.24	0.8968
22	35.10	0.00	104.29	0.4367
23	32.11	0.00	116.39	0.4273
24	31.39	1538.44	115.56	1.3241
25	32.61	767.50	110.95	1.2872
26	34.08	68.44	155.33	0.3529
27	25.96	37.47	106.07	0.5147
28	42.22	236.94	120.25	1.0595
29	32.00	375.95	82.82	1.5448
30	35.52	0.00	106.83	0.4356
31	33.84	962.52	108.21	1.3101
32	35.04	0.00	104.40	0.4348
33	33.30	1002.83	108.51	1.3143
34	41.14	156.99	127.26	0.7028
35	31.29	119.48	87.05	1.0252
36	40.50	169.76	126.56	0.7049
37	30.82	126.25	86.77	1.0282
38	28.18	24.94	133.41	0.4526
39	28.67	17.68	131.12	0.4389
40	35.30	431.99	102.24	1.3560
41	34.53	158.87	105.31	1.3168
42	34.77	30.42	106.27	0.8007
43	35.11	116.41	103.79	0.9595
44	35.75	27.69	100.45	0.9244
45	35.85	19.22	103.18	0.8279
46	35.80	76.89	101.37	0.9879
47	33.94	63.61	106.12	0.8684

5.5.1. Optimal point of engines operation

After all this statistical analysis, the optimal point of operation for each engine was found by applying the desirability function tool available in the Statistica software to the models with all the terms. The objective was to maximize the performance of the engine by increasing thermal efficiency and reducing specific NOx and CO_2 emissions. A mesh of 11 intervals for each factor was used to identify the best combination of the investigated factors. The individual desirability and the optimal condition are shown in Figure 5.30 and Figure 5.31 for SI and SACI engines, respectively.

Desirability function works as follows:

i. Values for desired and not desired responses (thermal efficiency and specific NOx and CO_2 emissions) are defined at 1 and 0 levels, respectively, as shown at the right side of Figure 5.30 and Figure 5.31. The value for medium (0.5) level is also defined. These levels are automatically defined as 1 to maximum, 0 to minimum, and 0.5 to medium, but they can be manually adjusted according to which response is the desired one.
ii. The number of intervals is defined to plot a mesh between the levels established for each factor in order to find the responses desired among their values range.
iii. After that, the function find a point for each factor that best fits all the desired responses. This point indicates the best configuration for that factor. All the best points for each factor together define the optimal point for the engine operation.

For SI engine, the optimal operating point was 50% of H_2 in fuel blend, engine speed of 1500 rpm, fuel-air equivalence ratio of 0.3, intake pressure of 1.5 bar and -10°CA of valve overlap (Figure 5.30). For SACI engine, the optimal operating point was 36% of H_2 in fuel blend, engine speed of 2300 rpm, fuel-air equivalence ratio of 0.3, intake pressure of 1.5 bar and -10°CA of valve overlap (Figure 5.31). The choice of -10ºCA is justified by the fact that univariate analysis showed higher efficiency and lower specific NOx emissions for this level.

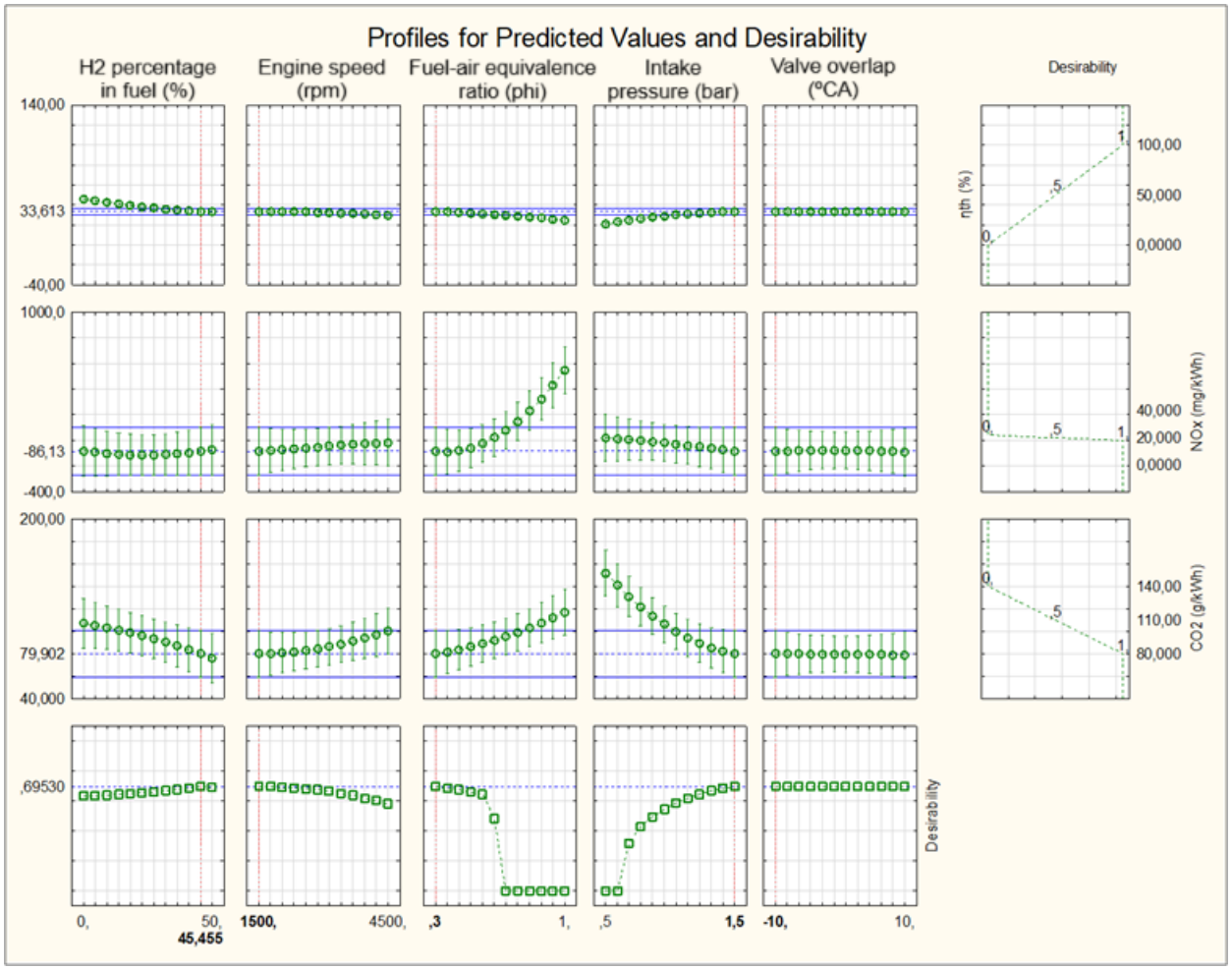

Figure 5.30: Profiles for predicted values and desirability for SI engine in BBD.

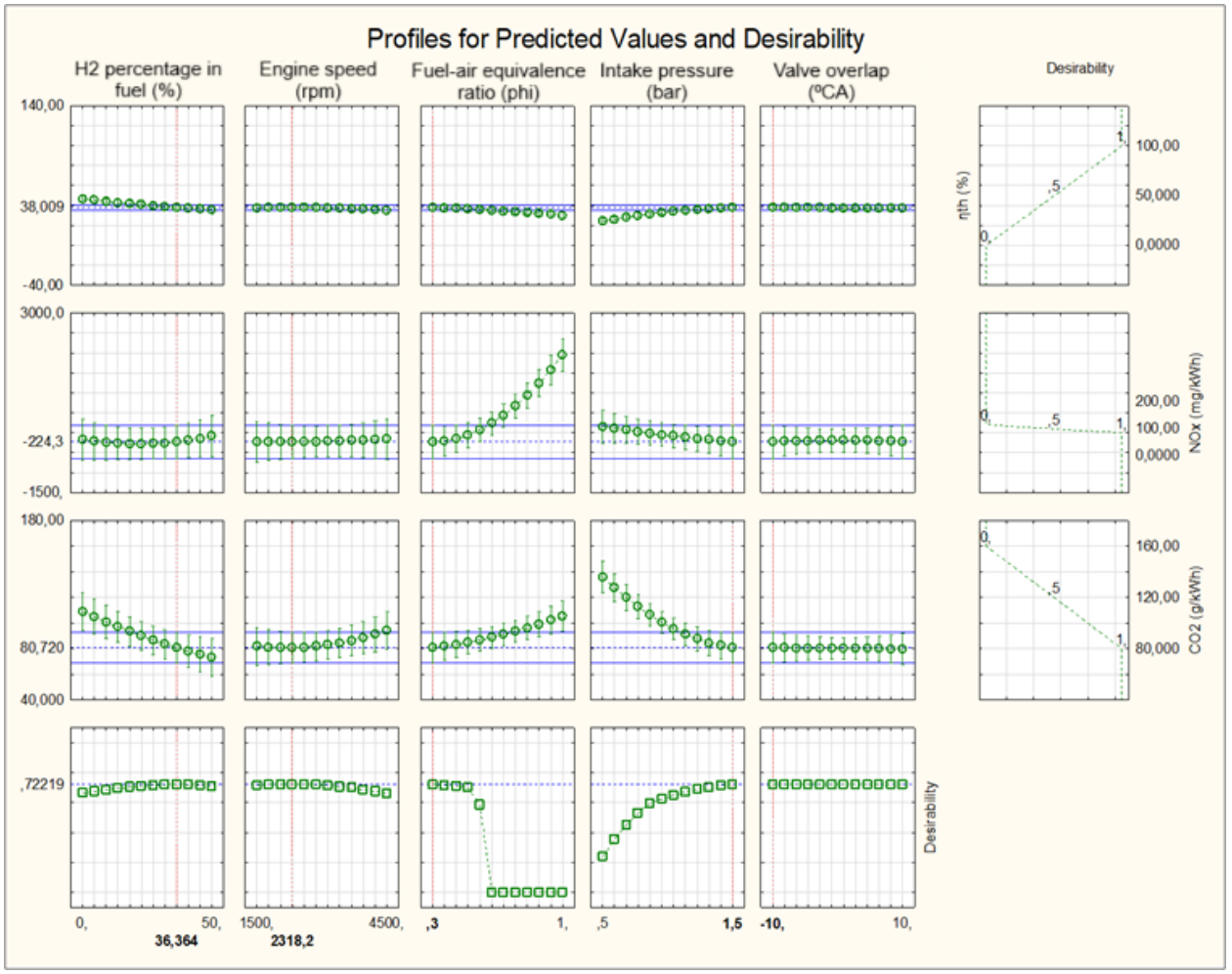

Figure 5.31: Profiles for predicted values and desirability for SACI engine in BBD.

5.5.2.Thermal Efficiency

The thermal efficiency simulation values were fitted to the quadratic equation (equation (4-4)). The complete quadratic regression models obtained were evaluated and the significant statistical coefficients identified with 95% of confidence (p-value < 0.05), Tables B.7 and B.8 at the . Appendices. After that, another model with the significant variables and interactions was generated and the following second-order polynomial regression equations were obtained:

$$Y_1^{SI} = 30.53025 - 5.77250 \cdot X_1 - 1.04472 \cdot X_1^2 - 0.78063 \cdot X_2 + 0.58320 \cdot X_2^2 - 1.15625 \cdot X_3 + 0.39945 \cdot X_3^2 + 3.27750 \cdot X_4 + 1.04028 \cdot X_4^2 - 2.71500 \cdot X_3 \cdot X_4 \quad [-] \quad R^2 = 0.97662 \tag{5-1}$$

$$Y_1^{SACI} = 32.23374 - 4.78875 \cdot X_1 + 0.89987 \cdot X_2^2 - 0.73000 \cdot X_3 + 0.46445 \cdot X_3^2 + 3.88438 \cdot X_4 + 1.19070 \cdot X_4^2 - 3.00250 \cdot X_3 \cdot X_4 \quad [-] \quad R^2 = 0.95272 \tag{5-2}$$

Figure 5.32 shows the Pareto Chart for this response: it shows the factors from most to least significant.

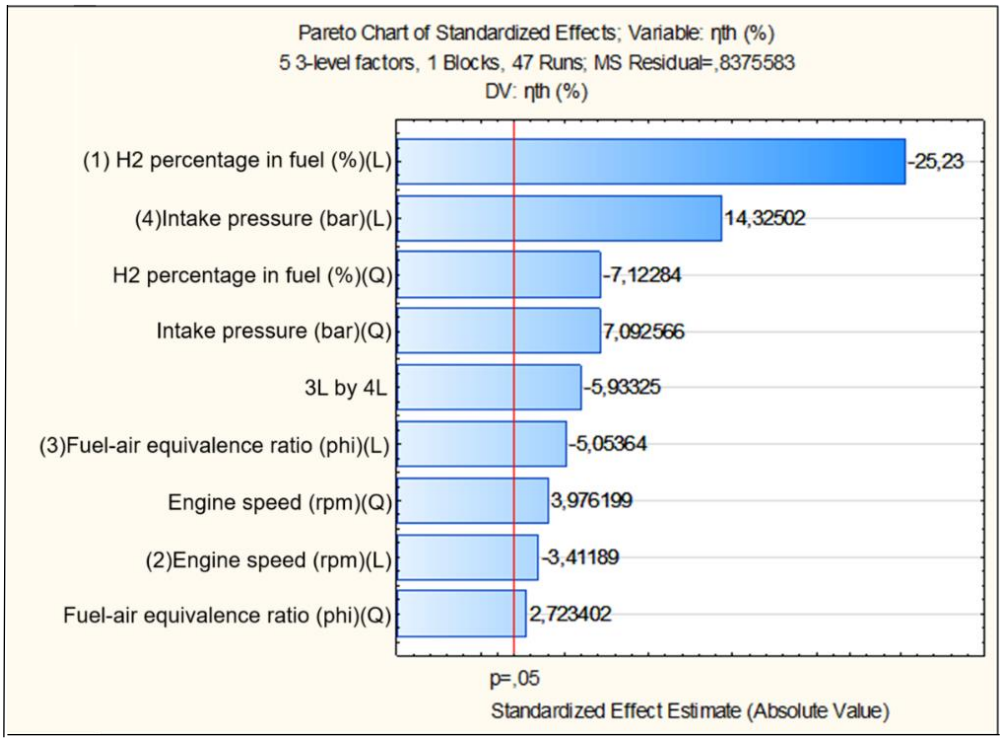

(a) SI engine

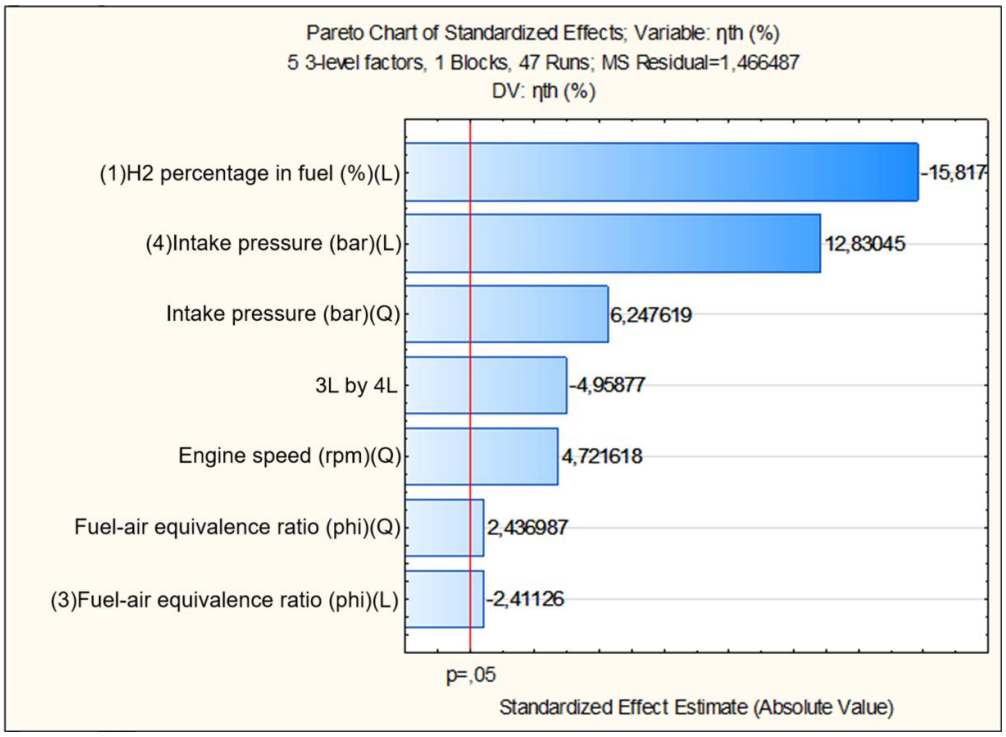

(b) SACI engine

Figure 5.32: Pareto Chart for thermal efficiency in the BBD.

It is possible to notice that all coefficients of the factors considered in the quadratic polynomial regression (equations (5-1) and (5-2)) are notable (95% of probability) to SI and SACI engine's thermal efficiency: percentage of H_2 (X_1; X_1^2), engine speed (X_2; X_2^2), fuel-air equivalence ratio (X_3; X_3^2) and intake pressure (X_4; X_4^2). The coefficient for fuel-air equivalence ratio times the intake pressure ($X_3 \cdot X_4$) is also a significant parameter. All the cited coefficients are significant for SI thermal efficiency reduced model and all except those for X_1^2 and X_2 are significant for SACI thermal efficiency reduced model.

The predicted models show negative linear (SI and SACI) and quadratic (SI) percentage of H_2 regression coefficients ($\beta_1^{SACI} = -4.78875$, $\beta_1^{SI} = -5.77250$ and $\beta_{11}^{SI} = -1.04472$), showing a negative influence in performance at high percentual of secondary fuel in blend. Thermal efficiency tends to increase with the increase of intake pressure for both engines ($\beta_4^{SACI} = +3.88438\ bar^{-1}$ and $\beta_{44}^{SACI} = +1.19070\ bar^{-1}$) similar to normal SI engines that augment efficiency with the increase in intake pressure ($\beta_4^{SI} = +3.27750\ bar^{-1}$ and $\beta_{44}^{SI} = +1.04028\ bar^{-1}$). The predicted model also shows a negative linear and positive quadratic fuel-air equivalence-ratio coefficients for both engines ($\beta_3^{SI} = -1.15625, \beta_{33}^{SI} = +0.39945, \beta_3^{SACI} = -0.73000$ and $\beta_{33}^{SACI} = +0.46445$), indicating that its variation impacts mainly negatively the thermal efficiency in SACI engines as in SI engines. The models present a positive quadratic (SI and SACI) and a negative linear (SI) engine speed regression coefficients ($\beta_{22}^{SACI} = +0.89987\ rpm^{-1}$, $\beta_2^{SI} = -0.78063\ rpm^{-1}$ and $\beta_{22}^{SI} = +0.58320\ rpm^{-1}$), showing that SACI engine is positively affected by the increase in engine speed and SI engine is mostly negatively affected. by the increase in engine speed. The models also present a negative coefficient of the interaction between intake pressure and fuel-air equivalence ratio for both engines ($\beta_{34}^{SI} = -2.71500\ bar^{-1}$ and $\beta_{34}^{SACI} = -3.00250\ bar^{-1}$).

Figure 5.33 shows the thermal efficiency residues distribution.

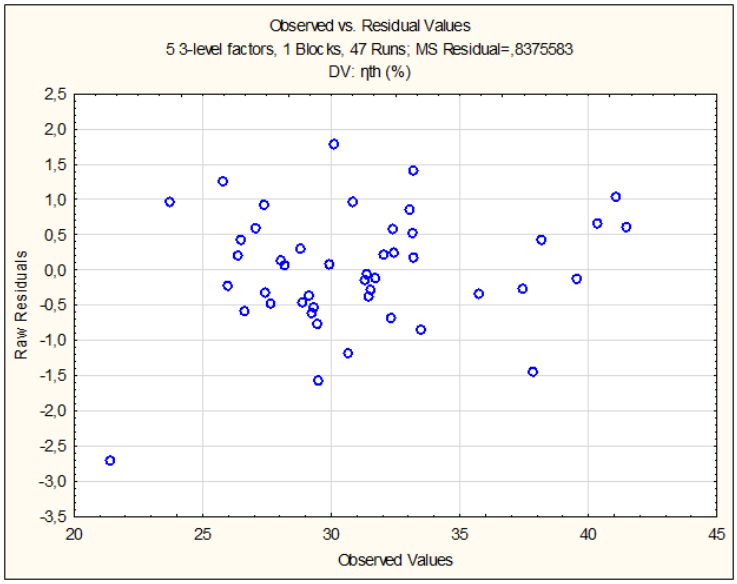

(a) SI engine

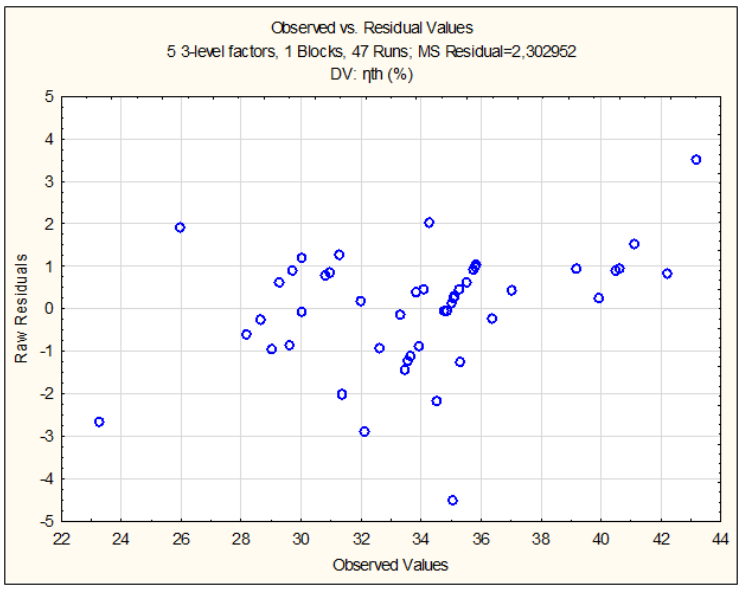

(b) SACI engine

Figure 5.33: Thermal efficiency observed x residuals values in the BBD ($R^2_{SI} = 0.97662\ and\ R^2_{SACI} = 0.95272$).

The residues are uniformly distributed around the average value of zero, as an expression of the robustness of the model. The highest residual in thermal efficiency for SACI engine was of less than 5%. For the SACI engine, thermal efficiency prediction has a R^2 of 95.27%. After that, surface responses were generated for two factors interactions. The other three factors were kept constant at medium values.

Figure 5.34 shows the influence of interaction between intake pressure and percentage of H_2 over thermal efficiency.

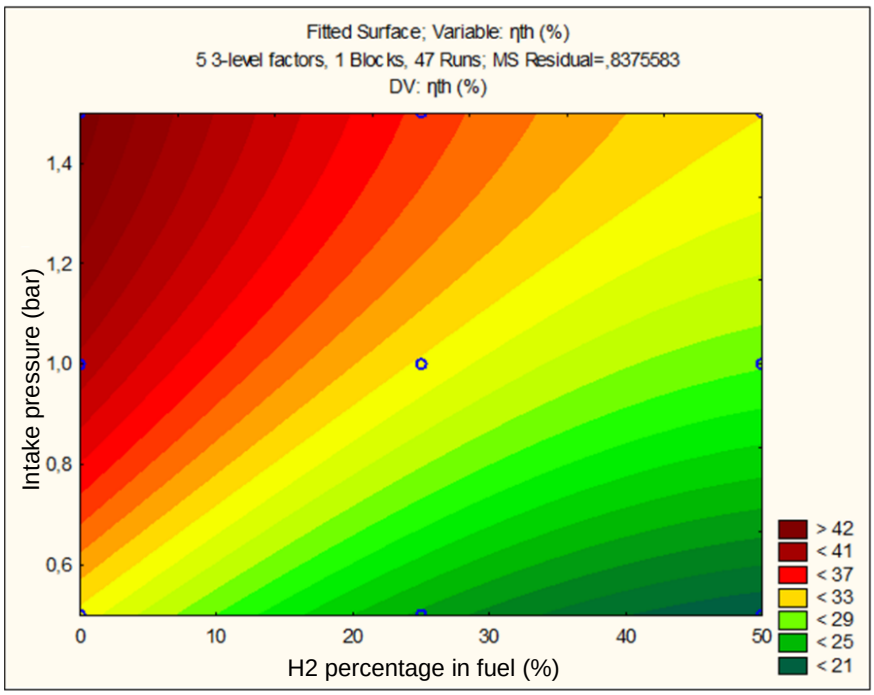

(a) SI engine

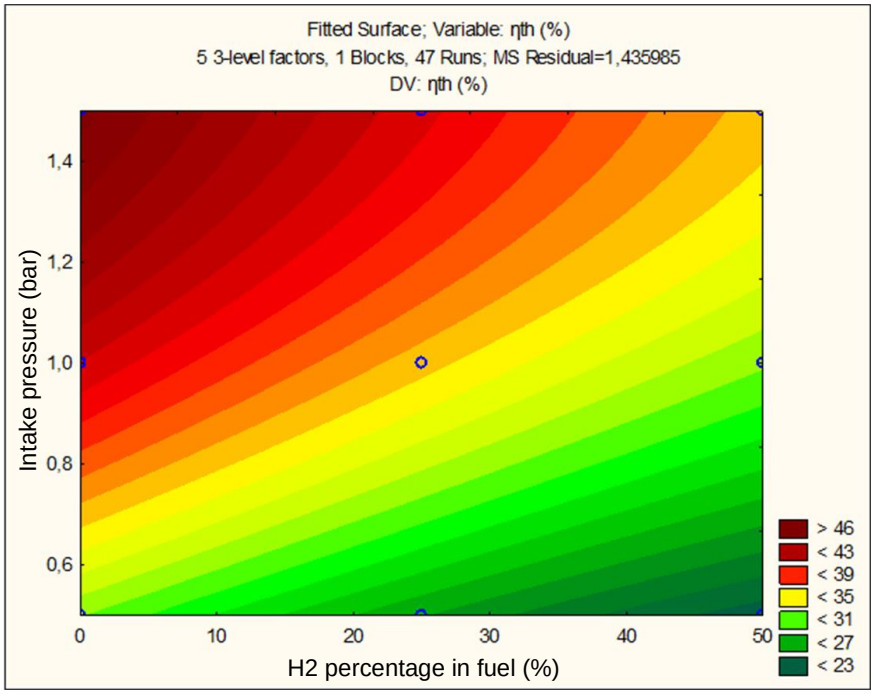

(b) SACI engine

Figure 5.34: Fitted surface for intake pressure and percentage of H_2 over thermal efficiency in BBD, remaining constant at medium value the factors ϕ, P_{IV} and valve overlap.

Figure 5.35 shows the influence of interaction between intake pressure and fuel-air equivalence ratio.

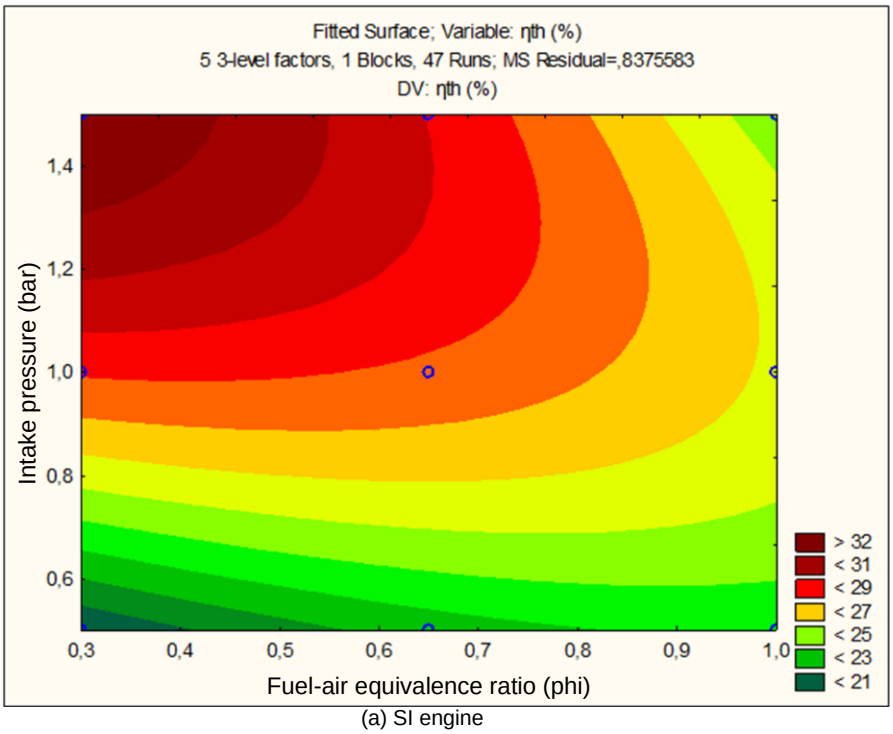

(a) SI engine

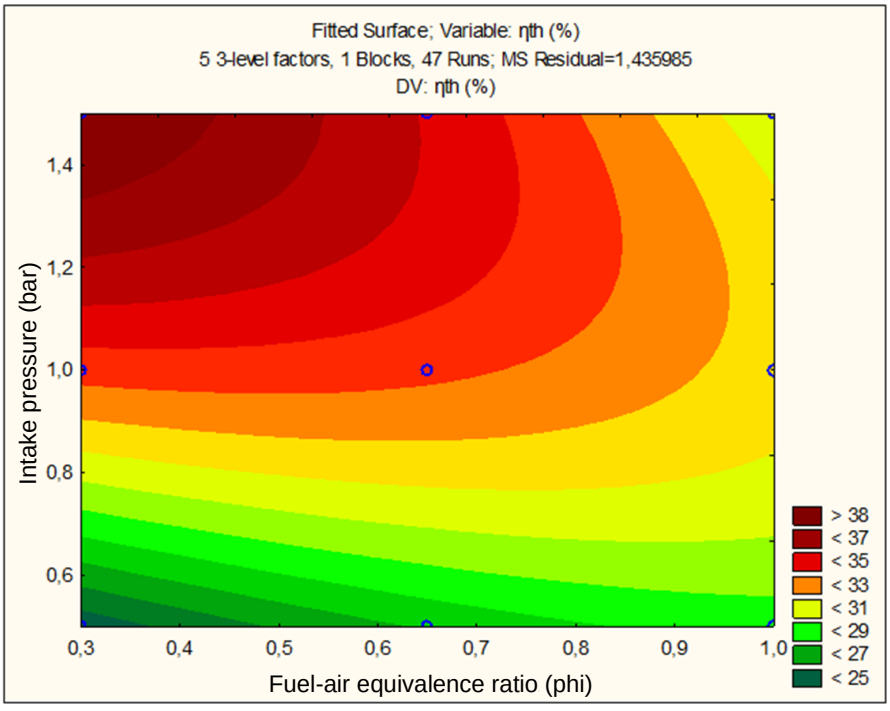

(b) SACI engine

Figure 5.35: Fitted surface for intake pressure and fuel-air equivalence ratio over thermal efficiency in BBD, remaining constant at medium value the factors $\%H_2, RPM$ and valve overlap.

From Figure 5.34 and Figure 5.35, it is notable that SACI engine performs better presenting higher thermal efficiencies for smaller percentages of H_2 and smaller fuel-air equivalence ratios with higher intake pressures. Increasing the percentage of H_2, maximum pressure decreases. A reduction of the cycle pressure leads to smaller indicated work, causing a reduction of the thermal efficiency. Decreasing fuel-air equivalence ratio reduces the amount of injected fuel energy, that leads to thermal efficiency reduction. Since SI engines operate in fuel-air equivalence ratios around 1, forcing it to work under very lean mixtures operationally and commercially unfeasible. So, evaluating regions under the same intake pressure, but with lean mixtures to SACI engines and roughly stoichiometric mixtures to SI engines for both optimal operation, SACI engine shows to be significantly more efficient than SI engine. Furthermore, SACI combustion allow the engine to operate with higher percentage of H_2 keeping thermal efficiency at best levels.

5.5.3. Specific NOx emission

The specific NOx emission reduced models with the significant statistical coefficients were generated and showed in equations (5-3) and (5-4).

$$Y_2^{SI} = 152.1699 - 19.7067 \cdot X_1^2 + 197.3794 \cdot X_3 - 92.4475 \cdot X_3^2 + 25.3231 \cdot X_4 - 52.7300 \cdot X_2 \cdot X_3 + 78.5375 \cdot X_3 \cdot X_4 \quad [mg/kWh] \quad R^2 = 0.9334 \tag{5-3}$$

$$Y_2^{SACI} = 509.847 - 72.762 \cdot X_1^2 - 87.825 \cdot X_2 + 603.210 \cdot X_3 - 261.861 \cdot X_3^2 + 167.819 \cdot X_4 - 192.735 \cdot X_2 \cdot X_3 + 403.800 \cdot X_3 \cdot X_4 \quad [mg/kWh] \quad R^2 = 0.93519 \tag{5-4}$$

The specific NOx emissions Pareto Chart, Figure 5.36, indicates the significance of the same four factors.

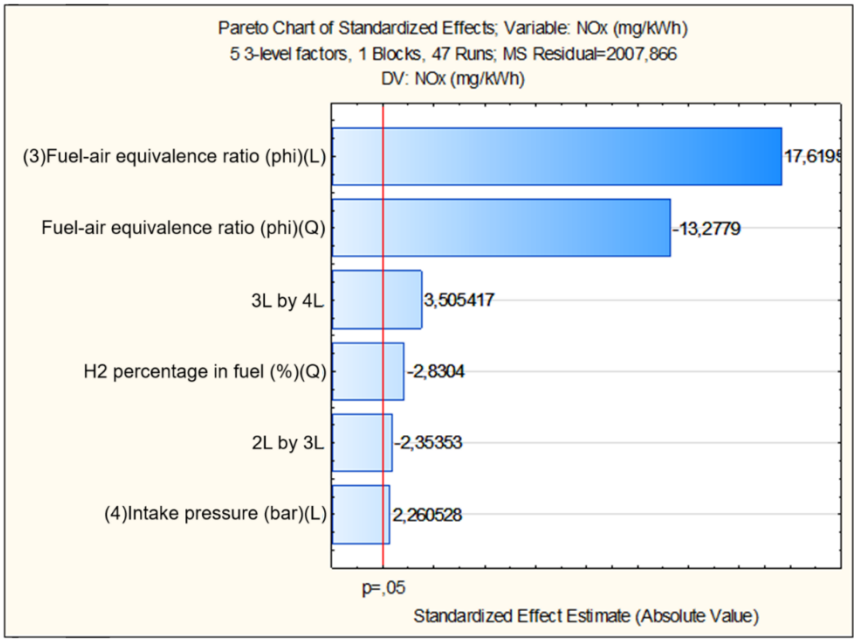

(a) SI engine

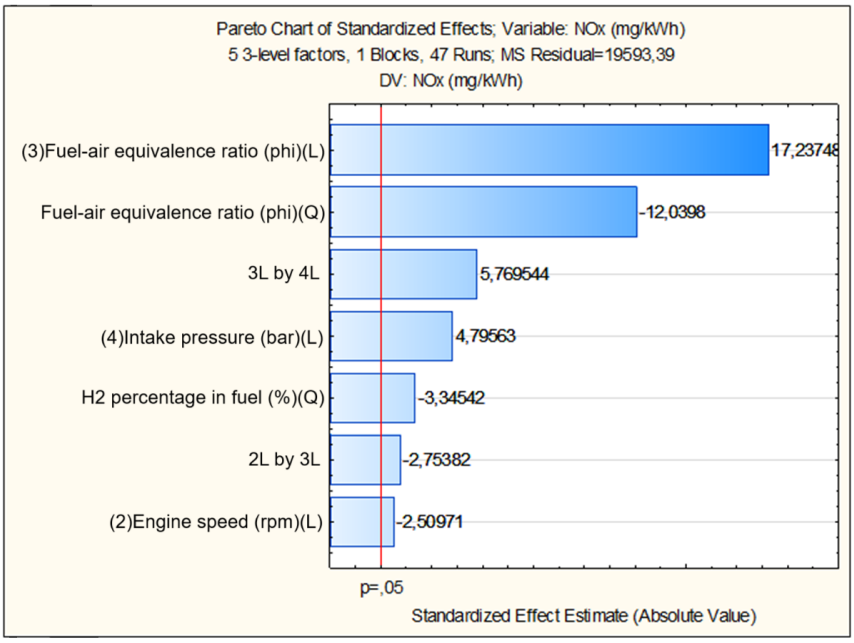

(b) SACI engine

Figure 5.36: Pareto Chart for specific NOx emission in the BBD.

All coefficients of the factors considered for the reduced models ($X_1^2;\ X_2;\ X_3; X_3^2; X_4$) are relevant (95% of probability) to SI and SACI engine's NOx emissions (equations (5-3) and (5-4)). The coefficients for engine speed times fuel-air equivalence ratio ($X_2 \cdot X_3$) and fuel-air equivalence ratio times the intake pressure ($X_3 \cdot X_4$) are also significant parameters. All the cited coefficients are significant for SACI specific NOx emissions reduced model and all except that for X_2 are significant for SI specific NOx emissions reduced model.

The predicted model for SACI engines shows a positive linear coefficient ($\beta_3^{SACI} = +603.210$) and a negative quadratic coefficient ($\beta_{33}^{SACI} = -261.861$) to fuel-air equivalence ratio, presenting a tendency to increase NOx emissions at high ratios. Same tendency presented at SI engine model ($\beta_3^{SI} = +197.3794\ and\ \beta_{33}^{SI} = -92.4475$). Increasing fuel-air equivalence ratio increases the average cycle temperature and high temperatures favor the formation of NOx. SACI engine's NOx emission tends to increase with the increase of intake pressure ($\beta_4^{SACI} = +167.819\ bar^{-1}$), similar to normal SI engines that augment emission with more fuel injected ($\beta_4^{SI} = +25.3231\ bar^{-1}$). NOx emission models present a tendency to decrease with the increase of H_2 percentage in fuel ($\beta_{11}^{SACI} = -72.762\ and\ \beta_{11}^{SI} = -19.7067$) . SACI engine model also presents a tendency to decrease NOx emissions increasing engine speed, showing a negative linear regression coefficient ($\beta_2^{SACI} = -87.825\ rpm^{-1}$). Lastly, the prediction models show a tendency to increase NOx emissions with the interaction between fuel-air equivalence ratio and intake pressure ($\beta_{34}^{SACI} = +403.800\ bar^{-1}\ and\ \beta_{34}^{SI} = +78.5375\ bar^{-1}$) and to decrease NOx emissions with the interaction between engine speed and fuel-air equivalence ratio ($\beta_{23}^{SACI} = -192.735\ rpm^{-1}\ and\ \beta_{23}^{SI} = -52.7300\ rpm^{-1}$).

Figure 5.37 shows the specific NOx emission residues distribution.

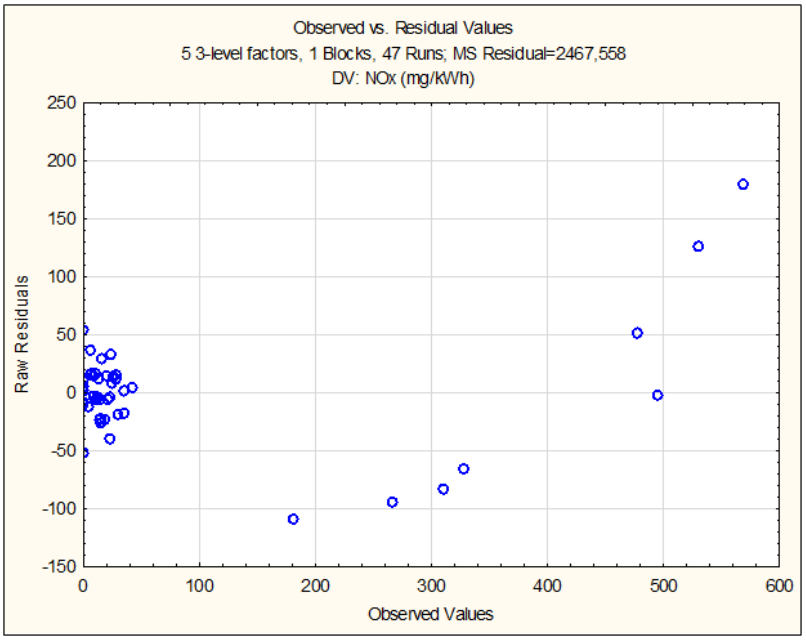

(a) SI engine

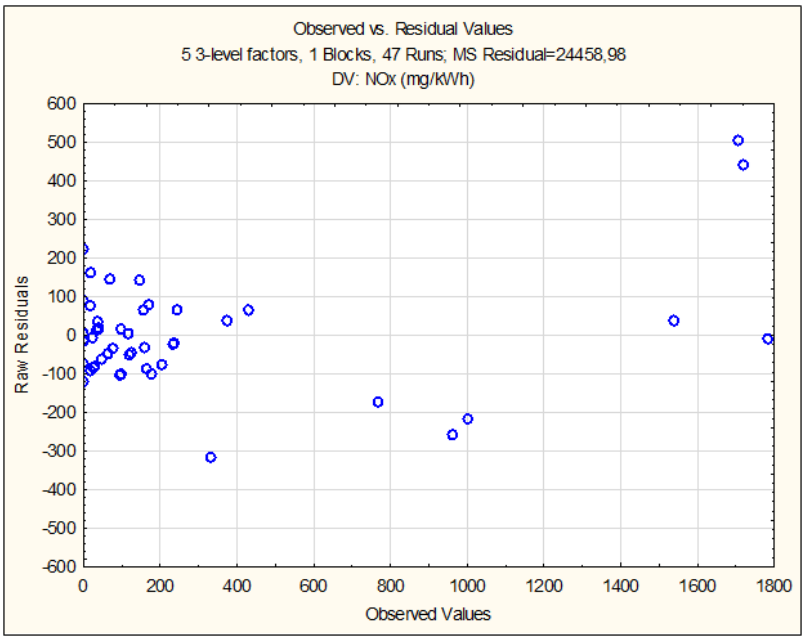

(b) SACI engine

Figure 5.37: Specific NOx emission observed x residuals values in the BBD model ($R^2_{SI} = 0.9334\ and\ R^2_{SACI} = 0.93519$).

The residues are considerably well distributed around the average value of zero, as an expression of the robustness of the model. For the SACI engine, specific NOx emission prediction has a R^2 of 93.52%.

Figure 5.38 shows the influence of interaction between fuel-air equivalence ratio and percentage of H_2 specific NOx emission.

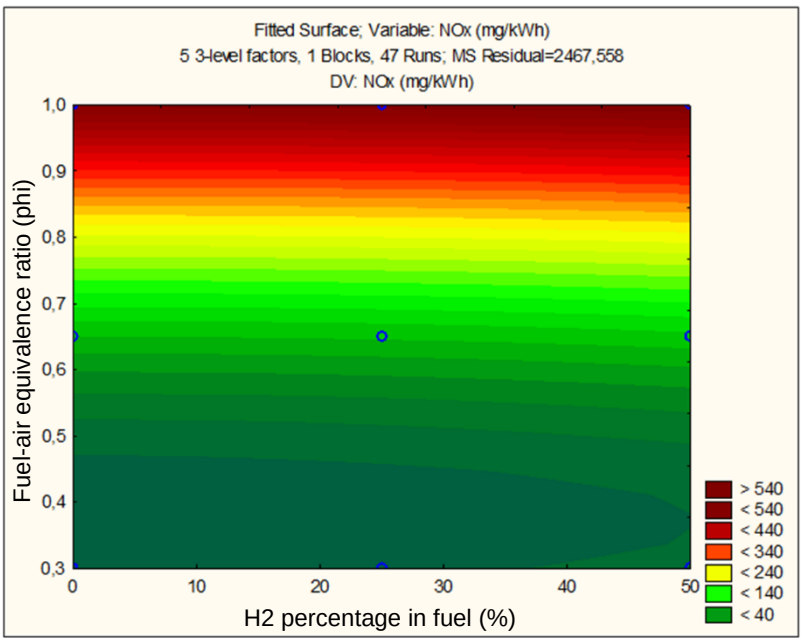

(a) SI engine

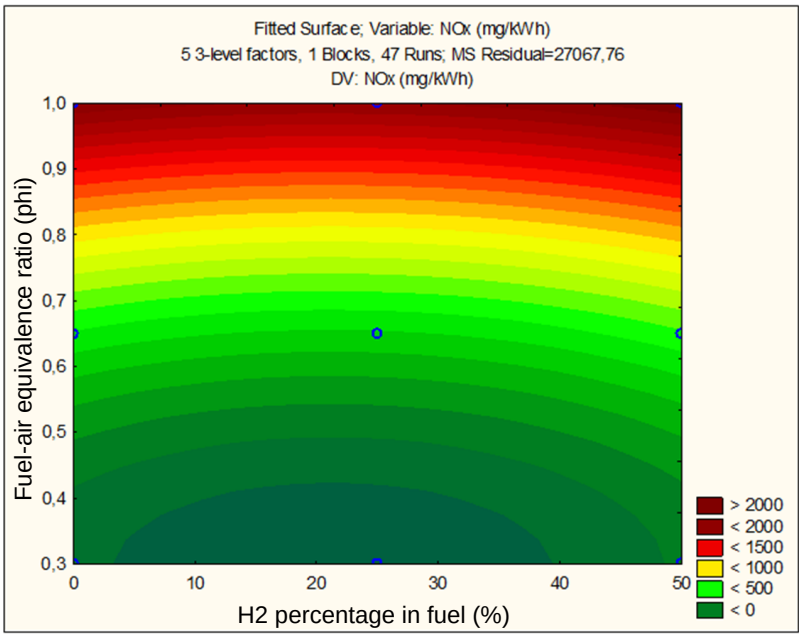

(b) SACI engine

Figure 5.38: Fitted surface for fuel-air equivalence ratio and percentage of H_2 over specific NOx emission in BBD, remaining constant at medium value the factors RPM, P_{IV} and valve overlap.

Figure 5.39 shows the influence of interaction between intake pressure and fuel-air equivalence ratio over specific NOx emission.

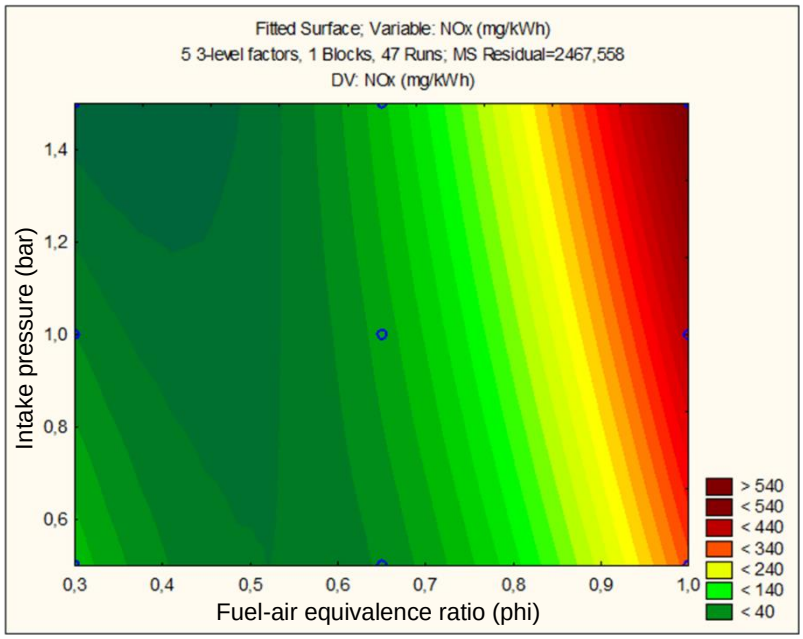

(a) SI engine

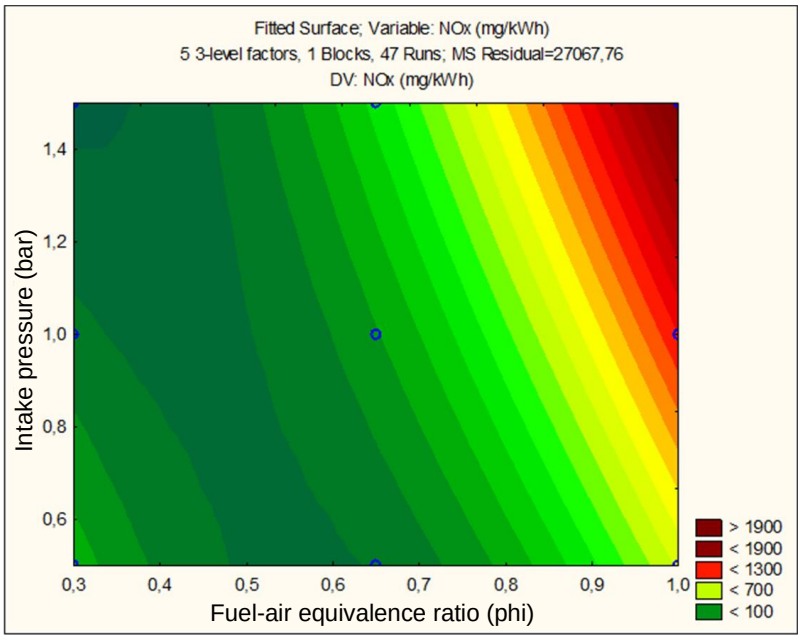

(b) SACI engine

Figure 5.39: Fitted surface for intake pressure and fuel-air equivalence ratio over specific NOx emission in BBD, remaining constant at medium value the factors $\%H_2, RPM$ and valve overlap.

Figure 5.38 and Figure 5.39 confirm the high significance of fuel-air equivalence ratio linear coefficient of reduced models. Compared to its significance, percentage of H_2 and intake pressure influences much less. At the same ratios, SACI engine shows to emit more NOx than SI engines. It probably happens due to the change of combustion during the cycle, which makes the burned fraction to increase rapidly in HCCI combustion blocking a more homogeneous burning. On the other hand, when the fuel-air equivalence ratio is lower than 0.5 with higher intake pressure, the NOx formation of both engines tends to be null. This results show that NOx emissions tend to achieve the concentration magnitude, but not precisely. This inaccuracy could be explained by the fact that NOx emissions in lean and very lean mixtures are low. So, the polynomial model achieve the order of magnitude, but not accurately (LEITE; PRADELLE; LEAL, 2021).

5.5.4.Specific CO_2 emission

The specific CO_2 emission reduced models with the significant statistical coefficients were generated and showed in equations (5-5) and (5-6).

$$Y_3^{SI} = 131.7325 - 17.6944 \cdot X_1 + 3.6963 \cdot X_2 - 2.6968 \cdot X_2^2 - 2.7655 \cdot X_3^2 - 19.0438 \cdot X_4 - 6.7734 \cdot X_4^2 + 15.6225 \cdot X_3 \cdot X_4 \quad [g/kWh] \quad R^2 = 0.93983 \tag{5-5}$$

$$Y_3^{SACI} = 115.4367 - 20.6344 \cdot X_1 - 2.3363 \cdot X_2^2 - 16.1463 \cdot X_4 - 4.6559 \cdot X_4^2 + 11.4750 \cdot X_3 \cdot X_4 \quad [g/kWh] \quad R^2 = 0.95603 \tag{5-6}$$

The specific CO_2 emissions Pareto Chart, Figure 5.40, indicates the significance of the same four factors.

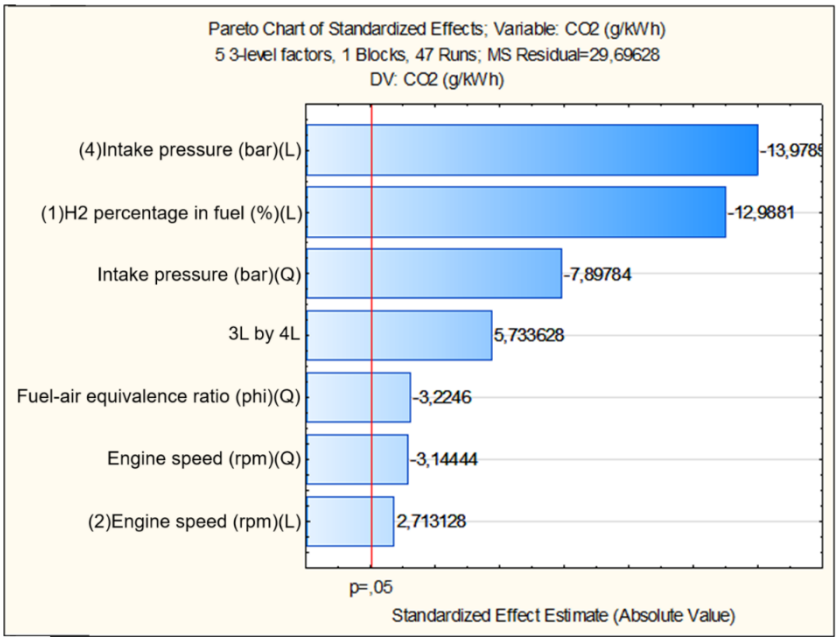

(a) SI engine

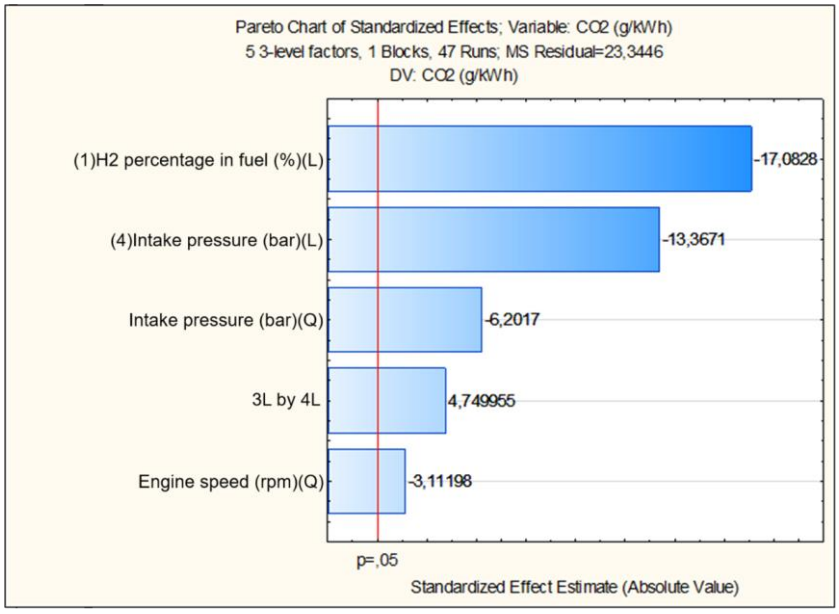

(b) SACI engine

Figure 5.40: Pareto Chart for specific CO_2 emission in the BBD.

All coefficients of the factors considered for the reduced models ($X_1;\ X_2; X_2^2; X_3^2; X_4;\ X_4^2$) are relevant (95% of probability) to SI and SACI engine's CO_2 emissions (equations (5-5) and (5-6)). The coefficient for fuel-air equivalence ratio times the intake pressure ($X_3 \cdot X_4$) is also a significant parameter. All the cited

coefficients are significant for SI specific CO_2 emissions reduced model and all except that for X_2 are significant for SACI specific CO_2 emissions reduced model.

CO_2 emission regression models show negative linear coefficients for percentage of H_2 ($\beta_1^{SACI} = -20.6344\ and\ \beta_1^{SI} = -20.6344$), tending to decrease CO_2 emissions at high percentual of secondary fuel in blend due to the less amount of carbon atoms in fuel . CO_2 emission regression models present negative linear and quadratic coefficients for intake pressure ($\beta_4^{SACI} = -16.1463\ bar^{-1}, \beta_{44}^{SACI} = -4.6559\ bar^{-2}, \beta_4^{SI} = -19.0438\ bar^{-1}\ and\ \beta_{44}^{SI} = -6.7734\ bar^{-2}$), tending to decrease CO_2 emissions at high intake pressures. CO_2 emission regression models reveal positive linear (SI) and negative quadratic (SACI and SI) coefficients for engine speed ($\beta_{22}^{SACI} = -2.3363\ rpm^{-2}, \beta_2^{SI} = +3.6963\ rpm^{-1}\ and\ \beta_{22}^{SI} = -2.6968\ rpm^{-2}$), tending to decrease CO_2 emissions at high speeds. CO_2 emission regression models tend to increase with the increase of interaction between fuel-air equivalence ratio and intake pressure ($\beta_{34}^{SACI} = +11.4750\ bar^{-1}\ and\ \beta_{34}^{SI} = +15.6225\ bar^{-1}$). CO_2 emission regression model for SI engine also present a negative quadratic coefficient for fuel-air equivalence ratio ($\beta_3^{SI} = -2.7655$), showing a tendency to decrease CO_2 emissions with the enrichment of the fuel-air mixture.

Figure 5.41 brings the specific CO_2 emission residues distribution.

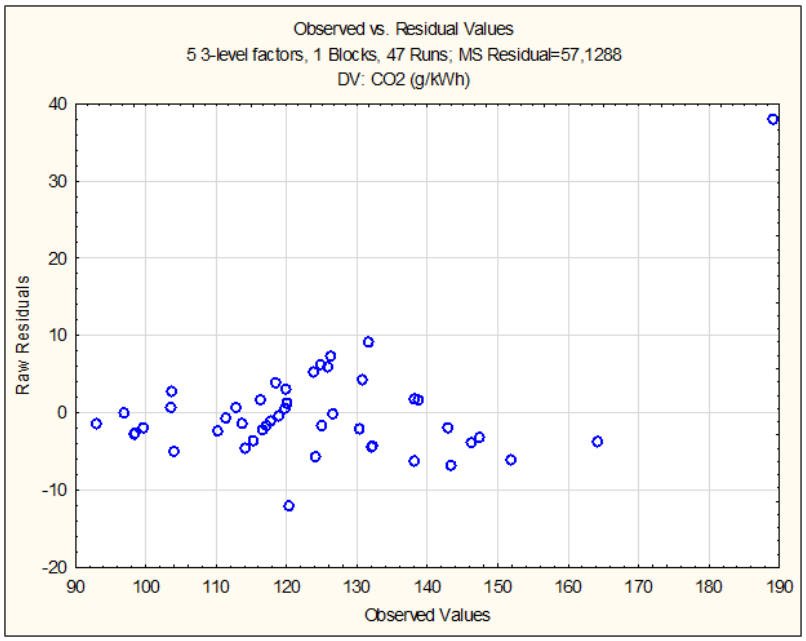

(a) SI engine

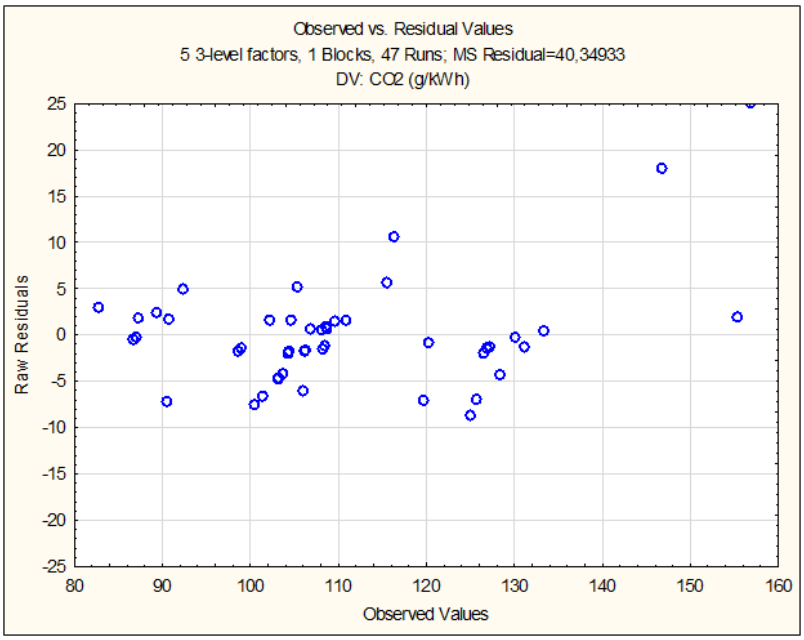

(b) SACI engine

Figure 5.41: Specific CO_2 emission observed x residuals values in the BBD model ($R^2_{SI} = 0.93983\ and\ R^2_{SACI} = 0.95603$).

The residues are consistently well distributed around the average value of zero, as an expression of the robustness of the model. For the SACI engine, specific CO_2 emission prediction has a R^2 of 95.60%.

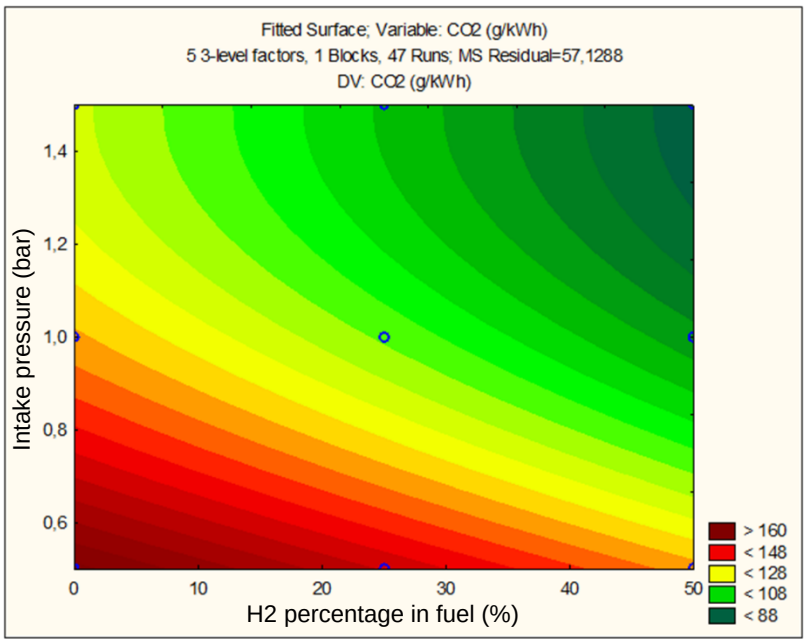

(a) P_{IV} x $\%H_2$

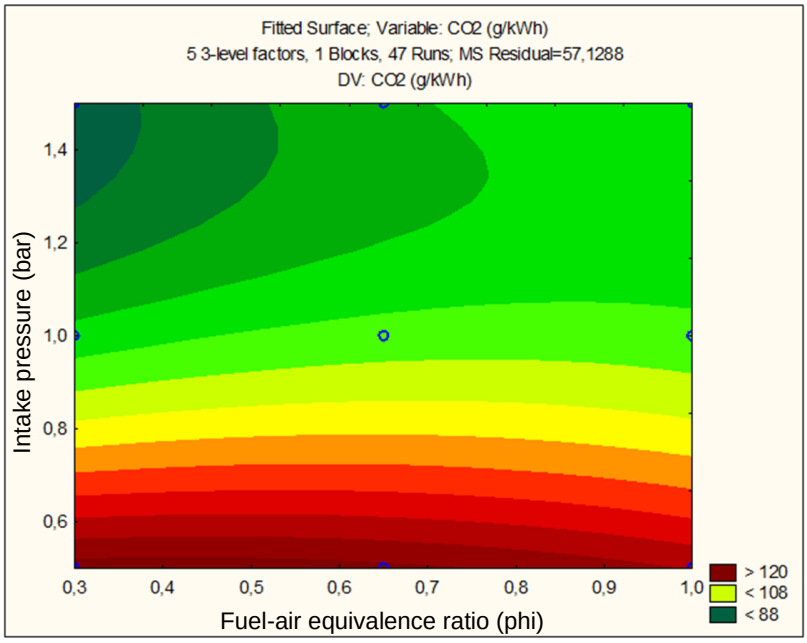

(b) P_{IV} x ϕ

Figure 5.42: Fitted surface for intake pressure times percentage of H_2 and fuel-air equivalence ratio over specific CO_2 emission for SI engine in BBD, remaining constant at medium value the factors RPM, ϕ and valve overlap in Figure 5.42(a); and $\%H_2, RPM$ and valve overlap in Figure 5.42(b).

Figure 5.42 (a) indicates that the higher percentage of H_2 and intake pressure, smaller the CO_2 emissions. Keeping the intake pressure high, satisfactory CO_2 emissions could also be attained at lower percentage of H_2 in fuel blend. But as much as increased are intake pressure and percentage of H_2,

smallest are the CO_2 emissions due to higher amount of secondary fuel in blend and also being admitted to the cylinder by the greater pressure. Figure 5.42 (b) shows that lower the fuel-air equivalence ratio and higher the intake pressure, lower the CO_2 emissions. Poor fuel-air mixtures have more free oxygen to allow the complete oxidation of fuel and increase the CO_2 formation, but increasing the intake pressure CO_2 emissions are diminished.

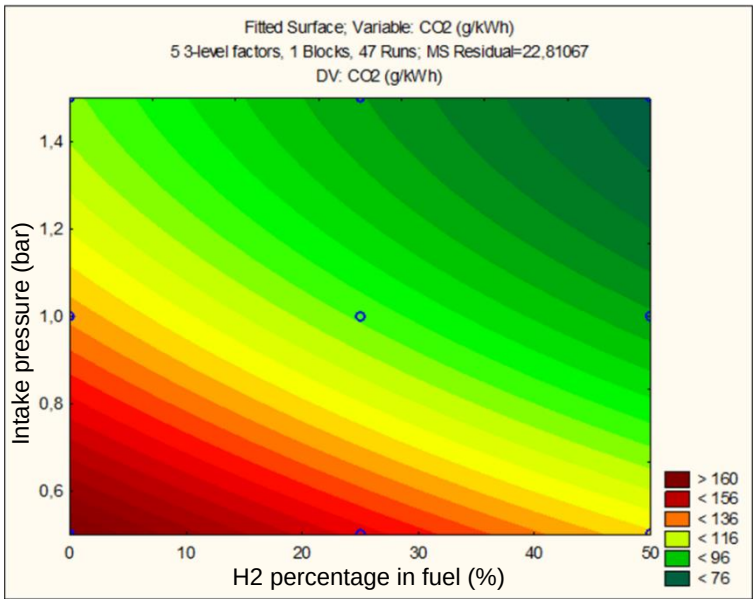

(a) P_{IV} x $\%H_2$

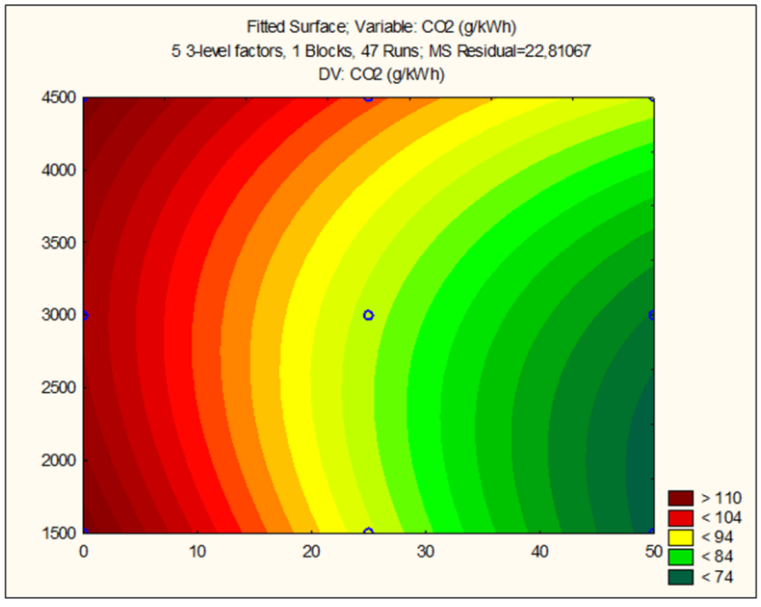

(b) RPM x $\%H_2$

Figure 5.43: Fitted surface for intake pressure and fuel-air equivalence ratio over specific CO_2 emission for SACI engine in BBD, remaining constant at medium value the factors RPM, ϕ and valve overlap in Figure 5.43(a); and ϕ, P_{IV} and valve overlap in Figure 5.43(b).

Figure 5.43 (a) shows the same behavior for SACI engine with interaction between intake pressure and percentage of H_2 in SI engine. Therefore, increasing intake pressure and percentage of H_2, CO_2 emissions decreases due to higher amount of secondary fuel in blend and also being admitted to the cylinder by the enlarged load. Figure 5.43 (b) indicates that higher the percentage of H_2 and lower the engine speed, lower are the CO_2 emissions for the SACI engine. That can be explained similarly. Increasing percentage of H_2 imply in less carbon atoms to form CO_2 and small engine speeds allow more mixing time, resulting in a better homogeneity of the mixture.

5.5.5. Injected Fuel energy

The injected fuel energy is calculated based on fuel mass present inside the cylinder right at the intake valve closing and the lower heating value (LHV) of the fuel used.

The injected fuel energy reduced models with the significant statistical coefficients were generated and showed in equations (5-7) and (5-8).

$$\begin{aligned} Y_4^{SI} = {} & 0.880976 + 0.162581 \cdot X_1 + 0.014780 \cdot X_1^2 - 0.015131 \\ & \cdot X_2 + 0.440063 \cdot X_3 + 0.011051 \cdot X_3^2 \\ & + 0.454538 \cdot X_4 + 0.068925 \cdot X_1 \cdot X_3 \\ & + 0.082825 \cdot X_1 \cdot X_4 + 0.227425 \cdot X_3 \\ & \cdot X_4 \quad [kJ/cycle] \qquad R^2 = 0.99562 \end{aligned} \tag{5-7}$$

$$\begin{aligned} Y_4^{SACI} = {} & 0.876545 + 0.159225 \cdot X_1 + 0.434456 \cdot X_3 + 0.441694 \cdot X_4 \\ & + 0.080875 \cdot X_1 \cdot X_4 \ [kJ/cycle] \ R^2 = 0.99569 \end{aligned} \tag{5-8}$$

The injected fuel energy Pareto Chart (Figure 5.44) indicates the significance of the same four factors.

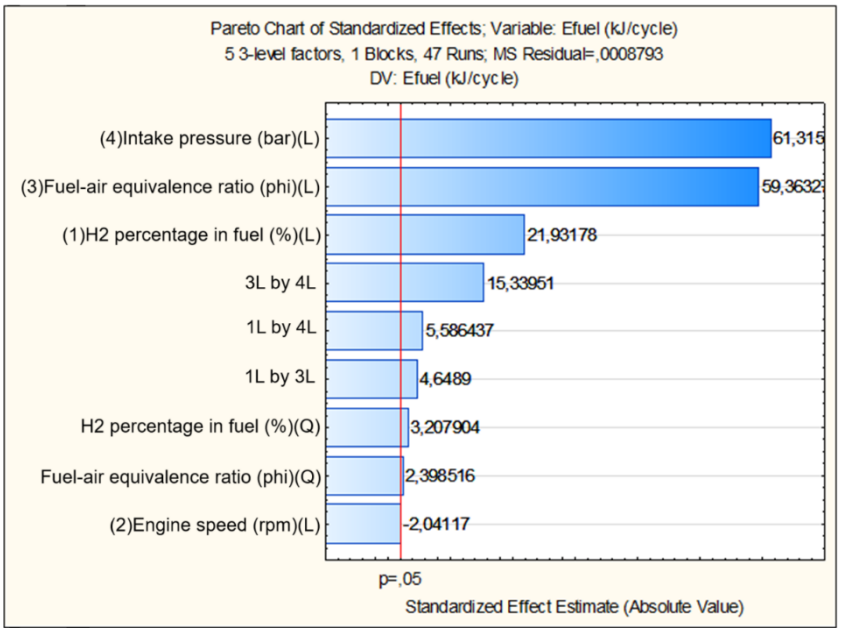

(a) SI engine

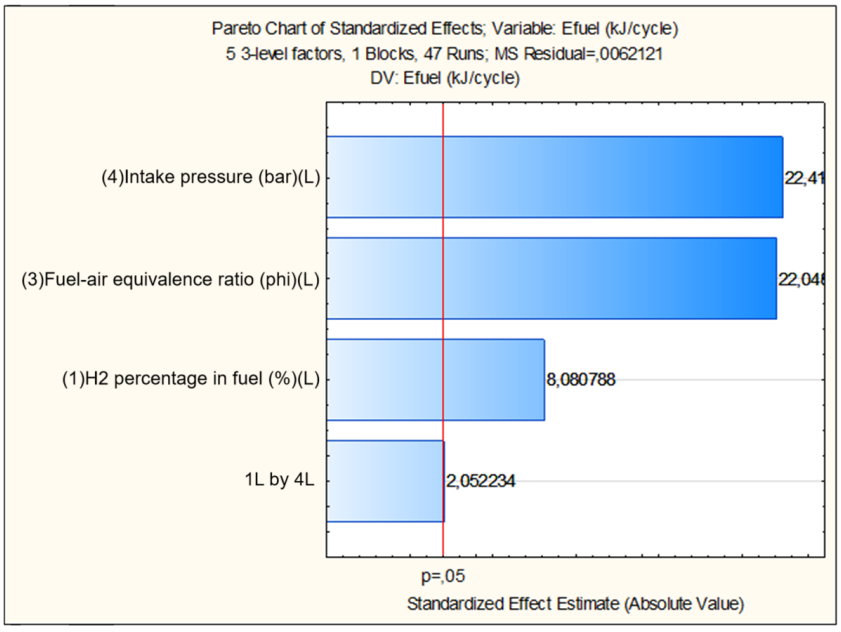

(b) SACI engine

Figure 5.44: Pareto Chart for injected fuel energy in the BBD.

All coefficients of the factors considered for the reduced models ($X_1; X_1^2;\ X_2; X_3; X_3^2; X_4$) are relevant (95% of probability) to SI and SACI engine's fuel energy (equations (5-7) and (5-8)). The coefficients for percentage of H_2 times the fuel-air equivalence ratio ($X_1 \cdot X_3$) and times the intake pressure ($X_1 \cdot X_4$), and

the fuel-air equivalence ratio times the intake pressure ($X_3 \cdot X_4$) are also significant parameters. All the cited coefficients are significant for SI fuel energy reduced model and those for $X_1; X_3; X_4$; factors and $X_1 \cdot X_4$ factors interaction are significant for SACI fuel energy reduced model.

The regression coefficient that most influence the increase in injected fuel energy is the linear coefficient for intake pressure ($\beta_4^{SACI} = +0.441694\ bar^{-1}\ and\ \beta_4^{SI} = +0.454538\ bar^{-1}$), showing a tendency to increase fuel energy available for the engine by increasing the fuel mass in each cycle. The fuel-air equivalence ratio having a positive influence on the energy of the injected fuel through the linear coefficient ($\beta_3^{SACI} = +0.434456\ and\ \beta_3^{SI} = +0.440063$) and quadratic coefficient ($\beta_{33}^{SI} = +0.011051$) confirms the trend that enrichment of the fuel-air mixture makes more energy available in the cycle. The percentage of H_2 in fuel present a positive influence on the energy of the injected fuel through the linear coefficient ($\beta_1^{SACI} = +0.159225\ and\ \beta_1^{SI} = +0.162581$) and quadratic coefficient ($\beta_{11}^{SI} = +0.014780$) endorse the trend that higher the amount of H_2 in fuel blend higher the LHV of fuel. The injected fuel energy model for SI engine also presents a negative linear coefficient for engine speed ($\beta_2^{SI} = -0.015131\ rpm^{-1}$), indicating that increasing engine speed the injected fuel energy decreases. Besides, both prediction models showed to suffer positive influence of some interaction coefficients, such as: fuel-air equivalence ratio with intake pressure for SI engine ($\beta_{34}^{SI} = +0.227425\ bar^{-1}$), percentage of H_2 with intake pressure for both engines ($\beta_{14}^{SACI} = +0.080875\ bar^{-1}\ and\ \beta_{14}^{SI} = +0.082825\ bar^{-1}$) and percentage of H_2 with fuel-air equivalence ratio for SI engine ($\beta_{13}^{SI} = +0.068925$). The predicted models presents mostly positive coefficients for both engines, showing a synergistic effect. The only exception is engine speed for SI engine, but it is on the limit of being a non-significant parameter.

Figure 5.45 shows the residues distribution. The fuel energy prediction models were the best quadratic fit between the responses, with a R^2 of 99.57% for SACI engine.

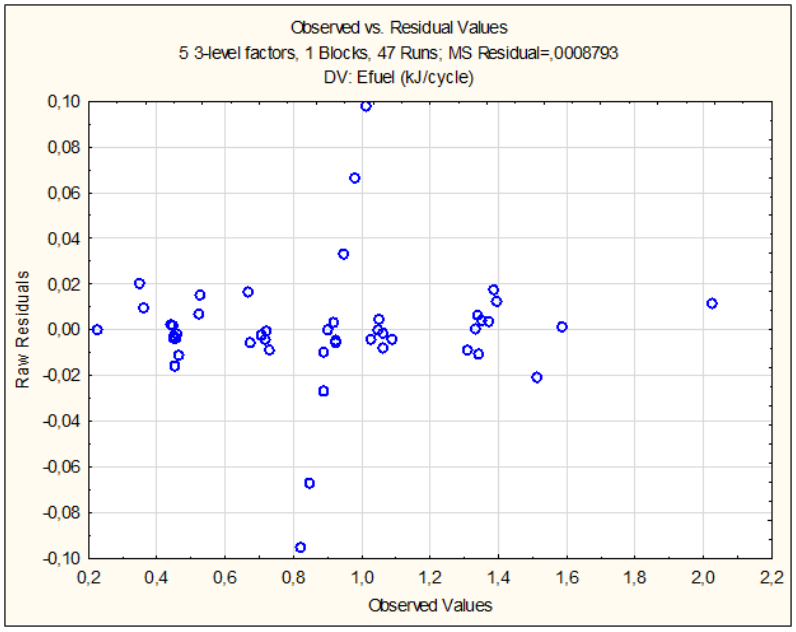

(a) SI engine

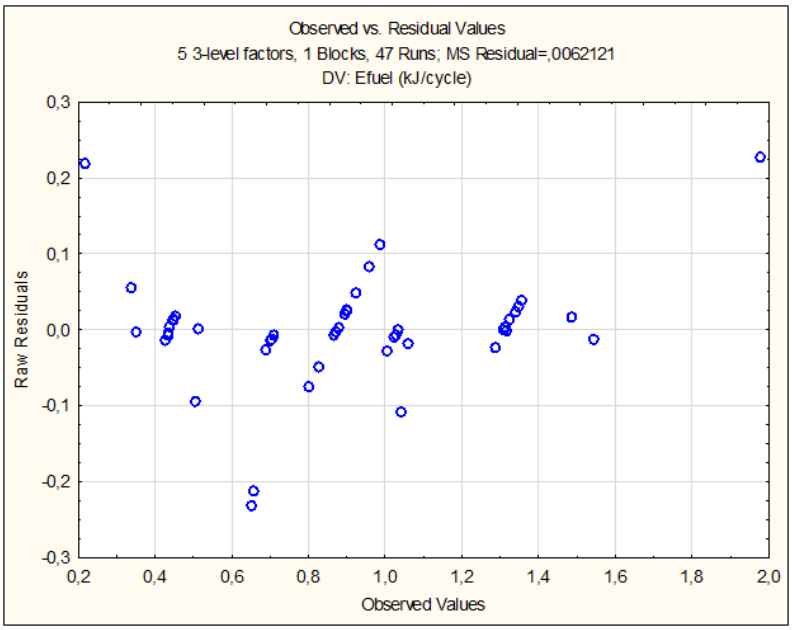

(b) SACI engine

Figure 5.45: Fuel energy observed x residuals values in the BBD model ($R^2_{SI} = 0.99562\ and\ R^2_{SACI} = 0.99569$).

5.5.6. Partial Conclusion

The summary of the most significant factors for each response is displayed in Table 5.9. This overview indicates that, to SACI engine, the percentage of H_2, fuel-air equivalence ratio and intake pressure are important factors to all performance parameters. Additionally, the engine speed is significant in three of the four responses (thermal efficiency, specific NOx emission, and specific CO_2 emission). On the other hand, the valve overlap, under the investigated conditions, did not show a significant impact in any response. Furthermore, SACI model indicates that fuel-air equivalence ratio and intake pressure interaction is significant to the performance parameters; engine speed and fuel-air equivalence ratio interaction is significant to specific NOx emission; and percentage of H_2 and intake pressure interaction is significant to fuel energy.

Table 5.9:Most significant factors per response

SACI				
Response	η_{th}	NOx/kWh	CO_2/kWh	E_{fuel}
Significant Linear Factors	%H_2 ϕ P_{IV}	RPM ϕ P_{IV}	%H_2 P_{IV}	%H_2 ϕ P_{IV}
Significant Quadratic Factors	RPM ϕ P_{IV}	%H_2 ϕ	RPM P_{IV}	-
Significant Interactions	ϕ•P_{IV}	RPM•ϕ ϕ•P_{IV}	ϕ•P_{IV}	ϕ•P_{IV}
SI				
Response	η_{th}	NOx/kWh	CO_2/kWh	E_{fuel}
Significant Linear Factors	%H_2 RPM ϕ P_{IV}	ϕ P_{IV}	%H_2 RPM P_{IV}	%H_2 RPM ϕ P_{IV}
Significant Quadratic Factors	%H_2 RPM ϕ P_{IV}	%H_2 ϕ	RPM ϕ P_{IV}	%H_2 ϕ
Significant Interactions	ϕ•P_{IV}	RPM•ϕ ϕ•P_{IV}	ϕ•P_{IV}	%H_2•ϕ %H_2• P_{IV} ϕ•P_{IV}

6. Conclusions

In this chapter, the main results of this work will be presented and also the perspectives of future studies on the theme will be outlined.

6.1. Conclusion of the present work

Nowadays, decarbonization and energy efficiency are main issue to fulfill the commitments assumed at a global level in regard GHG emissions within tolerable limits, as to mitigate negative effects of climate changes within the context of energy transition. As the transport sector has relevant implication over environmental demands, internal combustion engines (ICE) fueled with hydrogen or biofuels and new combustion methods has been studied as an option to a gradual transition between actual ICE' technologies and engines with small environmental impact.

Thus, an ICE simulator was adapted in this work to predict the main parameters of spark ignition (SI) and Spark-Assisted Compression Ignition (SACI) engines. It was developed over a two-zone combustion thermodynamic model, providing 0D numerical information. With this simulator, it was done a sensibility study to understand the SACI multimodal combustion and its impact on ICE's performance parameters. The simulations investigated the engine's geometry and operating parameters in a methane and methane-hydrogen blends SI and SACI engine, respectively. A Box-Behnken design was used to comprehend the most significant factors and their influence.

The main conclusions were enumerated in the following items:

1. **Effects of percentage of H_2 on the SACI performance parameters:** The percentage of H_2 was a significant factor in all performance parameters since Hydrogen is the fuel with the highest LHV in weight basis, more than twice the value for methane. Thus, less fuel is necessary to supply the same amount of energy than only methane. On the other hand, the hydrogen properties (Table 3.2) significantly influence the heat release process since the fuel burns faster and then the combustion ends rapidly. ILBAS et al. (2006) investigated the laminar burning velocity in air of hydrogen, methane and hydrogen/methane blends, and showed that

for an equal range of equivalence ratio add 50% of H_2 in volume to the fuel mixture can increase more than three times the burning velocity of the blend. So, this early combustion ending may justify the decrease of thermal efficiency due to the less amount of fuel burned. Specific CO_2 emissions decreased when more carbon-free fuel is added (0% - 50% H_2).

2. **Effects of engine speed on the SACI performance parameters:** The engine speed was a significant factor in all performance parameters. As the engine speed is related to the volumetric efficiency, it commands the amount of air-fuel mixture that enters the cylinder. The SACI combustion method is based on the auto-ignition of the unburned gases, demonstrating an intense dependance of the mass of fresh air that will self-ignite. SACI engines are more efficient at low engine speeds because its thermal efficiency decays significantly at high rotations (up to 13%), that is the reason why they are preferable used in this operating point.
3. **Effects of fuel-air equivalence ratio on the SACI performance parameters**: The fuel-air equivalence ratio was also a significant factor in all performance parameters. Low-temperature combustion methods, as the SACI, utilizes lean and very lean mixtures in order to avoid high emissions of NOx and formation of CO_2. Consequently, specific NOx and CO_2 emissions are significantly lower than the SI engine ones. With lean mixtures, NOx emissions are practically nonexistent, but severely high when approximates from stoichiometric mixtures. CO_2 emissions are around 6% smaller at optimal points. SACI engine showed to be more efficient than SI engine even under adverse conditions.
4. **Effects of intake pressure on the SACI performance parameters**: The magnitude of the intake pressure defines the pressure's extent across the cycle. When the intake pressure is high, the AIT starts early, which can reduce thermal efficiency. High intake pressures make the use of better materials necessary. At 3 bar, for instance, the cylinder had to support pressures up to 300 bar. At the same range of intake pressure, SACI engine showed to emit eight times less NOx and 12% less CO_2 than SI engines in terms of specific emissions.
5. **Effects of valve overlap on the SACI performance parameters:** The valve overlap was not a significant factor to any performance parameter. A univariate analysis was made to understand thoroughly its effect over the performance parameters. The optimal points to thermal efficiency and specific NOx emissions was at -10°CA of valve overlap. Additionally, NOx

emissions showed to be 18% smaller than the valve overlap of +10°CA. Valve overlap did not show to have a significant effect over CO_2 emission under the conditions applied.

The objectives of this work were successfully attained, i.e., the simulator is now able to work with different simultaneous valve overlaps of intake and exhaust valves, approximating its results to real engine functioning; to operate under different heat transfer models, allowing to find a better reference of heat transfer between the studied models; to simulate the combustion of hydrogen, enabling the simulator to perform the combustion of a cleaner fuel. All the objectives were attained to both SACI and SI engines.

The SI engine has been widely studied since the beginning of the 20th century. The results obtained in this work for this engine enriches the technical-scientific research database. Besides, these results allow the strengthening the SACI combustion database, in a context in which this technology has only been studied in the past 20 years and there is still a lot of information to be evaluated and many research possibilities for a better understanding of this combustion model when compared to traditional (SI and CI) engines.

6.2. Perspectives to future works

The present work sought to bring an overview of the SACI combustion technology. Although, additional studies can be performed to investigate other performance aspects and consider new parameters. The following features can be investigated in future projects:

1. **Model combustion with the minimization of Gibbs free energy:** The combustion modeling can be modified to the minimization of Gibbs free energy. With this method, it is possible to set the wanted burned species, which permits the analysis of fuels that are not hydrocarbon nor alcohol. However, this approach does not take the intermediate species and the chemical reaction path into account. So, it should have an additional model for calculating the radical species molar fractions allowing the calculation of NOx with the Zeldovich mechanism.
2. **Further study emissions:** evaluate more deeply which factors interfere with emissions of NOx and CO_2 species and add the analysis of hydrocarbons and carbon monoxide emissions. In addition, looking for

ways to optimize the NOx emissions should be in the horizon of future studies.

3. **Simulate different valve overlaps:** To evaluate why the simulator results did not show significancy of this factor to the models, the simulation of bigger valve overlaps is an important step.
4. **Model, simulate and study the effects of stratified air-fuel mixtures:** One SACI characteristic not considered in the simulator is the stratification of the charge. This property indicates that the fuel-air equivalence ratio is not the same at all the cylinder volume. Add it on the model and simulate some cases would better outline SACI combustion.
5. **Model and simulate complete hydrogen SACI engines:** H_2 combustion is not simple to be implemented. Several intermediate species impact the combustion characteristics, and internal aerodynamic studies with an extremely lighter fuel are not yet robust. Future works could implement the hydrogen combustion reaction and apply it to a SACI engine. This examination can justify hydrogen internal combustion engines if the performance parameters indicate solid predictions.
6. **Model and simulate heavy duty hydrogen engines:** H_2 combustion is nowadays a trend in China, Korea, Europe and United Sates engine researches. Data from IEA (2023a) showed that buses have been the vehicles from transport sector that have used more of H_2 as fuel.
7. **Experimental validation:** the robustness of the prediction models could be improved with experimental test and a better calibration could be provided to the simulator.
8. **Comparison with CI engine:** the simulator was not yet compared and fitted to work under CI combustion. So, this adequation in the Matlab routine could provide a more general internal combustion engine simulator.

7. References

ALBAYRAK ÇEPER, B. et al. Performance and emission characteristics of an IC engine under SI, SI-CAI and CAI combustion modes. **Energy**, v. 136, p. 72–79, 2017.

ALI, N. M. Comparative Study of Performance and Emission Characteristics between Spark Ignition Engine and Homogeneous Charge Compression Ignition Engine (HCCI). **Al-Khwarizmi Engineering Journal**, v. 12, n. 4, p. 102–110, 18 dez. 2017.

ANNAND, W. J. D. Heat Transfer in the Cylinders of Reciprocating Internal Combustion Engines. **Proceedings of the Institution of Mechanical Engineers**, v. 177, n. 1, p. 973–996, 6 jun. 1963.

BABAJIMOPOULOS, A.; LAVOIE, G. A.; ASSANIS, D. N. **Modeling HCCI combustion with high levels of Residual Gas Fraction - A comparison of two VVA strategies**. SAE Technical Papers. **Anais**...SAE International, 2003.

BOX, G. E. P.; BEHNKEN, D. W. Some New Three Level Designs for the Study of Quantitative Variables. **Technometrics**, v. 2, n. 4, p. 455, nov. 1960.

BRUYNINCKX, H. **Shaping the future of energy in Europe: Clean, smart and renewable**. Disponível em: <https://www.eea.europa.eu/signals/signals-2017/articles/shaping-the-future-of-energy>. Acesso em: 25 dez. 2022.

BUNTING, B. G. **Combustion, Control, and Fuel Effects in a Spark Assisted HCCI Engine Equipped with Variable Valve Timing**. 3 abr. 2006. Disponível em: <https://www.sae.org/content/2006-01-0872/>

CATON, J. A. **An Introduction to Thermodynamic Cycle Simulations for Internal Combustion Engines**. [s.l.] Wiley, 2016.

ÇENGEL, Y. A.; BOLES, M. A. **Termodinâmica**. 7. ed. Porto Alegre: AMGH Editora Ltda., 2013.

CHANG, J. et al. **New heat transfer correlation for an HCCI engine derived from measurements of instantaneous surface heat flux**. SAE Technical Papers. **Anais**...SAE International, 2004.

CHANG, Y. et al. Effect of Ambient Temperature and Humidity on Combustion and Emissions of a Spark-Assisted Compression Ignition Engine. **Journal of Engineering for Gas Turbines and Power**, v. 139, n. 5, 1 maio 2017.

CHARALAMBIDES, A. G. Homogenous Charge Compression Ignition (HCCI) Engines. Em: **Advances in Internal Combustion Engines and Fuel Technologies**. [s.l.] InTech, 2013.

CHEN, L. et al. Effects of partitioned fuel distribution on auto-ignition and knocking under spark assisted compression ignition conditions. **Applied Energy**, v. 260, 15 fev. 2020.

CHEN, T. et al. **Continuous Load Adjustment Strategy of a Gasoline HCCI-SI Engine Fully Controlled by Exhaust Gas**. 12 abr. 2011. Disponível em: <https://www.sae.org/content/2011-01-1408/>

CHEN, Y. et al. An approach to estimate CCV (cycle-to-cycle variation) of effective energy output of thermal engine: A case study on a high speed gasoline engine. **Case Studies in Thermal Engineering**, v. 28, 1 dez. 2021.

CRIPPA, M. . et al. **GHG emissions of all world countries : 2023**. [s.l.] Publications Office of the European Union, 2023.

CUDDIHY, J. L. **A User-Friendly, Two-Zone Heat Release Model for Predicting Spark-Ignition Engine Performance and Emissions**. [s.l.] University of Idaho, maio 2014.

DABBAGHI, M. F. et al. Comparative evaluation of different heat transfer correlations on a single curved-cylinder spark ignition crank-rocker engine. **Alexandria Engineering Journal**, v. 60, n. 3, p. 2963–2978, 1 jun. 2021.

DANDAJEH, H. A.; SANUSI, Y. S.; AHMADU, T. O. Exhaust emission characteristics of a gardener compression ignition engine fuelled with rapeseed methyl ester and fossil diesel. **Nigerian Journal of Technology**, v. 39, n. 3, p. 752–760, 16 set. 2020.

DI IORIO, S.; SEMENTA, P.; VAGLIECO, B. M. Experimental investigation on the combustion process in a spark ignition optically accessible engine fueled with methane/hydrogen blends. **International Journal of Hydrogen Energy**, v. 39, n. 18, p. 9809–9823, 15 jun. 2014.

DIAZ, G. J. A. et al. Influence of engine operating conditions on combustion parameters in a spark ignited internal combustion engine fueled with blends of methane and hydrogen. **Energy Conversion and Management**, v. 181, p. 414–424, 1 fev. 2019.

DIMITROVA, I. D. et al. Computational analysis of an HCCI engine fuelled with hydrogen/hydrogen peroxide blends. **International Journal of Hydrogen Energy**, v. 47, n. 17, p. 10083–10096, 26 fev. 2022.

DUFFOUR, F. et al. **Influence of the Valve-lift Strategy in a CAI^{TM} Engine using Exhaust Gas Re-Breathing - Part 1: Experimental Results and 0D Analysis**. 20 abr. 2009. Disponível em: <https://www.sae.org/content/2009-01-0299/>

EDGAR/JRC. **Carbon dioxide emissions of the transportation sector worldwide in 2022, by select country**. Disponível em: <https://www.statista.com/statistics/1291501/transportation-emissions-worldwide-by-country/>. Acesso em: 31 jul. 2024.

EDGAR/JRC; STATISTA. **Carbon dioxide emissions of the transportation sector worldwide from 1990 to 2022, by region**. Disponível em: <https://www.statista.com/statistics/1200745/regional-carbon-dioxide-emissions-transport-sector-worldwide/>. Acesso em: 31 jul. 2024.

EICHELBERG, G. Some new investigations on old combustion engine problems. **Engineering**, v. 148, p. 547–550, 1939.

EPE. **BRAZILIAN ENERGY BALANCE (BEN) 2023**. [s.l: s.n.]. Disponível em: <http://www.epe.gov.br>.

FERGUSON, C. R.; KIRKPATRICK, A. T. **Internal Combustion Engines: Applied Thermosciences**. 3. ed. Chichester: John Wiley & Sons Ltd, 2016.

FERREIRA, S. L. C. et al. **Box-Behnken design: An alternative for the optimization of analytical methods**. **Analytica Chimica Acta**, 10 ago. 2007.

FURLANI, C. E. A.; SILVA, R. P. DA. **Motores de Combustão Interna**. 1. ed. São Paulo: UNESP, 2006. v. 2

GLEWEN, W. J. et al. Analysis of cyclic variability in spark-assisted HCCI combustion using a double Wiebe function. **Proceedings of the Combustion Institute**, v. 32 II, p. 2885–2892, 2009.

GREEN, A.; FANSHAWE, F.; CREPALDI, N. **21st Century Cities: Asia Pacific's urban transformation**. [s.l: s.n.]. Disponível em: <https://mittrinsights.s3.amazonaws.com/21stCenturyCities.pdf>. Acesso em: 29 abr. 2024.

HAGOS, F. Y. et al. Engine speed and air-fuel ratio effect on the combustion of methane augmented hydrogen rich syngas in DI SI engine. **International Journal of Hydrogen Energy**, p. 477–486, 1 jan. 2019.

HANSON, R. K.; SALIMIAN, S. Survey of Rate Constants in the N/H/O System. Em: **Combustion Chemistry**. New York: Springer-Verlag, 1984.

HEYWOOD, J. B. Pollutant formation and control in spark-ignition engines. **Progress in Energy and Combustion Science**, v. 1, n. 4, p. 135–164, jan. 1976.

HEYWOOD, J. B. **Internal combustion engine fundamentals**. [s.l.] McGraw-Hill, 1988.

HOHENBERG, G. F. **Advanced Approaches for Heat Transfer Calculations**. 1 fev. 1979.

HUNICZ, J. et al. Detailed analysis of combustion stability in a spark-assisted compression ignition engine under nearly stoichiometric and heavy EGR conditions. **Applied Energy**, v. 280, 15 dez. 2020.

IEA. **World Energy Outlook 2021**. Paris: [s.n.]. Disponível em: <www.iea.org/weo>.

IEA. **CO2 Emissions in 2022**. Paris: [s.n.]. Disponível em: <https://www.iea.org/reports/co2-emissions-in-2022>. Acesso em: 1 jun. 2024.

IEA. **Global Hydrogen Review 2023**. Paris: [s.n.]. Disponível em: <www.iea.org>.

IEA. **Net Zero Roadmap: A Global Pathway to Keep the 1.5 °C Goal in Reach - 2023 Update**. [s.l: s.n.]. Disponível em: <www.iea.org/t&c/>.

IEA. **World Energy Outlook 2023**. Paris: [s.n.]. Disponível em: <www.iea.org/terms>.

IHSAN SHAHID, M. et al. Comparative analysis of different heat transfer models, energy and exergy analysis for hydrogen-enriched internal combustion engine under different operation conditions. **Applied Thermal Engineering**, v. 247, p. 123004, jun. 2024.

ILBAS, M. et al. Laminar-burning velocities of hydrogen-air and hydrogen-methane-air mixtures: An experimental study. **International Journal of Hydrogen Energy**, v. 31, n. 12, p. 1768–1779, set. 2006.

KALGHATGI, G. **Is it really the end of internal combustion engines and petroleum in transport? Applied Energy**Elsevier Ltd, , 1 set. 2018.

KEROS, P. E. et al. **An Experimental Investigation of the Exhaust Emissions From Spark-Assisted Homogeneous Charge Compression Ignition in a Single-Cylinder Research Engine**. ASME 2009 Internal Combustion Engine Division Spring Technical Conference. **Anais**...ASMEDC, 1 jan. 2009. Disponível em:

<https://asmedigitalcollection.asme.org/ICES/proceedings/ICES2009/43406/309/337815>

KLEIN, M.; ERIKSSON, L. **A Specific Heat Ratio Model for Single-Zone Heat Release Models**. 8 mar. 2004. Disponível em: <https://www.jstor.org/stable/44723567>. Acesso em: 27 jul. 2024

KURIEN, C.; MITTAL, M. **Utilization of green ammonia as a hydrogen energy carrier for decarbonization in spark ignition engines**. **International Journal of Hydrogen Energy**Elsevier Ltd, , 29 ago. 2023.

LEITE, C. **Numerical study of spark-assisted compression ignition engines**. Rio de Janeiro: Pontifícia Universidade Católica do Rio de Janeiro (PUC-Rio), 4 out. 2021.

LI, X. et al. Numerical comparative study on performance and emissions characteristics fueled with methanol, ethanol and methane in high compression spark ignition engine. **Energy**, v. 254, 1 set. 2022.

LI, X. et al. Effect of air and gas dilution on combustion and emission characteristics in alcohol-gasoline fueled SACI engine. **Energy Conversion and Management**, v. 313, 1 ago. 2024.

LINDSEY, R.; DAHLMAN, L. **Climate Change: Global Temperature**. [s.l: s.n.]. Disponível em: <https://www.climate.gov/news-features/understanding-climate/climate-change-global-temperature#:~:text=Earth's%20temperature%20has%20risen%20by,based%20on%20NOAA's%20temperature%20data.>. Acesso em: 25 dez. 2022.

LOUNICI, M. S. et al. Investigation on heat transfer evaluation for a more efficient two-zone combustion model in the case of natural gas SI engines. **Applied Thermal Engineering**, v. 31, n. 2–3, p. 319–328, fev. 2011.

MALONEY, J. O. **Perry's chemical engineers' handbook. Section 1, Conversion factors and mathematical symbols**. [s.l.] McGraw-Hill, 2008.

MANOFSKY, L. et al. **Bridging the gap between HCCI and SI: Spark-assisted compression ignition**. SAE 2011 World Congress and Exhibition. **Anais**...2011.

MAZDA UK. **SKYACTIV-X with Spark Controlled Compression Ignition (SPCCI)**. Disponível em: <https://www.insidemazda.co.uk/2018/06/15/skyactiv-x-with-spark-controlled-compression-ignition-spcci/>. Acesso em: 14 jan. 2023.

MCBRIDE, B. J. et al. **NASA Technical Memorandum 4513 Coefficients for Calculating Thermodynamic and Transport Properties of Individual Species**. [s.l: s.n.]. Disponível em: <https://ntrs.nasa.gov/search.jsp?R=19940013151>.

MIDDLETON, R. J. et al. The effect of spark timing and negative valve overlap on Spark Assisted Compression Ignition combustion heat release rate. **Proceedings of the Combustion Institute**, v. 35, n. 3, p. 3117–3124, 2015.

MILLER, J. A.; BOWMAN, C. T. Mechanism and modeling of nitrogen chemistry in combustion. **Progress in Energy and Combustion Science**, v. 15, n. 4, p. 287–338, jan. 1989.

MORFELDT, J.; DAVIDSSON KURLAND, S.; JOHANSSON, D. J. A. Carbon footprint impacts of banning cars with internal combustion engines. **Transportation Research Part D: Transport and Environment**, v. 95, 1 jun. 2021.

NADALETI, W. C. et al. Methane-hydrogen fuel blends for SI engines in Brazilian public transport: Efficiency and pollutant emissions. **International Journal of Hydrogen Energy**, v. 42, n. 49, p. 29585–29596, dez. 2017.

NOAA CLIMATE.ORG. **Monthly Global Climate Report for Annual 2021**. [s.l: s.n.]. Disponível em: <https://www.ncdc.noaa.gov/sotc/global/202113>. Acesso em: 25 dez. 2022.

OLESKY, L. M. et al. The effects of spark timing, unburned gas temperature, and negative valve overlap on the rates of stoichiometric spark assisted compression ignition combustion. **Applied Energy**, v. 105, p. 407–417, 2013.

OLIKARA, C.; BORMAN, G. L. **A Computer Program for Calculating Properties of Equilibrium Combustion Products with Some Applications to I.C. Engines**. 1 fev. 1975.

ORTIZ-SOTO, E. A. et al. Thermodynamic efficiency assessment of gasoline spark ignition and compression ignition operating strategies using a new multi-mode combustion model for engine system simulations. **International Journal of Engine Research**, v. 20, n. 3, p. 304–326, 23 mar. 2019.

PERSSON, H. et al. **The Effect of Intake Temperature on HCCI Operation Using Negative Valve Overlap**. 8 mar. 2004. Disponível em: <https://www.sae.org/content/2004-01-0944/>

PERSSON, H. et al. **Cylinder-to-Cylinder and Cycle-to-Cycle Variations at HCCI Operation With Trapped Residuals**. 11 abr. 2005. Disponível em: <https://www.sae.org/content/2005-01-0130/>

PERSSON, H. et al. **Investigation of the Early Flame Development in Spark Assisted HCCI Combustion Using High Speed Chemiluminescence Imaging**. 16 abr. 2007. Disponível em: <https://www.sae.org/content/2007-01-0212/>

PERSSON, H.; JOHANSSON, B.; REMÓN, A. **The Effect of Swirl on Spark Assisted Compression Ignition (SACI)**. 23 jul. 2007. Disponível em: <https://www.sae.org/content/2007-01-1856/>

PIPITONE, E. **A New Simple Friction Model for S. I. Engine**. 15 jun. 2009.

PIPITONE, E.; BECCARI, S. A Comprehensive Model for the Auto-Ignition Prediction in Spark Ignition Engines Fueled With Mixtures of Gasoline and Methane-Based Fuel. **Journal of Engineering for Gas Turbines and Power**, v. 141, n. 4, 1 abr. 2019.

REITZ, R. D. **Directions in internal combustion engine research**. **Combustion and Flame**, jan. 2013.

SHAMUN, S. et al. Experimental investigation of methanol compression ignition in a high compression ratio HD engine using a Box-Behnken design. **Fuel**, v. 209, p. 624–633, 2017.

SHARMA, P. et al. Exploring the exhaust emission and efficiency of algal biodiesel powered compression ignition engine: Application of box–behnken and desirability based multi-objective response surface methodology. **Energies**, v. 14, n. 18, 1 set. 2021.

SINGH, A. P.; SONAWANE, U.; AGARWAL, A. K. Methanol/Ethanol/Butanol-Gasoline Blends Use in Transportation Engine-Part 1: Combustion, Emissions, and Performance Study. **Journal of Energy Resources Technology, Transactions of the ASME**, v. 144, n. 10, 1 out. 2022.

SITKEI, G.; RAMANAIAH, G. V. **A Rational Approach for Calculation of Heat Transfer in Diesel Engines**. 1 fev. 1972.

STATISTA. **Transportation emissions worldwide - statistics & facts**. Disponível em: <https://www.statista.com/topics/7476/transportation-emissions-worldwide/#topicOverview>. Acesso em: 30 jul. 2024.

UNFCCC. **What is the Paris Agreement?** Disponível em: <https://unfccc.int/process-and-meetings/the-paris-agreement/the-paris-agreement>. Acesso em: 25 dez. 2022.

URUSHIHARA, T. et al. **A Study of a Gasoline-fueled Compression Ignition Engine ~ Expansion of HCCI Operation Range Using SI Combustion as a Trigger of Compression Ignition ~**. 11 abr. 2005. Disponível em: <https://www.sae.org/content/2005-01-0180/>

WAGNER, R. M. et al. **On the Nature of Cyclic Dispersion in Spark Assisted HCCI Combustion**. 3 abr. 2006. Disponível em: <https://www.sae.org/content/2006-01-0418/>

WAGNER, R. M. et al. **Hybrid SI-HCCI combustion modes and the potential for control**. [s.l: s.n.]. Disponível em: <https://www.researchgate.net/publication/236440688>.

WANG, S.; GE, M. **Everything You Need to Know About the Fastest-Growing Source of Global Emissions: Transport**. Disponível em: <https://www.wri.org/insights/everything-you-need-know-about-fastest-growing-source-global-emissions-transport>. Acesso em: 25 dez. 2022.

WANG, Z. et al. **Effects of Spark Ignition and Stratified Charge on Gasoline HCCI Combustion With Direct Injection**. 11 abr. 2005. Disponível em: <https://www.sae.org/content/2005-01-0137/>

WANG, Z. et al. Study of the effect of spark ignition on gasoline HCCI combustion. **Proceedings of the Institution of Mechanical Engineers, Part D: Journal of Automobile Engineering**, v. 220, n. 6, p. 817–825, 2006.

WANG, Z. et al. Combustion visualization and experimental study on spark induced compression ignition (SICI) in gasoline HCCI engines. **Energy Conversion and Management**, v. 51, n. 5, p. 908–917, maio 2010.

WEF. **How will car use change over the next 50 years**. Disponível em: <https://www.weforum.org/agenda/2021/11/where-car-use-is-rising-falling/>. Acesso em: 28 dez. 2022.

WOSCHNI, G. **A Universally Applicable Equation for the Instantaneous Heat Transfer Coefficient in the Internal Combustion Engine**. 1 fev. 1967.

WRI. **Global Historical Emissions - Climate Watch Data**. Disponível em: <https://www.climatewatchdata.org/ghg-emissions?end_year=2021&start_year=1990>. Acesso em: 30 jul. 2024.

WRI. **Brazil Deforestation Rates & Statistics - GFW**. Disponível em: <https://www.globalforestwatch.org/dashboards/country/BRA/?category=climate&location=WyJjb3VudHJ5IiwiQlJBIl0%3D>. Acesso em: 29 jul. 2024.

XIE, H. et al. Study on spark assisted compression ignition (SACI) combustion with positive valve overlap at medium-high load. **Applied Energy**, v. 101, p. 622–633, 2013a.

XIE, H. et al. Study on spark assisted compression ignition (SACI) combustion with positive valve overlap at medium-high load. **Applied Energy**, v. 101, p. 622–633, 2013b.

YANG, C.; ZHAO, H. In-cylinder studies of CAI/HCCI combustion with negative valve overlap in a direct injection gasoline optical engine. **Combustion Science and Technology**, v. 183, n. 5, p. 467–486, maio 2011.

YANG, C.; ZHAO, H.; MEGARITIS, T. **Investigation of CAI Combustion with Positive Valve Overlap and Enlargement of CAI Operating Range**. 20 abr. 2009. Disponível em: <https://www.sae.org/content/2009-01-1104/>

YANG, R. et al. Numerical Investigation of the Fuel/Air Ratio Sensor Sensitivity in a Port-Fuel-Injected Spark-Ignition Engine Equipped With Three-Way Catalysts. **Journal of Energy Resources Technology, Transactions of the ASME**, v. 145, n. 5, 1 maio 2023.

YANG, X.; ZHU, G. G. A control-oriented hybrid combustion model of a homogeneous charge compression ignition capable spark ignition engine. **Proceedings of the Institution of Mechanical Engineers, Part D: Journal of Automobile Engineering**, v. 226, n. 10, p. 1380–1395, 2012.

YAO, M.; ZHENG, Z.; LIU, H. **Progress and recent trends in homogeneous charge compression ignition (HCCI) engines**. **Progress in Energy and Combustion Science**, out. 2009.

YILDIZ, M.; ALBAYRAK ÇEPER, B. Zero-dimensional single zone engine modeling of an SI engine fuelled with methane and methane-hydrogen blend using single and double Wiebe Function: A comparative study. **International Journal of Hydrogen Energy**, v. 42, n. 40, p. 25756–25765, 5 out. 2017.

YILDIZ, M.; ÇEPER, B. A. Zero-dimensional single zone engine modeling of an SI engine fuelled with methane and methane-hydrogen blend using single and double Wiebe Function: A comparative study. **International Journal of Hydrogen Energy**, v. 42, n. 40, p. 25756–25765, 5 out. 2017.

YIN, S. **Volumetric Efficiency Modeling of a Four Stroke IC Engine**. Master—Fort Collins: Colorado State University, 2017.

YOO, C. S. et al. Direct numerical simulations of ignition of a lean n-heptane/air mixture with temperature inhomogeneities at constant volume: Parametric study. **Combustion and Flame**, v. 158, n. 9, p. 1727–1741, set. 2011.

YOO, C. S. et al. A DNS study of ignition characteristics of a lean iso-octane/air mixture under HCCI and SACI conditions. **Proceedings of the Combustion Institute**, v. 34, n. 2, p. 2985–2993, 2013.

YUN, H.; WERMUTH, N.; NAJT, P. High Load HCCI Operation Using Different Valving Strategies in a Naturally-Aspirated Gasoline HCCI Engine. **SAE International Journal of Engines**, v. 4, n. 1, p. 2011- 01–0899, 12 abr. 2011.

ZHANG, F. et al. Direct numerical simulation of flame/spontaneous ignition interaction fueled with hydrogen under SACI engine conditions. **International Journal of Hydrogen Energy**, v. 42, n. 6, p. 3842–3852, 9 fev. 2017.

ZHANG, Y. et al. Experimental investigation of the high-pressure SCR reactor impact on a marine two-stroke diesel engine. **Fuel**, v. 335, 1 mar. 2023.

ZHAO, T. et al. AN EXPERIMENTAL STUDY ON COMBUSTION AND EMISSIONS CHARACTERISTICS IN A DUAL-INJECTION SPARK-ASSISTED COMPRESSION IGNITION ENGINE FUELED WITH PODE/GASOLINE. **Thermal Science**, v. 27, n. 5, p. 3757–3768, 2023.

ZHOU, L. et al. Effects of applying EGR with split injection strategy on combustion performance and knock resistance in a spark assisted compression ignition (SACI) engine. **Applied Thermal Engineering**, v. 145, p. 98–109, 25 dez. 2018.

ZHU, T. et al. Effects of intake conditions on a dual-fuel spark-assisted compression ignition engine with polyoxymethylene dimethyl ether and methanol as fuels. **Fuel**, v. 357, 1 fev. 2024.

8. Appendices

A. SACI Literature Review Summary

Table A.1: Summary of the studies discussed in the 2.3.2 section

Title	Author	Combustion	Fuel	Analysis	Year	Comments
Effects of Spark Ignition and Stratified Charge on Gasoline HCCI Combustion with Direct Injection	Wang et al.	SI, HCCI, and SACI	Gasoline	Experimental	2005	• Spark ignition assistance • Fuel injection • Stratified charge
A Study of a Gasoline-fueled Compression Ignition Engine ~ Expansion of HCCI Operation Range Using SI Combustion as a Trigger of Compression Ignition ~	Urushihara et al.	SACI	Gasoline	Experimental	2005	• Combustion phasing • EGR
Study of the effect of spark ignition on gasoline HCCI combustion	Wang et al.	SI, HCCI, and SACI	Gasoline	Experimental	2006	• Spark ignition assistance • Performance
Combustion, Control, and Fuel Effects in a Spark Assisted HCCI Engine Equipped with Variable Valve Timing	Bunting	SACI	Gasoline and Indolene blends	Experimental	2006	• Spark timings • Combustion phasing • NVO
Bridging the Gap between HCCI and SI: Spark-Assisted Compression Ignition	Manofsky et al.	SACI	Gasoline	Experimental	2011	• Spark timings • Performance • NVO

The effects of spark timing, unburned gas temperature, and negative valve overlap on the rates of stoichiometric spark assisted compression ignition combustion	Olesky et al.	SACI	Gasoline	Experimental	2013	• Spark timing • Unburned temperature • NVO ranges • EGR
A DNS study of ignition characteristics of a lean isooctane/air mixture under HCCI and SACI conditions	Yoo et al.	HCCI and SACI	Isooctane	Numerical	2013	• Thermal stratification • Spark ignition • Turbulence
Analysis of cyclic variability in spark-assisted HCCI combustion using a double Wiebe function	Glewen et al.	SI, HCCI, and SACI	Indolene	Numerical	2009	• EGR
Hybrid SI-HCCI combustion modes and the potential for control	Wagner et al.	SI, HCCI, and SACI	Indolene and 85/15 ethanol-indolene blend	Experimental	2007	• Spark timing • EGR
The Effect of Intake Temperature on HCCI Operation Using Negative Valve Overlap	Persson et al.	SI and HCCI	-	Experimental	2004	• Intake temperature • EGR • NVO
Cylinder-to-Cylinder and Cycle-to-Cycle Variations at HCCI Operation with Trapped Residuals	Persson et al.	HCCI	-	Experimental	2005	• Deviations of operating region • Spark timing
The Effect of Swirl on Spark Assisted Compression Ignition (SACI)	Persson; Johansson; Remón.	SI, HCCI and SACI	-	Experimental	2007	• Swirl • Turbulence • NVO • EGR
On the Nature of Cyclic Dispersion in Spark Assisted HCCI Combustion	Wagner et al.	SI, HCCI and SACI	Gasoline	Experimental	2006	• Variable engine speed • Variable load • EGR
Investigation of the Early Flame Development in Spark Assisted HCCI Combustion Using High Speed Chemiluminescence Imaging	Persson et al.	SI, HCCI and SACI	Gasoline	Experimental	2007	• Intake temperature • EGR • NVO

In-Cylinder Studies Of CAI/HCCI Combustion with Negative Valve Overlap In A Direct Injection Gasoline Optical Engine	Yang; Zhao.	SACI	Gasoline	Experimental	2011	• Injection timing • Spark discharge • NVO • EGR
Continuous Load Adjustment Strategy of a Gasoline HCCI-SI Engine Fully Controlled by Exhaust Gas	Chen et al.	SI, HCCI and SACI	Gasoline	Experimental	2011	• Adjustable load • NVO • EGR
Study on spark assisted compression ignition (SACI) combustion with positive valve overlap at medium–high load	Xie et al.	SACI	Gasoline	Numerical	2013	• Emissions • PVO • NVO • EGR
Modeling HCCI Combustion with High Levels of Residual Gas Fraction – A Comparison of Two VVA Strategies	Babajimopulos; Lavoie; Assanis.	HCCI	Natural Gas	Numerical	2003	• VVA** • EGR
Effect of air and gas dilution on combustion and emission characteristics in alcohol-gasoline fueled SACI engine	Li et al.	SACI	Alcohol Gasoline	Experimental	2024	• Emissions • EGR • Valve timing and lifting
Influence of the Valve-lift Strategy in a CAI™ Engine using Exhaust Gas Re-Breathing - Part 1: Experimental Results and 0D Analysis	Duffour et al.	SACI	-	Experimental and Numerical	2009	• VVA • EGR
Investigation of CAI Combustion with Positive Valve Overlap and Enlargement of CAI Operating Range	Yang; Zhao; Megaritis.	SACI	Gasoline	Experimental	2009	• Performance • Emissions • PVO • EGR
High Load HCCI Operation Using Different Valving Strategies in a Naturally-Aspirated Gasoline HCCI Engine	Yun; Wermuth; Najt.	SI, HCCI and SACI	Gasoline	Experimental	2011	• Valve configurations • PVO • NVO • EGR

Combustion visualization and experimental study on spark induced compression ignition (SICI) in gasoline HCCI engines	Wang et al.	HCCI and SACI	Gasoline	Experimental	2010	• Combustion visualization • EGR
Direct numerical simulations of ignition of a lean n-heptane/air mixture with temperature inhomogeneities at constant volume: Parametric study	Yoo et al.	HCCI	Heptane	Numerical	2011	• Thermal stratification • Turbulence
An Experimental Investigation of the Exhaust Emissions from Spark-Assisted Homogeneous Charge Compression Ignition in a Single-Cylinder Research Engine	Keros et al.	HCCI and SACI	Indolene	Experimental	2009	• Emissions
Progress and recent trends in homogeneous charge compression ignition (HCCI) engines	Yao; Zheng; Liu.	HCCI	Isooctane Natural gas Ethanol Methanol	Numerical	2009	• Fuel • Additives • Optical analysis • EGR
Performance and emission characteristics of an IC engine under SI, SI-CAI and CAI combustion modes	Albayrak Çeper et al.	SI, HCCI and SACI	Gasoline	Experimental	2017	• Emissions • Performance • Engine speed • EAR • WOT
Effect of Ambient Temperature and Humidity on Combustion and Emissions of a Spark-Assisted Compression Ignition Engine	Chang et al.	SI, HCCI and SACI	Gasoline	Experimental	2017	• Ambient temperature • Humidity • EGR
An Experimental Study on Combustion and Emissions Characteristics in A Dual-Injection Spark-Assisted Compression Ignition Engine Fueled With PODE/Gasoline	Zhao et al.	SACI	PODE Gasoline	Experimental	2023	• Equivalence ratio variation • Direct fuel injection
Thermodynamic efficiency assessment of gasoline spark ignition and compression ignition operating strategies using a new multi-mode combustion model for engine system simulations	Ortiz-Soto et al.	SI, HCCI and SACI	Isooctano	Numerical	2019	• Spark timing • Manifold pressure • NVO • EGR

Effects of partitioned fuel distribution on auto-ignition and knocking under spark assisted compression ignition conditions	Chen et al.	SI and SACI	n-heptane Methane	Experimental	2020	• Knocking • Fuel • Injection timing • Optical analysis
The effect of spark timing and negative valve overlap on Spark Assisted Compression Ignition combustion heat release rate	Middleton et al.	SACI	Gasoline	Numerical	2015	• Spark timing • Unburned temperature
Effects of applying EGR with split injection strategy on combustion performance and knock resistance in a spark assisted compression ignition (SACI) engine	Zhou et al.	SI and SACI	Gasoline	Experimental	2018	• EGR • Valve configurations • NVO • Knocking • Ignition timing
Direct numerical simulation of flame/spontaneous ignition interaction fueled with hydrogen under SACI engine conditions	Zhang et al.	SACI	Hydrogen CO Methane	Numerical	2018	• Fuel • Initial temperature • EGR • Equivalence ratio

**VVA = Variable Valve Actuation.

B. Mathematical Modelling Details

Table B.1: NASA model constants (MCBRIDE et al., 1993)

Species	Range	a_1	a_2	a_3	a_4	a_5	a_6	a_7	b_1	b_2
CO_2	T ≤ 1000	+4.94E+04	−6.26E+02	+5.30E+00	+2.50E−03	−2.12E−07	−7.68E−10	+2.84E−13	−4.52E+04	−7.04E+00
	T > 1000	+1.17E+05	−1.78E+03	+8.29E+00	−9.22E−05	+4.86E−09	−1.89E−12	+6.33E−16	−3.90E+04	−2.65E+01
H_2O	T ≤ 1000	−3.94E+04	+5.75E+02	+9.31E−01	+7.22E−03	−7.34E−06	+4.95E−09	−1.33E−12	−3.30E+04	+1.72E+01
	T > 1000	+1.03E+06	−2.41E+03	+4.64E+00	+2.29E−03	−6.83E−07	+9.42E−11	−4.82E−15	−1.38E+04	−7.97E+00
N_2	T ≤ 1000	+2.21E+04	−3.81E+02	+6.08E+00	−8.53E−03	+1.38E−05	−9.62E−09	+2.51E−12	+7.10E+02	−1.07E+01
	T > 1000	+5.87E+05	−2.23E+03	+6.06E+00	−6.13E−04	+1.49E−07	−1.92E−11	+1.06E−15	+1.28E+04	−1.58E+01
O_2	T ≤ 1000	−3.42E+04	+4.84E+02	+1.11E+00	+4.29E−03	−6.83E−07	−2.02E−09	+1.03E−12	−3.39E+03	+1.84E+01
	T > 1000	−1.03E+06	+2.34E+03	+1.81E+00	+1.26E−03	−2.18E−07	+2.05E−11	−8.19E−16	−1.68E+04	+1.73E+01
CO	T ≤ 1000	+1.48E+04	−2.92E+02	+5.72E+00	−8.17E−03	+1.45E−05	−1.08E−08	+3.02E−12	−1.30E+04	−7.85E+00
	T > 1000	+4.61E+05	−1.94E+03	+5.91E+00	−5.66E−04	+1.39E−07	−1.78E−11	+9.62E−16	−2.46E+03	−1.38E+01
H_2	T ≤ 1000	+4.07E+04	−8.00E+02	+8.21E+00	−1.26E−02	+1.75E−05	−1.20E−08	+3.36E−12	+2.68E+03	−3.04E+01
	T > 1000	+5.60E+05	−8.37E+02	+2.97E+00	+1.25E−03	−3.74E−07	+5.93E−11	−3.60E−15	+5.33E+03	−2.20E+00
H	T ≤ 1000	+0.00E+00	+0.00E+00	+2.50E+00	0.00E+00	0.00E+00	0.00E+00	0.00E+00	+2.54E+04	−4.46E−01
	T > 1000	+6.07E+01	−1.81E−01	+2.50E+00	−1.22E−07	+3.73E−11	−5.68E−15	+3.41E−19	+2.54E+04	−4.48E−01
O	T ≤ 1000	−7.95E+03	+1.60E+02	+1.96E+00	+1.01E−03	−1.11E−06	+6.51E−10	−1.58E−13	+2.84E+04	+8.40E+00
	T > 1000	+2.61E+05	−7.29E+02	+3.31E+00	−4.28E−04	+1.03E−07	−9.43E−12	+2.72E−16	+3.39E+04	−6.67E−01
OH	T ≤ 1000	−1.99E+03	+9.30E+01	+3.05E+00	+1.52E−03	−3.15E−06	+3.31E−09	−1.13E−12	+2.99E+03	+4.67E+00
	T > 1000	+1.01E+06	−2.50E+03	+5.11E+00	+1.30E−04	−8.28E−08	+2.00E−11	+1.55E−15	+2.01E+04	−1.10E+01
NO	T ≤ 1000	−1.14E+04	+1.53E+02	+3.43E+00	−2.66E−03	+8.48E−06	−7.68E−09	+2.38E−12	+9.09E+03	+6.72E+00
	T > 1000	+2.23E+05	−1.28E+03	+5.43E+00	−3.65E−04	+9.88E−08	−1.41E−11	+9.38E−16	+1.75E+04	−8.50E+00

Table B.2: Perry fuel model constants (MALONEY, 2008)

Fuel	C1	C2	C3	C4	C5	$h(T_{ref})$ (kJ/(kmol.K))	$s(T_{ref})$ (kJ/(kmol.K))
Methane	+3.33E+04	+7.99E+04	+2.09E+03	+4.16E+04	+991.96	−7.45E+07	+1.86E+05
Hydrogen	+2.76E+04	+9.56E+03	+2.47E+03	+3.76E+03	+567.6	0	+1.31E+05

Table B.3: Complete regression model of a_W (equation (3-68))

Effect Estimates; Var.:a; R-sqr=,69914; Adj:,68195 (Spreadsheet1)
2 factors, 1 Blocks, 38 Runs; MS Residual=1,031341
DV: a

Factor	Effect	Std.Err.	t(35)	p	-95,% Cnf.Limt	+95,% Cnf.Limt	Coeff.	Std.Err. Coeff.	-95,% Cnf.Limt	+95,% Cnf.Limt
Mean/Interc.	3,123799	0,227553	13,72777	0,000000	2,661841	3,585756	3,123799	0,227553	2,661841	3,585756
(1)%CH4(L)	5,131957	0,616029	8,33070	0,000000	3,881351	6,382563	2,565978	0,308015	1,940675	3,191281
%CH4(Q)	5,177697	0,823086	6,29059	0,000000	3,506744	6,848650	2,588848	0,411543	1,753372	3,424325

Table B.4: Complete regression model of k_W (equation (3-69))

Factor	Effect Estimates; Var.:k; R-sqr=,70528; Adj:,68844 (Spreadsheet1) 2 factors, 1 Blocks, 38 Runs; MS Residual=,0725434 DV: k Effect	Std.Err.	t(35)	p	-95,% Cnf.Limt	+95,% Cnf.Limt	Coeff.	Std.Err. Coeff.	-95,% Cnf.Limt	+95,% Cnf.Limt
Mean/Interc.	3,54255	0,060350	58,69965	0,000000	3,42004	3,66507	3,542553	0,060350	3,42004	3,665071
(1)%CH4(L)	-1,24656	0,163380	-7,62982	0,000000	-1,57824	-0,91488	-0,623281	0,081690	-0,78912	-0,457441
%CH4(Q)	-1,64108	0,218295	-7,51774	0,000000	-2,08424	-1,19792	-0,820541	0,109147	-1,04212	-0,598960

Table B.5: Complete regression model of θ_d (equation (3-70))

Factor	Effect Estimates; Var.:Delta_theta; R-sqr=,93322; Adj:,92512 (Spreadsheet1) 2 factors, 1 Blocks, 38 Runs; MS Residual=6,233852 DV: Delta_theta Effect	Std.Err.	t(33)	p	-95,% Cnf.Limt	+95,% Cnf.Limt	Coeff.	Std.Err. Coeff.	-95,% Cnf.Limt	+95,% Cnf.Limt
Mean/Interc.	32,11964	0,727397	44,15698	0,000000	30,63974	33,59954	32,11964	0,727397	30,63974	33,59954
(1)%CH4(L)	29,81448	1,515591	19,67185	0,000000	26,73099	32,89798	14,90724	0,757796	13,36550	16,44899
%CH4(Q)	29,92856	2,044895	14,63574	0,000000	25,76819	34,08893	14,96428	1,022448	12,88409	17,04446
(2)Phi (L)	-3,94413	1,044141	-3,77739	0,000630	-6,06845	-1,81981	-1,97206	0,522071	-3,03423	-0,90990
Phi (Q)	-3,85060	1,729698	-2,22617	0,032946	-7,36969	-0,33150	-1,92530	0,864849	-3,68485	-0,16575

C. Research flowchart

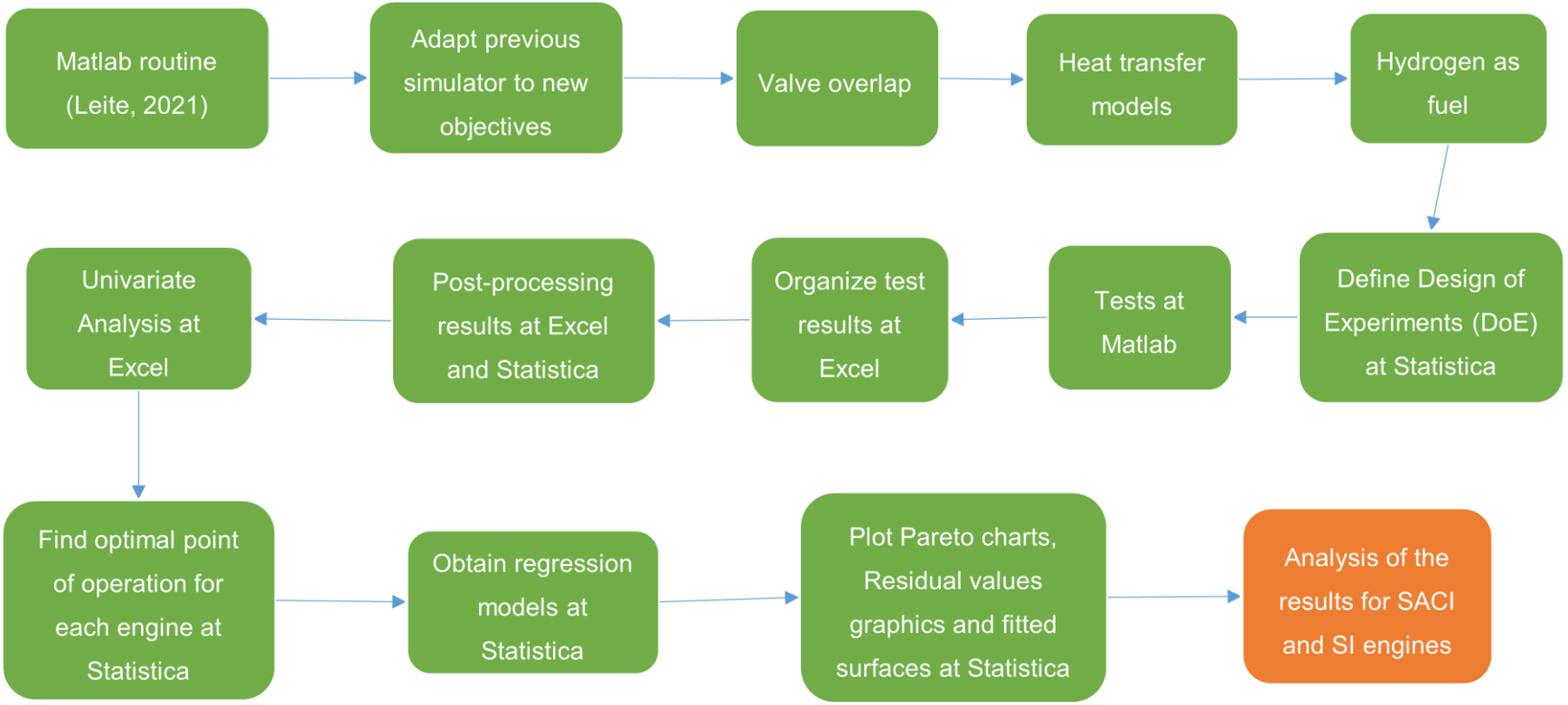

D. Baseline Case Study for SI engine

To understand the simulator plots capabilities and best compare the SI engine with SACI engine, the results for the 21st test of Table 4.1 at are plotted in this Appendix. Table D.1 shows engine specifications.

Table D.1: Engine Specification for the BBD tests

Geometric parameters	
Number of cylinders	4
Bore (mm)	83
Stroke (mm)	81.4
Half-stroke to Rod Ratio	0.271
Total Displacement Volume (cm^3)	1761
Compression ratio, r_c	10
Valve timing	
IVO	0°aTDC
IVC	45°aBDC
EVO	35°bTDC
EVC	0°bBDC
Operating point	
Engine speed (rpm)	3000
Fuel type	25%H_2/75%CH_4
Equivalence ratio, $\boldsymbol{\phi}$	0.65
P_{IV} (bar)	1.0
T_{IV} (K)	380
T_{EV} (K)	480
Wiebe parameters	
a_W	3.1238
$\boldsymbol{\theta_s}$	-20°
$\boldsymbol{\theta_{d,SI}}$	46°
$k_{W,SI}$	3.5426
$\boldsymbol{\theta_{d,HCCI}}$	11°
$k_{W,HCCI}$	6.00

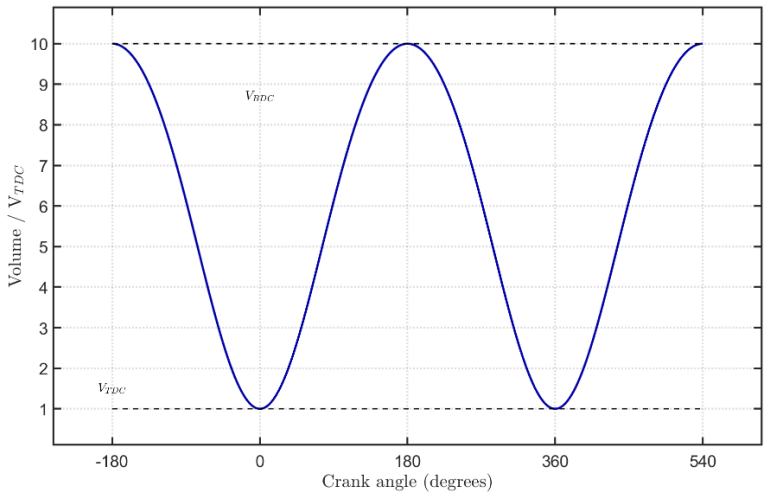

Figure D.1: In-cylinder volume in function of the crank angle.

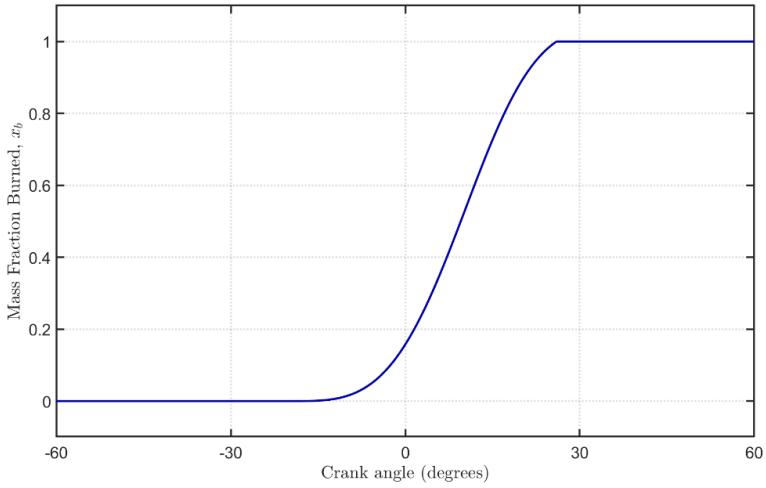

Figure D.2: Mass fraction burned in function of the crank angle.

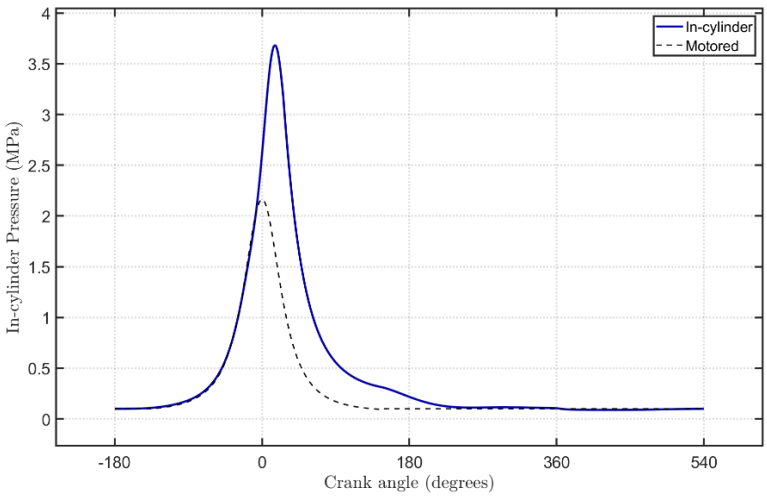

Figure D.3: In-cylinder Pressure.

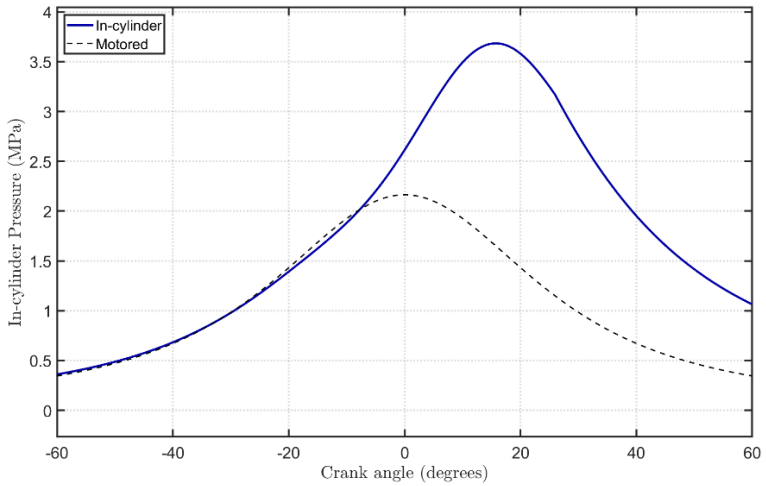

Figure D.4: In-cylinder Pressure Zoom.

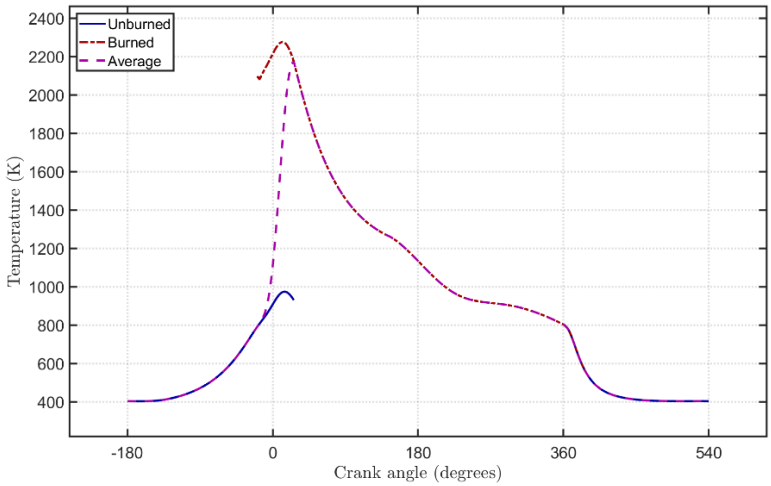

Figure D.5: In-cylinder Temperature.

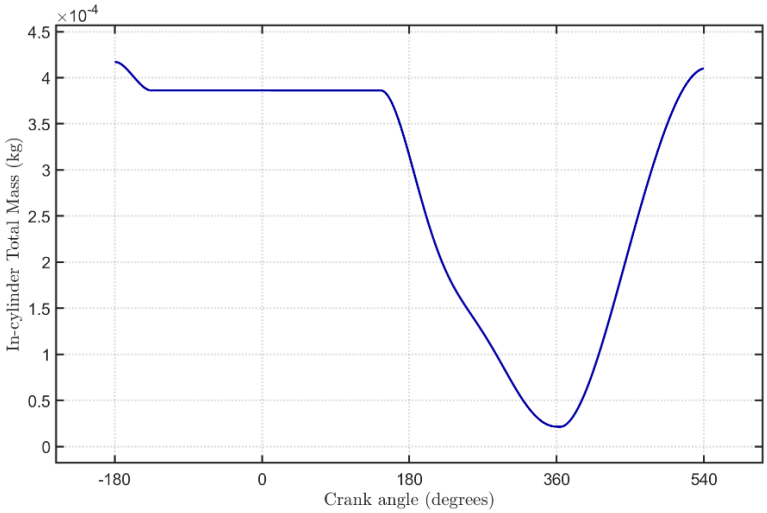

Figure D.6: In-cylinder Mass.

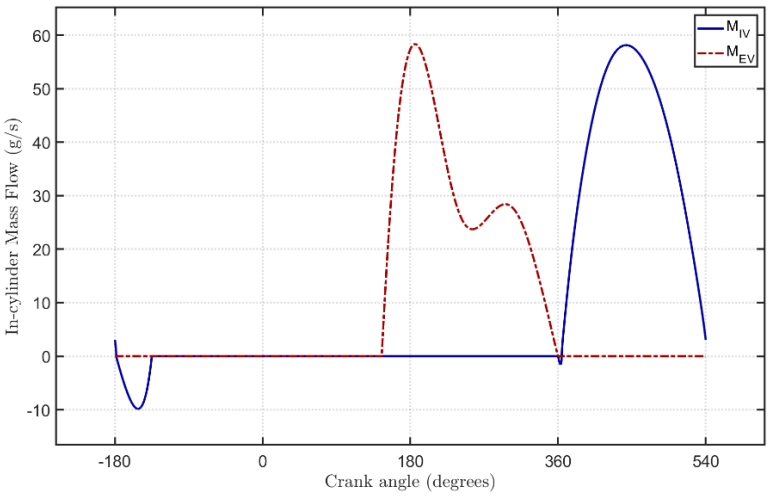

Figure D.7: In-cylinder Mass Flow.

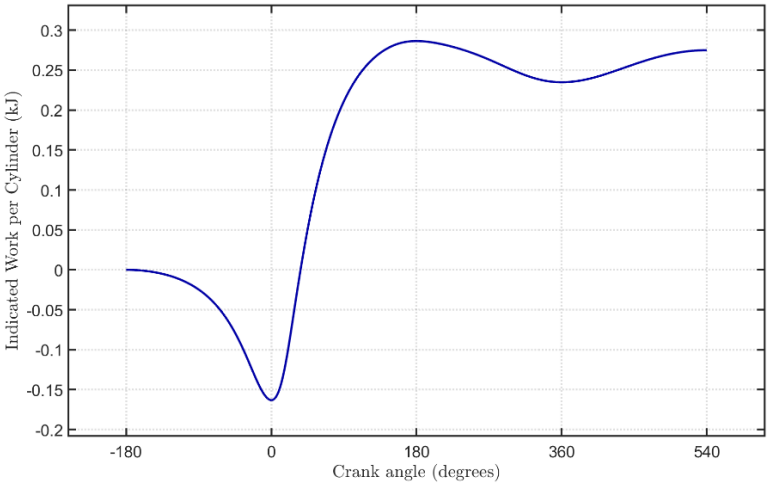

Figure D.8: Work.

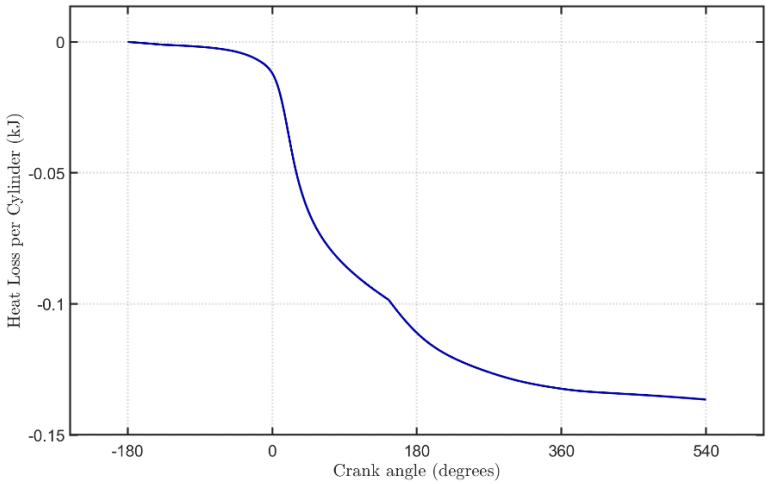

Figure D.9: Heat Loss.

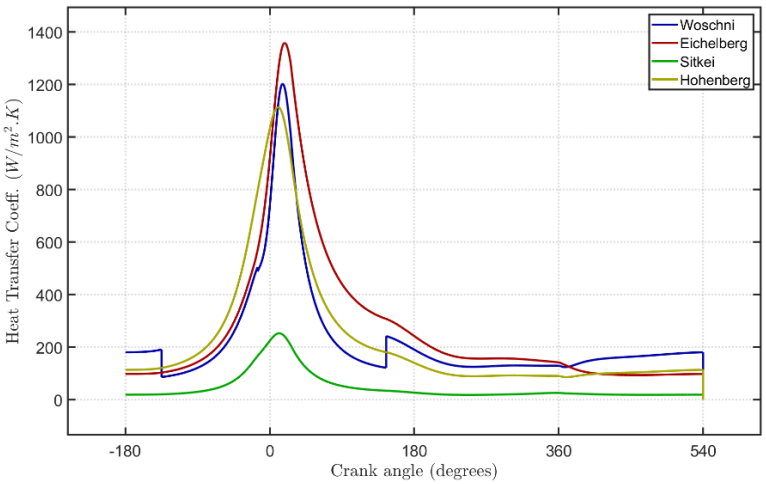

Figure D.10: Heat Transfer Coefficients.

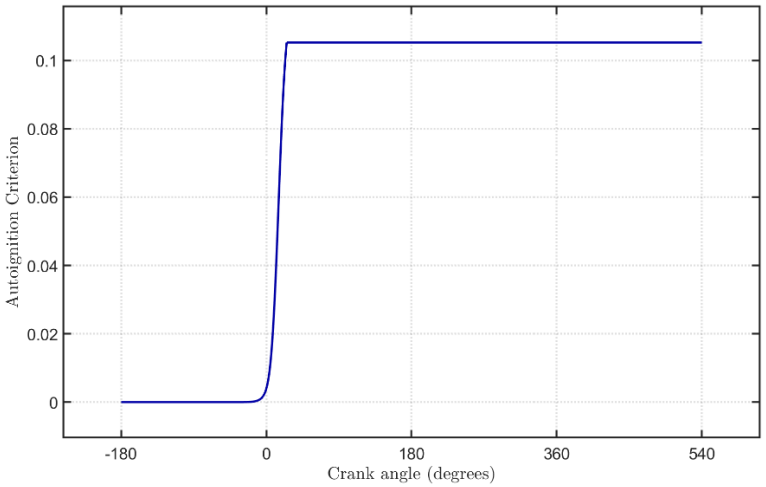

Figure D.11: Knock Integral.

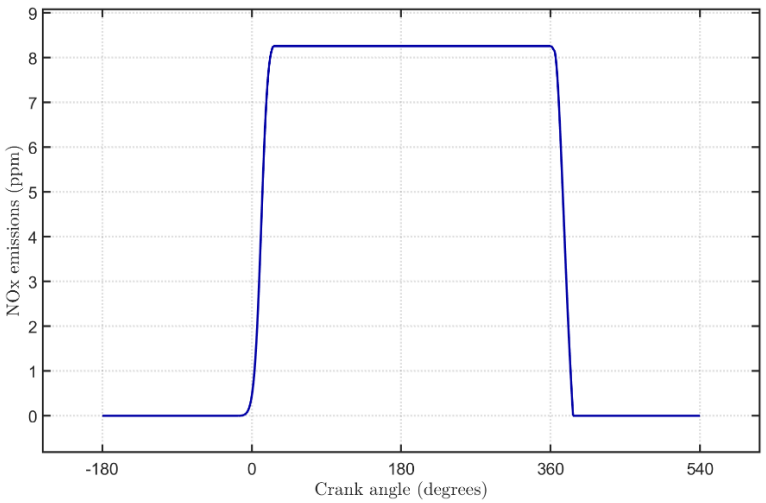

Figure D.12: NOx formation as a function of the crank angle.

E. SACI and SI Polynomial Models' Description

Table E.1: Complete regression model of η_{th} to SI engine (equation (5-1))

Effect Estimates; Var.:ηth (%); R-sqr=,97662; Adj:,95863 (SI Results) 5 3-level factors, 1 Blocks, 47 Runs; MS Residual=,8269393 DV: ηth (%)				
Factor	Coeff.	Std.Err.	t(26)	p
Mean/Interc.	30.66190	0.331558	92.4784	0.000000
(1)H2 percentage in fuel (%)(L)	-5.77250	0.227341	-25.3914	0.000000
H2 percentage in fuel (%)(Q)	-1.06905	0.149859	-7.1337	0.000000
(2)Engine speed (rpm)(L)	-0.78063	0.227341	-3.4337	0.002006
Engine speed (rpm)(Q)	0.55887	0.149859	3.7293	0.000943
(3)Fuel-air equivalence ratio (phi)(L)	-1.15625	0.227341	-5.0860	0.000027
Fuel-air equivalence ratio (phi)(Q)	0.37512	0.149859	2.5031	0.018922
(4)Intake pressure (bar)(L)	3.27750	0.227341	14.4167	0.000000
Intake pressure (bar)(Q)	1.01595	0.149859	6.7794	0.000000
(5)Valve overlap (ºCA)(L)	-0.33813	0.227341	-1.4873	0.148962
Valve overlap (ºCA)(Q)	-0.10446	0.149859	-0.6971	0.491938
1L by 2L	-0.33750	0.454681	-0.7423	0.464572
1L by 3L	0.19500	0.454681	0.4289	0.671549
1L by 4L	-0.72000	0.454681	-1.5835	0.125391
1L by 5L	0.06250	0.454681	0.1375	0.891727
2L by 3L	0.66750	0.454681	1.4681	0.154082
2L by 4L	-0.73250	0.454681	-1.6110	0.119251
2L by 5L	-0.37500	0.454681	-0.8248	0.417014
3L by 4L	-2.71500	0.454681	-5.9712	0.000003
3L by 5L	-0.00250	0.454681	-0.0055	0.995655
4L by 5L	-0.13250	0.454681	-0.2914	0.773048

Table E.2: Complete regression model of η_{th} to SACI engine (equation (5-2))

Effect Estimates; Var.:ηth (%); R-sqr=,95272; Adj:,91634 (SACI Results) 5 3-level factors, 1 Blocks, 47 Runs; MS Residual=1,435985 DV: ηth (%)				
Factor	Coeff.	Std.Err.	t(26)	p
Mean/Interc.	32.64351	0.436915	74.7136	0.000000
(1)H2 percentage in fuel (%)(L)	-4.78875	0.299582	-15.9848	0.000000
H2 percentage in fuel (%)(Q)	-0.30960	0.197479	-1.5677	0.129031
(2)Engine speed (rpm)(L)	0.35188	0.299582	1.1746	0.250819
Engine speed (rpm)(Q)	0.82415	0.197479	4.1734	0.000297
(3)Fuel-air equivalence ratio (phi)(L)	-0.73000	0.299582	-2.4367	0.021974
Fuel-air equivalence ratio (phi)(Q)	0.38874	0.197479	1.9685	0.059760
(4)Intake pressure (bar)(L)	3.88438	0.299582	12.9660	0.000000
Intake pressure (bar)(Q)	1.11499	0.197479	5.6461	0.000006
(5)Valve overlap (ºCA)(L)	-0.28750	0.299582	-0.9597	0.346060
Valve overlap (ºCA)(Q)	-0.09126	0.197479	-0.4621	0.647819
1L by 2L	-1.14750	0.599163	-1.9152	0.066532
1L by 3L	0.58500	0.599163	0.9764	0.337883
1L by 4L	-0.52500	0.599163	-0.8762	0.388933
1L by 5L	0.04250	0.599163	0.0709	0.943994
2L by 3L	1.05250	0.599163	1.7566	0.090756
2L by 4L	-0.31500	0.599163	-0.5257	0.603529
2L by 5L	-0.31750	0.599163	-0.5299	0.600674
3L by 4L	-3.00250	0.599163	-5.0112	0.000033
3L by 5L	-0.01500	0.599163	-0.0250	0.980218
4L by 5L	-0.09000	0.599163	-0.1502	0.881759

Table E.3: Complete regression model of NOx/kWh to SI engine (equation (5-3))

Effect Estimates; Var.:NOx (mg/kWh); R-sqr=,9334; Adj:,88216 (SI Results) 5 3-level factors, 1 Blocks, 47 Runs; MS Residual=2832,68 DV: NOx (mg/kWh)				
Factor	Coeff.	Std.Err.	t(26)	p
Mean/Interc.	141.7360	19.40532	7.3040	0.000000
(1)H2 percentage in fuel (%)(L)	-4.2406	13.30573	-0.3187	0.752495
H2 percentage in fuel (%)(Q)	-17.7787	8.77093	-2.0270	0.053031
(2)Engine speed (rpm)(L)	-15.7988	13.30573	-1.1874	0.245819
Engine speed (rpm)(Q)	1.3342	8.77093	0.1521	0.880267
(3)Fuel-air equivalence ratio (phi)(L)	197.3794	13.30573	14.8342	0.000000
Fuel-air equivalence ratio (phi)(Q)	-90.5195	8.77093	-10.3204	0.000000
(4)Intake pressure (bar)(L)	25.3231	13.30573	1.9032	0.068145
Intake pressure (bar)(Q)	4.3805	8.77093	0.4994	0.621676
(5)Valve overlap (ºCA)(L)	1.7844	13.30573	0.1341	0.894352
Valve overlap (ºCA)(Q)	6.4205	8.77093	0.7320	0.470705
1L by 2L	0.3375	26.61146	0.0127	0.989978
1L by 3L	-9.6575	26.61146	-0.3629	0.719608
1L by 4L	-1.0800	26.61146	-0.0406	0.967938
1L by 5L	-0.1575	26.61146	-0.0059	0.995323
2L by 3L	-52.7300	26.61146	-1.9815	0.058205
2L by 4L	-1.4700	26.61146	-0.0552	0.956370
2L by 5L	0.3275	26.61146	0.0123	0.990275
3L by 4L	78.5375	26.61146	2.9513	0.006622
3L by 5L	4.5175	26.61146	0.1698	0.866515
4L by 5L	0.6250	26.61146	0.0235	0.981442

Table E.4: Complete regression model of NOx/kWh to SACI engine (equation (5-4))

Effect Estimates; Var.:NOx (mg/kWh); R-sqr=,93519; Adj:,88533 (SACI Results) 5 3-level factors, 1 Blocks, 47 Runs; MS Residual=27067,76 DV: NOx (mg/kWh)				
Factor	Coeff.	Std.Err.	t(26)	p
Mean/Interc.	518.554	59.98578	8.64462	0.000000
(1)H2 percentage in fuel (%)(L)	-0.785	41.13071	-0.01909	0.984919
H2 percentage in fuel (%)(Q)	-74.371	27.11271	-2.74303	0.010877
(2)Engine speed (rpm)(L)	-87.825	41.13071	-2.13527	0.042328
Engine speed (rpm)(Q)	-11.490	27.11271	-0.42379	0.675205
(3)Fuel-air equivalence ratio (phi)(L)	603.210	41.13071	14.66569	0.000000
Fuel-air equivalence ratio (phi)(Q)	-263.470	27.11271	-9.71759	0.000000
(4)Intake pressure (bar)(L)	167.819	41.13071	4.08013	0.000379
Intake pressure (bar)(Q)	-16.506	27.11271	-0.60879	0.547947
(5)Valve overlap (ºCA)(L)	5.956	41.13071	0.14481	0.885975
Valve overlap (ºCA)(Q)	17.869	27.11271	0.65907	0.515648
1L by 2L	-9.063	82.26141	-0.11017	0.913123
1L by 3L	3.767	82.26141	0.04580	0.963820
1L by 4L	42.495	82.26141	0.51658	0.609812
1L by 5L	-1.500	82.26141	-0.01823	0.985591
2L by 3L	-192.735	82.26141	-2.34296	0.027057
2L by 4L	-66.465	82.26141	-0.80797	0.426437
2L by 5L	0.473	82.26141	0.00574	0.995461
3L by 4L	403.800	82.26141	4.90874	0.000043
3L by 5L	10.078	82.26141	0.12251	0.903440
4L by 5L	6.105	82.26141	0.07421	0.941408

Table E.5: Complete regression model of CO_2/kWh to SI engine (equation (5-5))

Effect Estimates; Var.:CO2 (g/kWh); R-sqr=,93983; Adj:,89355 (SI Results) 5 3-level factors, 1 Blocks, 47 Runs; MS Residual=35,2137 DV: CO2 (g/kWh)				
Factor	Coeff.	Std.Err.	t(26)	p
Mean/Interc.	129.8867	2.163605	60.0325	0.000000
(1)H2 percentage in fuel (%)(L)	-17.6944	1.483528	-11.9272	0.000000
H2 percentage in fuel (%)(Q)	1.6614	0.977918	1.6989	0.101275
(2)Engine speed (rpm)(L)	3.6963	1.483528	2.4915	0.019426
Engine speed (rpm)(Q)	-2.3557	0.977918	-2.4089	0.023383
(3)Fuel-air equivalence ratio (phi)(L)	0.6481	1.483528	0.4369	0.665805
Fuel-air equivalence ratio (phi)(Q)	-2.4244	0.977918	-2.4792	0.019975
(4)Intake pressure (bar)(L)	-19.0438	1.483528	-12.8368	0.000000
Intake pressure (bar)(Q)	-6.4324	0.977918	-6.5776	0.000001
(5)Valve overlap (ºCA)(L)	-0.1350	1.483528	-0.0910	0.928191
Valve overlap (ºCA)(Q)	0.1443	0.977918	0.1476	0.883829
1L by 2L	1.2125	2.967057	0.4087	0.686140
1L by 3L	-0.2700	2.967057	-0.0910	0.928191
1L by 4L	3.1700	2.967057	1.0684	0.295160
1L by 5L	0.0450	2.967057	0.0152	0.988015
2L by 3L	-3.3625	2.967057	-1.1333	0.267440
2L by 4L	2.7950	2.967057	0.9420	0.354858
2L by 5L	0.6450	2.967057	0.2174	0.829604
3L by 4L	15.6225	2.967057	5.2653	0.000017
3L by 5L	0.7975	2.967057	0.2688	0.790217
4L by 5L	1.0725	2.967057	0.3615	0.720670

Table E.6: Complete regression model of CO_2/kWh to SACI engine (equation (5-6))

Effect Estimates; Var.:CO2 (g/kWh); R-sqr=,95603; Adj:,9222 (SACI Results) 5 3-level factors, 1 Blocks, 47 Runs; MS Residual=22,81067 DV: CO2 (g/kWh)				
Factor	Coeff.	Std.Err.	t(26)	p
Mean/Interc.	117.9526	1.741370	67.7355	0.000000
(1)H2 percentage in fuel (%)(L)	-20.6344	1.194013	-17.2815	0.000000
H2 percentage in fuel (%)(Q)	-1.3670	0.787074	-1.7368	0.094251
(2)Engine speed (rpm)(L)	-1.0169	1.194013	-0.8516	0.402188
Engine speed (rpm)(Q)	-2.8012	0.787074	-3.5590	0.001460
(3)Fuel-air equivalence ratio (phi)(L)	0.4688	1.194013	0.3926	0.697827
Fuel-air equivalence ratio (phi)(Q)	-1.5608	0.787074	-1.9830	0.058024
(4)Intake pressure (bar)(L)	-16.1463	1.194013	-13.5227	0.000000
Intake pressure (bar)(Q)	-5.1208	0.787074	-6.5061	0.000001
(5)Valve overlap (ºCA)(L)	-0.3725	1.194013	-0.3120	0.757549
Valve overlap (ºCA)(Q)	0.0017	0.787074	0.0022	0.998267
1L by 2L	4.2400	2.388026	1.7755	0.087519
1L by 3L	-1.7350	2.388026	-0.7265	0.473998
1L by 4L	2.9575	2.388026	1.2385	0.226607
1L by 5L	0.1050	2.388026	0.0440	0.965265
2L by 3L	-4.1775	2.388026	-1.7494	0.092027
2L by 4L	1.3400	2.388026	0.5611	0.579512
2L by 5L	0.3150	2.388026	0.1319	0.896072
3L by 4L	11.4750	2.388026	4.8052	0.000056
3L by 5L	0.6825	2.388026	0.2858	0.777295
4L by 5L	0.7425	2.388026	0.3109	0.758336

Table E.7: Complete regression model of E_{fuel} to SI engine (equation (5-7))

Effect Estimates; Var.:Efuel (kJ/cycle); R-sqr=,99562; Adj:,99226 (SI Results) 5 3-level factors, 1 Blocks, 47 Runs; MS Residual=,0012 DV: Efuel (kJ/cycle)				
Factor	Coeff.	Std.Err.	t(26)	p
Mean/Interc.	0.879458	0.012630	69.63198	0.000000
(1)H2 percentage in fuel (%)(L)	0.162581	0.008660	18.77353	0.000000
H2 percentage in fuel (%)(Q)	0.015060	0.005709	2.63819	0.013890
(2)Engine speed (rpm)(L)	-0.015131	0.008660	-1.74723	0.092401
Engine speed (rpm)(Q)	0.002985	0.005709	0.52297	0.605426
(3)Fuel-air equivalence ratio (phi)(L)	0.440063	0.008660	50.81477	0.000000
Fuel-air equivalence ratio (phi)(Q)	0.011331	0.005709	1.98494	0.057796
(4)Intake pressure (bar)(L)	0.454538	0.008660	52.48622	0.000000
Intake pressure (bar)(Q)	-0.001794	0.005709	-0.31422	0.755863
(5)Valve overlap (ºCA)(L)	0.002600	0.008660	0.30023	0.766392
Valve overlap (ºCA)(Q)	0.000573	0.005709	0.10036	0.920828
1L by 2L	-0.002400	0.017320	-0.13857	0.890861
1L by 3L	0.068925	0.017320	3.97944	0.000493
1L by 4L	0.082825	0.017320	4.78197	0.000060
1L by 5L	0.000275	0.017320	0.01588	0.987453
2L by 3L	-0.007700	0.017320	-0.44457	0.660312
2L by 4L	-0.009025	0.017320	-0.52107	0.606731
2L by 5L	0.002200	0.017320	0.12702	0.899903
3L by 4L	0.227425	0.017320	13.13058	0.000000
3L by 5L	0.001350	0.017320	0.07794	0.938470
4L by 5L	0.003075	0.017320	0.17754	0.860462

Table E.8: Complete regression model of E_{fuel} to SACI engine (equation (5-8))

Effect Estimates; Var.:Efuel (kJ/cycle); R-sqr=,99569; Adj:,99237 (SACI Results) 5 3-level factors, 1 Blocks, 47 Runs; MS Residual=,0011338 DV: Efuel (kJ/cycle)				
Factor	Coeff.	Std.Err.	t(26)	p
Mean/Interc.	0.858776	0.012277	69.95023	0.000000
(1)H2 percentage in fuel (%)(L)	0.159225	0.008418	18.91483	0.000000
H2 percentage in fuel (%)(Q)	0.014788	0.005549	2.66500	0.013053
(2)Engine speed (rpm)(L)	-0.012463	0.008418	-1.48046	0.150768
Engine speed (rpm)(Q)	0.002763	0.005549	0.49794	0.622709
(3)Fuel-air equivalence ratio (phi)(L)	0.434456	0.008418	51.61041	0.000000
Fuel-air equivalence ratio (phi)(Q)	0.010542	0.005549	1.89985	0.068599
(4)Intake pressure (bar)(L)	0.441694	0.008418	52.47018	0.000000
Intake pressure (bar)(Q)	-0.001083	0.005549	-0.19512	0.846814
(5)Valve overlap (ºCA)(L)	0.001525	0.008418	0.18116	0.857647
Valve overlap (ºCA)(Q)	0.000221	0.005549	0.03990	0.968474
1L by 2L	-0.002275	0.016836	-0.13513	0.893552
1L by 3L	0.068775	0.016836	4.08500	0.000374
1L by 4L	0.080875	0.016836	4.80370	0.000056
1L by 5L	0.000225	0.016836	0.01336	0.989439
2L by 3L	-0.006875	0.016836	-0.40835	0.686359
2L by 4L	-0.006375	0.016836	-0.37865	0.708020
2L by 5L	0.001425	0.016836	0.08464	0.933196
3L by 4L	0.222275	0.016836	13.20237	0.000000
3L by 5L	0.001250	0.016836	0.07425	0.941383
4L by 5L	0.001450	0.016836	0.08613	0.932027